

A NOVEL METHOD TO IMPROVE QUANTITATIVE  
SUSCEPTIBILITY MAPPING WITH AN APPLICATION  
FOR MEASURING CHANGES IN BRAIN OXYGEN  
SATURATION IN THE PRESENCE OF CAFFEINE  
AND DIAMOX



A NOVEL METHOD TO IMPROVE QUANTITATIVE  
SUSCEPTIBILITY MAPPING WITH AN APPLICATION FOR  
MEASURING CHANGES IN BRAIN OXYGEN SATURATION IN THE  
PRESENCE OF CAFFEINE AND DIAMOX

BY

SAGAR BUCH

A Thesis

Submitted to the School of Graduate Studies

in Partial Fulfillment of the Requirements

for the Degree of Ph.D.

(Doctor of Philosophy)

in Biomedical Engineering

McMaster University

© Copyright by Sagar Buch, April 2015

Ph.D. (2015)

McMaster University

(Biomedical Engineering)

Hamilton, ON, Canada

TITLE: A Novel Method to Improve Quantitative Susceptibility Mapping  
with an Application for Measuring Changes in Brain Oxygen Saturation in  
the Presence of Caffeine and Diamox

AUTHOR: Sagar Buch, M.A.Sc.

SUPERVISOR: Dr. E. Mark Haacke

NUMBER OF PAGES: xvi, 116

## Abstract

Magnetic Resonance Imaging (MRI) is a widely used, non-invasive imaging technique that provides a means to reveal structural and functional information of different body tissues in detail. Susceptibility Weighted Imaging (SWI) is a field in MRI that utilizes the information from the magnetic susceptibility property of different tissues using the gradient echo phase information. Although longer echo times (TEs) have been widely used in applications involving SWI, there are a few problems related with the long TE data, such as the strong blooming effect and phase aliasing even at macroscopic levels. In this thesis, the use of very short TEs is proposed to study susceptibility mapping. The short TEs can be used to study structures with susceptibilities an order of magnitude larger (such as air and bones in and around the brain sinuses, skull and teeth) than those within soft tissue. Using the phase replacement technique that we recently developed, it becomes possible to map the geometry of such structures, which to date has proven difficult due to the lack of water content (for sinuses) or due to very short  $T_2^*$  (for bones).

The method of phase replacement inside the sinuses proposed in this thesis provides more accurate phase information for the inversion than assuming zero or some arbitrary constant inside these structures. The first and second iterations were responsible for most of the changes in mapping out the susceptibility values. The mean susceptibility value in the sphenoid sinus is calculated as  $+9.3 \pm 1.1$ ppm, close to the expected value of +9.4ppm for air. The reconstruction of the teeth in the *in-vivo* data provides a mean  $\Delta\chi_{(\text{teeth-tissue})} = 3.3$ ppm, thanks to the preserved phase inside the jaw. This is in agreement with the

susceptibility value measured from a tooth phantom ( $\Delta\chi_{(\text{tooth-phantom})}=-3.1\text{ppm}$ ). The mean susceptibility inside a relatively homogeneous region of the skull bone was measured to be  $\Delta\chi_{(\text{bone-tissue})}=-2.1\text{ppm}$ . Finally, these susceptibilities can be used to help remove the unwanted background fields prior to applying either SHARP or HPF.

In addition, the effects of the background field gradient on flow compensation are studied. Due to the presence of these background gradients, an unwanted phase term is induced by the blood flow inside the vessels. Using a 3D numerical model and *in vivo* data, the background gradients were estimated to be as large as 1.5mT/m close to the air-tissue interfaces and 0.7mT/m inside the brain (leading to a potential signal loss of up to 15%). The quantitative susceptibility mapping (QSM) results were improved in the entire image after removing the confounding arterial phase thanks to the reduced ringing artifacts.

Lastly, a novel approach to improve the susceptibility mapping results was introduced and utilized to monitor the changes in venous oxygen saturation levels as well as the changes in oxygen extraction fraction instigated by the vasodynamic agents, caffeine and acetazolamide. The internal streaking artifacts in the susceptibility maps were reduced by giving an initial susceptibility value uniformly to the structure-of-interest, based on the *a priori* information. For veins, the iterative results, when the initial value of 0.45 ppm was used, were the best in terms of the highest accuracy in the mean susceptibility value (0.453 ppm) and the lowest standard deviation (0.013 ppm). Using this technique, the venous oxygen saturation levels (inside the internal cerebral veins (ICVs)) for normal physiological conditions, post-caffeine and post-Diamox for the first volunteer were

calculated as (mean  $\pm$  standard deviation):  $Y_{\text{Normal}} = 69.1 \pm 3.3 \%$ ,  $Y_{\text{Caffeine}} = 60.5 \pm 2.8 \%$  and  $Y_{\text{Diamox}} = 79.1 \pm 4.0\%$ .

For the caffeine challenge, the percentage change in oxygen extraction fraction (OEF) for pre and post caffeine results was calculated as  $+27.0 \pm 3.8\%$ ; and for the Diamox challenge, the percentage change in OEF was calculated as  $-32.6 \pm 2.1 \%$  for the ICVs. These vascular effects of Diamox and caffeine were large enough to be easily measured with susceptibility mapping and can serve as a sensitive biomarker for measuring reductions in cerebro-vascular reserve through abnormal vascular response, an increase in oxygen consumption during reperfusion hyperoxia or locally varying oxygen saturation levels in regions surrounding damaged tissue.

In conclusion, our new approach to QSM offers a means to monitor venous oxygen saturation reasonably accurately and may provide a new means to study neurovascular diseases where there are changes in perfusion that affect the oxygen extraction fraction.

## Acknowledgements

I would like to sincerely thank my supervisor, Dr. E. Mark Haacke, for encouraging my research and for allowing me to grow as a researcher. He invariably finds time for his students and collaborators to sort out their problems and gives them new, interesting ideas to think about. Dr. Haacke and his works have been and will always be a huge source of inspiration for me. It has been an unbelievable privilege to work under your guidance.

I am very thankful to Dr. Michael Noseworthy, for his continuous support, motivation and enthusiasm during my graduate career. His extremely informative and insightful approach of teaching the students is very instrumental in our progress and attending his courses has always been a delight. I cannot thank my supervisory committee members, Dr. Maureen MacDonald and Dr. Qiyin Fang, enough for their extremely helpful comments and guidance. Your words of encouragement have brought me to where I am right now.

I would also like to acknowledge Dr. Yu-Chung Norman Cheng, Dr. Jaladhar Neelavalli and Dr. Yongquan Ye at Wayne State University, for their help and time they spent in clearing my doubts. I wish to thank my colleague at McMaster University, Saifeng Liu, for sharing his knowledge and experiences that has been instrumental in my research work.

I wish to thank my parents, my mother, Dr. Bharati Buch and my father, Dr. Yatrik Buch, for the immense love and support they gave me throughout my life. I could not have come so far without them. This thesis is dedicated to them.

## Table of Contents

Chapter 1: Introduction .....	1
Chapter 2: Basics Of Mr Phase Signal And Magnetic Susceptibility.....	7
2.1 Larmor Frequency And Free Induction Decay .....	7
2.2 Magnetic Susceptibility.....	9
2.3 Gradient Echo Imaging .....	13
2.4 Magnetic Field Perturbations ( $\Delta B(r)$ ) .....	19
2.5 Background Field Removal.....	24
2.6 Forward Method For Calculating Field Perturbations .....	27
2.7 Susceptibility Mapping .....	30
Chapter 3: Susceptibility Mapping Of Air, Bone And Calcium In The Head.....	39
3.1 Introduction .....	39
3.2 Methods.....	41
3.3 Results .....	49
3.4 Discussion And Conclusions.....	58
Chapter 4: Estimation Of Phase Change Induced By Blood Flow In Presence Of Background Gradients ( $G'$ ) .....	67
4.1 Introduction .....	67
4.2 Theory .....	69

4.3 Methods.....	73
4.4 Results.....	75
4.5 Discussion And Conclusions.....	81
Chapter 5: Measuring The Changes In Cerebral Oxygen Extraction Fraction.....	87
5.1 Introduction.....	87
5.2 Theory.....	89
5.3 Methods.....	90
5.4 Results.....	93
5.5 Discussion And Conclusions.....	101
Chapter 6: Future Directions.....	111

## List of Figures

### Chapter 2:

- Figure 2.1.** The precession of a spin after the application of an RF pulse, a), which generates an observable NMR signal called free induction decay (FID) signal in the absence of any magnetic gradients, b). ..... 9
- Figure 2.2.** Basics of a gradient echo sequence. a) The effects of applying a positive or negative gradient field in presence of the main external magnetic field ( $B_0$ ), b) A simple representation of a gradient-echo pulse sequence. .... 14
- Figure 2.3.** Pulse sequence diagram for a 3D gradient echo MR acquisition with flow compensation in all three directions to reduce the effects of pulsatility effects of the blood or cerebrospinal fluid flow. The pulse sequence includes first order gradient moment nulling in readout ( $G_r$ ) and slice-select ( $G_s$ ) directions. The partition encoding and phase encoding ( $G_p$ ) gradients are velocity compensated with respect to the echo. .... 17
- Figure 2.4.** Complex representation of an MR signal acquired through ‘Real’ and ‘Imaginary’ channels.  $|S|$  represents the magnitude and  $\varphi$  is the phase component of an MR signal. .... 19
- Figure 2.5.** A cylinder with a radius ‘a’ placed at an angle  $\theta$  to the external magnetic field  $B_0$  and is the polar angle in the x-y plane of the point ‘p’ relative to the external field. The magnetic field variation outside the cylinder at a point ‘p’ with a distance  $\rho$  can be defined by Eq. 2.17. .... 23

**Figure 2.6.** a) Original unfiltered phase image with imaging parameters: TE=20ms, B<sub>0</sub>=3T with 0.5×0.5×0.5mm<sup>3</sup> resolution and b) Homodyne high pass filtered phase image with filter size of 64×64 pixels, c) phase images processed with SHARP algorithm (radius=6 pixels and th=0.05). The filtered phase images in b) and c) shows the underlying tissue information much clearly due to the reduced background field variations. .... 26

**Figure 2.7.** a) Original susceptibility map (SM) of a 3D brain model, b) Simulated phase generated by using the forward calculation of the magnetic field perturbations (Eq. 2.31) at TE=20ms and B<sub>0</sub>=3T, c) SM reconstructed from phase information in b) using the inverse process (Eq. 2.32 and Eq. 2.33)..... 32

**Figure 2.8.** Susceptibility maps before and after the iterative method using veins as the structure-of-interest. a) Original susceptibility map in sagittal view, b) Iterative result of a) after three iterations, c) The difference map of a) and b), d) Same original susceptibility map as a) in coronal view, e) Iterative result of a) after three iterations in coronal view, f) The difference map of d) and e). White arrows indicate the streaking artifacts seen in the original susceptibility maps a) and d). The difference maps demonstrate that this streaking noise is almost completely removed after three iterations of iterative method. .... 34

### Chapter 3:

**Figure 3.1.** Illustration of the proposed sinus mapping process using short TE and phase replacement method. Phase replacement steps are repeated until the relative change of the mean susceptibility inside the sinuses is less than some chosen value of  $\beta$ . The mask,  $M_{\text{head}}$ , is used to remove the noisy pixels from phase images, whereas  $M_{\text{air/bone}}$  represents the mask

of structures-of-interest for phase replacement process (in this case: sinuses, bones and teeth). ..... 47

**Figure 3.2.** Simulation of the phase behavior using a 3D numerical model. a) In vivo  $T_1$ -weighted data used to generate the 3D model, b) 3D numerical brain model, and c) simulated phase of the air-tissue interfaces using Eq. 9. .... 49

**Figure 3.3.** a) 3D brain model used to test the proposed concept; b) simulated phase image generated from a) by using a forward calculation ( $TE=2.5ms$  and  $B_0=3T$ ); c) brain mask ( $M_{brain}$ ); d) head mask ( $M_{head}$ ); e) measured susceptibility map resulting from the phase simulation keeping phase only inside the brain, by using the  $M_{brain}$  mask; and f) measured susceptibility map resulting from the phase simulation using phase information from all tissues surrounding the sinuses inside the head, by using the  $M_{head}$  mask. Note the major improvement in the shape and susceptibility of the ethmoid sinus. .... 50

**Figure 3.4.** Susceptibility reconstruction of the tooth phantom. a) Original phase image at  $TE=2.5ms$ , b) processed phase image and c) reconstructed susceptibility map of the tooth phantom generated after five phase replacement iterations. The mean susceptibility value inside the tooth is measured as  $\Delta\chi_{(teeth-tissue)} = -3.1 \pm 1.2$ . .... 50

**Figure 3.5.** Comparison of the magnitude images (a, b and c) and susceptibility maps (d, e and f) in all three views, showing agreement spatially between the sinuses and teeth in the original magnitude images and their reconstruction in the susceptibility maps. Structures are identified by the white arrows: 1 – Frontal sinus, 2 – maxillary sinus, 3 – teeth, 4 – mastoid sinus, 5 – ear canal, 6 – ethmoid sinus, 7 – occipital skull bone. .... 52

**Figure 3.6.** Measured mean susceptibility values and standard deviations inside the sphenoid sinus from the brain model (a and b); along with sphenoid sinus (c and d), teeth (e and f) and bone (g and h) from the in vivo data. .... 53

**Figure 3.7.** Background field removal using extracted susceptibility distributions inside the sinuses, bones and teeth for two different volunteers: (a-d) volunteer 1 and (e-h) volunteer 2. a) and e) original phase data acquired at  $TE = 7.5\text{ms}$ , b) and f) predicted magnetic perturbations  $TE=7.5\text{ms}$  and  $B_0=3\text{T}$ , c) and g) resultant phase information produced after subtracting the predicted phase from original phase images. The phase profile plots (d and h), along the black lines, demonstrate that the predicted phase agrees well with the original phase behavior outside the sinuses. .... 55

**Figure 3.8.** Improvement in phase processing using susceptibility maps of sinuses and bones. The phase images shown in this figure are acquired at  $TE=7.5\text{ms}$  and field strength of  $3\text{T}$ . a) Conventional homodyne high pass (HP) filtering with  $32 \times 32$  filter size, b) homodyne HP filtered image ( $32 \times 32$  filter size) applied after subtracting the forward modeled phase generated from susceptibility maps of sinuses and bones, c) filtered phase image generated using SHARP method. d), e) and f) are the resultant susceptibility maps generated from phase images shown in a), b) and c), respectively. The white arrows demonstrate the areas of improvement using the forward modeled phase, namely the preservation of SSS (long arrow) and significant reduction of phase behavior caused by the air-tissue interfaces (short arrow). The effect of the improper boundary conditions due to the erosion of the brain near the SSS in the SHARP processed phase images is indicated by the black arrows. .... 57

## Chapter 4:

**Figure 4.1.** A negative background gradient ( $G_x'$ ) in the readout direction and the induced echo shift. The center of the sampling period represents the ideal echo time, TE. However, in presence of an extraneous gradient ( $G_x'$ ), the shifted echo occurs at the time TE'..... 71

**Figure 4.2.** Calculated background gradient deviations along three dimensions: (a, d and g) along x-direction,  $G_x'$ ; (b, e and h) along y-direction,  $G_y'$ ; and (c, f and i) along z-direction,  $G_z'$ ; shown in transverse, sagittal and coronal planes. The profiles in j), k) and l) were measured along the black lines shown in a), b) and c), respectively. .... 76

**Figure 4.3.** Phase accumulation due to flow in presence of the background gradient ( $G'$ ) in: a) x-direction (left-right), b) y-direction (up-down) and c) in z-direction (perpendicular to the plane of the image); for blood flow velocity of 60cm/s and TE = 20ms. .... 77

**Figure 4.4.** a) Original, low resolution, unwrapped phase image (TE = 2.5ms), b) sinus maps generated from a, c) the predicted field ( $\Delta B$ ) generated from the sinus shown in b, d) frequency profiles generated along the black line in a and c. Note the agreement between the original phase and predicted field. .... 77

**Figure 4.5.** a) Original, high resolution, magnitude image with b) homodyne high-pass filtered  $32 \times 32$  (TE=17.5ms), c) simulated maps representing background gradient induced phase (in x-direction, i.e.  $G_x'$ ), assuming the blood flow velocity of MCAs is  $v = 60\text{cm/s}$  and TE = 17.5ms; and d) resultant phase image after correcting the flow-induced phase inside left and right MCAs (identified by the black and white arrows, respectively, representing opposite flow directions). .... 79

**Figure 4.6.** Background gradients generated from field inhomogeneities caused by the veins. Susceptibility maps are shown in a) transverse and b) sagittal views. Red crosses are used to identify the vein of Galen. The background gradients were measured primarily in c) y-direction and d) z-direction. .... 79

**Figure 4.7.** Phase images and susceptibility maps with and without the suppression of phase from the arteries. a) SHARP processed result using the original phase images, b) susceptibility map produced from a), c) SHARP processed result using the phase images generated after setting the phase inside the arteries to zero, d) susceptibility map produced from c)..... 80

## Chapter 5:

**Figure 5.1.** Simulated susceptibility maps produced from a 3D numerical model using a) conventional iterative algorithm, b) the proposed method by assigning 450ppb to veins and c) by assigning 700ppb to veins. Images d, e and f are contrast modified versions of a, b, and c to visualize the extent of internal streaking artifacts. .... 94

**Figure 5.2.** Mean (a) and standard deviation (b) of the susceptibility measured inside the superior sagittal sinus at each iteration of the iterative SWIM algorithm. Different initial values ( $\chi_0$ ) were set to the veins. Independent of the choice of starting point, the values tend to converge close to the expected susceptibility of 0.45 ppm. The use of proper initial value reduces the streaking artifacts inside the veins. .... 94

**Figure 5.3.** a) Susceptibility maps generated using the conventional iterative technique, and b) susceptibility maps generated using the forced value iterative method. Note the

improvement in the susceptibility distribution, inside the veins of different sizes, in d) with respect to the conventional iterative SWIM results in c). ..... 96

**Figure 5.4.** Evaluation of dynamic changes in venous susceptibility distribution due to the administration of caffeine and Diamox. Phase data is acquired for four time points after the drug ingestion, at an interval of 15 minutes. a) and f) Susceptibility maps for the data acquired before caffeine and Diamox intake, respectively, b-e) susceptibility maps for the data at four times points after caffeine intake, g-j) susceptibility maps the data at four times points after Diamox intake. .... 97

**Figure 5.5.** Susceptibility maps generated from the data acquired: a) post-Diamox administration, b and c) pre-Diamox and pre-caffeine administration, d) post-caffeine administration for healthy volunteers. The profile plot demonstrates the variation in susceptibility values across the internal cerebral veins caused by these altered brain states. .... 98

**Figure 5.6.** Susceptibility values measured inside the major cerebral veins across five healthy volunteers. The phase data was acquired before and after the administration of Diamox and Caffeine with TE = 15ms and voxel resolution =  $(0.5\text{mm})^3$ . Each drug test was performed on separate days. The susceptibility values generated from the data acquired pre-administration of these drugs were averaged. R-ICV, L-ICV: right and left internal cerebral veins; R-TSV, L-TSV: right and left thalamo-striate veins; R-SV, L-SV: right and left septal veins; VoG: Vein of Galen; StrS: Straight sinus. .... 99

## List of Tables

### Chapter 3:

**Table 3.1.** Mean susceptibility value ( $\Delta\chi_{(\text{sinus-tissue})}$ ), standard deviation and relative change, inside the sphenoid sinus of a healthy volunteer, as a function of the number of phase replacement iterations. .... 52

**Table 3.2.** Measured susceptibility distributions (mean  $\pm$  standard deviation) inside the various sinuses ( $\Delta\chi_{(\text{sinus-tissue})}$ ), skull bone ( $\Delta\chi_{(\text{bone-tissue})}$ ) and teeth ( $\Delta\chi_{(\text{teeth-tissue})}$ ) from the 3D brain model and from the four healthy volunteers. These results were produced with five iterations of phase replacement method..... 54

### Chapter 5:

**Table 5.1.** Mean  $\pm$  standard deviation of the percentage change in oxygen extraction fraction for cerebral veins of different vessel sizes, across five healthy subjects, measured before and after administration of Diamox and caffeine. R-ICV, L-ICV: right and left internal cerebral veins; R-TSV, L-TSV: right and left thalamo-striate veins; R-SV, L-SV: right and left septal veins; VoG: Vein of Galen; StrS: Straight sinus. .... 100

# Chapter 1: Introduction

Magnetic Resonance Imaging (MRI) is a widely used, non-invasive imaging technique that provides a means to reveal structural and functional information of different body tissues in detail. The MR magnitude information has been primarily used in MRI for clinical diagnosis due to the soft tissue contrast provided by the images. Depending on the application, a variety of contrasts can be generated between different tissues of interest in the magnitude images by altering the imaging parameters (1). For example, different contrasts are created by spin density,  $T_1$  and  $T_2$  weighted sequences.

Apart from a few applications such as flow quantification, phase sensitive inversion recovery or MRI thermometry, the phase signal had been ignored in obtaining structural information from different tissues (2–5). Susceptibility Weighted Imaging (SWI) is a field in MRI that utilizes the gradient echo phase information to create filtered phase images that are used to enhance contrast in the magnitude images (2,6). The phase signal is dependent on the magnetic susceptibility distribution of a given tissue sample, hence, the phase images offer a unique image contrast. The applications of the phase images include

studying the progress of neurodegenerative diseases like multiple sclerosis by detection of iron deposition in the brain, and the presence of calcium deposition in breast tissue and quantifying oxygen saturation in veins using the susceptibility maps (7–9). Susceptibility mapping technique utilizes the phase information around an object to reconstruct the susceptibility properties across a given tissue (6,10–13).

The strength of phase behavior is dependent on the time of echo, where higher echo times will produce a stronger, more discernible signal. Currently, the focus of phase imaging and susceptibility mapping has been on using longer TEs on the order of  $T_2^*$  (~20 to 30ms) to enhance susceptibility effects for small structures or objects with low susceptibility (14). However, the macroscopic and microscopic phase wrapping or phase aliasing at higher echo times leads to  $T_2^*$  signal loss and blooming artifacts that makes the object appear larger than its actual size. This, in turn, leads to an underestimation of the measured susceptibility. Therefore, in this thesis, use of relatively shorter TEs (~2.5ms) is proposed, especially when studying structures with much stronger susceptibilities in the brain.

The potential applications of utilizing short TEs includes imaging of high iron content in stroke and traumatic brain injury as well as mineralization in Parkinson's disease; imaging of major veins in the body to measure oxygen saturation (2). Furthermore, by preserving the signal outside the brain itself, phase images at short echo times provide a new approach for imaging high susceptibility objects such as sinuses, bones and teeth that have no or unreliable MR signal. Regions which have no signal cannot benefit from any of the usual tissue properties except for susceptibility which usually affects tissues outside the

source. This thesis introduces the phase replacement method, which updates the predicted phase inside an object iteratively in order to improve the susceptibility reconstruction (15). The resulting images for air and bones are not only of interest in and of themselves, but also can be used to model and remove the unwanted background phase to better evaluate local tissue anomalies at long TEs.

Recently, a variety of multi-echo gradient echo sequences have been used for simultaneous MR angiography and venography, susceptibility weighted imaging (SWI) and susceptibility mapping (10,16,17). However, these flow compensated sequences are still highly sensitive to flow artifacts, especially at the longer echo times. The presence of flow induced phase will hamper the quality of SWI images and create artifacts in quantitative susceptibility mapping (QSM). Therefore, it is critical to understand these potential sources of error and then eventually remove them if viable. For the second major part of this thesis, the unwanted phase induced by blood flow in presence of the background gradients is studied and evaluated. This unique approach also suggests that the magnitude images from the first echo can be used as a means to remove spurious phase for QSM calculations.

A recently developed iterative algorithm helps in reducing the streaking artifacts caused by the ill-posed nature (singularity region within the inverse Green's function) of the susceptibility mapping process (18). However, the streaking artifacts inside a structure are carried forward to the final results. For structures with high susceptibility, these artifacts can be stronger and deleterious. The final part of this thesis introduces a method to further improve the susceptibility mapping by reducing the streaking artifacts both inside and

outside a structure-of-interest. This method is then used for measuring the cerebral venous oxygen saturation levels. In this work, the ability of this approach is to demonstrate the quantification of the blood oxygenation level of cerebral veins ( $Y_v$ ) *in vivo*, not only under normal physiological conditions but also by challenging the physiologic conditions, induced by vasodynamic agents such as caffeine or acetazolamide, which affect the cerebral venous blood oxygenation level (19–22). For each of the above mentioned approaches, a 3D numerical brain model was used to predict and validate the associated errors.

## References

1. Haacke EM. Magnetic resonance imaging: physical principles and sequence design. New York, NY [u.a.: Wiley-Liss; 1999.
2. Haacke EM, Mittal S, Wu Z, Neelavalli J, Cheng Y-CN. Susceptibility-Weighted Imaging: Technical Aspects and Clinical Applications, Part 1. Am J Neuroradiol. 2009 Jan 1;30(1):19–30.
3. De Poorter J. Noninvasive MRI thermometry with the proton resonance frequency method: study of susceptibility effects. Magn Reson Med Off J Soc Magn Reson Med Soc Magn Reson Med. 1995 Sep;34(3):359–67.
4. Evans AJ, Iwai F, Grist TA, Sostman HD, Hedlund LW, Spritzer CE, et al. Magnetic resonance imaging of blood flow with a phase subtraction technique. In vitro and in vivo validation. Invest Radiol. 1993 Feb;28(2):109–15.
5. Hou P, Hasan KM, Sitton CW, Wolinsky JS, Narayana PA. Phase-sensitive T1 inversion recovery imaging: a time-efficient interleaved technique for improved tissue contrast in neuroimaging. AJNR Am J Neuroradiol. 2005 Jul;26(6):1432–8.
6. Haacke EM, Reichenbach JR. Susceptibility Weighted Imaging in MRI: Basic Concepts and Clinical Applications. John Wiley & Sons; 2014. 916 p.

7. Haacke EM, Garbern J, Miao Y, Habib C, Liu M. Iron stores and cerebral veins in MS studied by susceptibility weighted imaging. *Int Angiol J Int Union Angiol*. 2010 Apr;29(2):149–57.
8. Fatemi-Ardekani A, Boylan C, Noseworthy MD. Identification of breast calcification using magnetic resonance imaging. *Med Phys*. 2009 Dec;36(12):5429–36.
9. Haacke EM, Tang J, Neelavalli J, Cheng YCN. Susceptibility mapping as a means to visualize veins and quantify oxygen saturation. *J Magn Reson Imaging JMRI*. 2010 Sep;32(3):663–76.
10. Haacke EM, Liu S, Buch S, Zheng W, Wu D, Ye Y. Quantitative susceptibility mapping: current status and future directions. *Magn Reson Imaging*. 2015 Jan;33(1):1–25.
11. Marques J p., Bowtell R. Application of a Fourier-based method for rapid calculation of field inhomogeneity due to spatial variation of magnetic susceptibility. *Concepts Magn Reson Part B Magn Reson Eng*. 2005 Apr 1;25B(1):65–78.
12. Salomir R, de Senneville BD, Moonen CT. A fast calculation method for magnetic field inhomogeneity due to an arbitrary distribution of bulk susceptibility. *Concepts Magn Reson Part B Magn Reson Eng*. 2003 Jan 1;19B(1):26–34.
13. Haacke EM, Lai S, Reichenbach JR, Kuppusamy K, Hoogenraad FG, Takeichi H, et al. In vivo measurement of blood oxygen saturation using magnetic resonance imaging: a direct validation of the blood oxygen level-dependent concept in functional brain imaging. *Hum Brain Mapp*. 1997;5(5):341–6.
14. Haacke EM, Xu Y, Cheng Y-CN, Reichenbach JR. Susceptibility weighted imaging (SWI). *Magn Reson Med*. 2004;52(3):612–8.
15. Buch S, Liu S, Ye Y, Cheng Y-CN, Neelavalli J, Haacke EM. Susceptibility mapping of air, bone, and calcium in the head. *Magn Reson Med Off J Soc Magn Reson Med Soc Magn Reson Med*. 2014 Jul 7;
16. Ye Y, Hu J, Wu D, Haacke EM. Noncontrast-enhanced magnetic resonance angiography and venography imaging with enhanced angiography. *J Magn Reson Imaging JMRI*. 2013 Dec;38(6):1539–48.
17. Feng W, Neelavalli J, Haacke EM. Catalytic multiecho phase unwrapping scheme (CAMPUS) in multiecho gradient echo imaging: removing phase wraps on a voxel-by-voxel basis. *Magn Reson Med Off J Soc Magn Reson Med Soc Magn Reson Med*. 2013 Jul;70(1):117–26.

18. Tang J, Liu S, Neelavalli J, Cheng YCN, Buch S, Haacke EM. Improving susceptibility mapping using a threshold-based K-space/image domain iterative reconstruction approach. *Magn Reson Med Off J Soc Magn Reson Med Soc Magn Reson Med*. 2013 May;69(5):1396–407.
19. Cameron OG, Modell JG, Hariharan M. Caffeine and human cerebral blood flow: a positron emission tomography study. *Life Sci*. 1990;47(13):1141–6.
20. Chen Y, Parrish TB. Caffeine's effects on cerebrovascular reactivity and coupling between cerebral blood flow and oxygen metabolism. *NeuroImage*. 2009 Feb 1;44(3):647–52.
21. Okazawa H, Yamauchi H, Sugimoto K, Toyoda H, Kishibe Y, Takahashi M. Effects of acetazolamide on cerebral blood flow, blood volume, and oxygen metabolism: a positron emission tomography study with healthy volunteers. *J Cereb Blood Flow Metab Off J Int Soc Cereb Blood Flow Metab*. 2001 Dec;21(12):1472–9.
22. Grossmann WM, Koeberle B. The dose-response relationship of acetazolamide on the cerebral blood flow in normal subjects. *Cerebrovasc Dis Basel Switz*. 2000 Feb;10(1):65–9.

# Chapter 2: Basics of MR Phase Signal and Magnetic Susceptibility<sup>1</sup>

The phase component of the magnetic resonance imaging (MRI) signal has been increasingly employed to improve image contrast, to depict normal or abnormal tissues and to image veins based on the tissue magnetic susceptibility property. In this chapter, the major purpose will be to describe introductory physics of MR phase signal. Furthermore, the post-processing techniques for the phase data as well as the method for susceptibility mapping are described.

## 2.1 Larmor Frequency and Free Induction Decay

MRI is a technique based on the interaction of the external main magnetic field with the nuclear spin. One component of this interaction is the precession of the spins about the magnetic field (1). Nuclear spin is a quantum mechanical intrinsic property of a particle which represents the intrinsic angular momentum of that particle (1).

<sup>1</sup>Most of the contents of this chapter have been adapted from: Haacke et al, “*Magnetic Resonance Imaging: Physical Principles and Sequence Design*,” 1st Ed., Wiley-Liss;1999.

The frequency of the spin precession around the external magnetic field for a right handed system is given by:

$$\omega_0 = \gamma \cdot B_0 \quad [2.1]$$

where,  $\omega_0$  is the frequency of spin precession or the Larmor frequency,  $\gamma$  is the constant known as the gyromagnetic ratio (for a hydrogen proton  $\gamma = 2.68 \times 10^8$  rad/s/Tesla) and  $B_0$  is the external field strength. In the presence of an external magnetic field, the net magnetization of the spins in a tissue is in the direction of the main field. After a time much larger than the  $T_1$  (spin-lattice) relaxation time, this magnetization is known as the equilibrium magnetization ( $M_0$ ) (1). Even though, the external magnetic field tends to align the protons along the direction of the main field, only a fraction of the total number of spins orient themselves in the direction parallel to the main field.

The three major components of an MRI machine include the main magnet that generates a static external magnetic field, the radio frequency (RF) coils that excite a tissue sample using an RF pulse and receive MRI signal and the gradient coils that help in spatial selection of the region of interest(2). Application of a Radio-Frequency (RF) pulse enables the spin of hydrogen protons to orient away from the main field direction. Due to short temporary presence of this RF pulse, the spin will then collectively precess towards the main field direction (2). The process of redirecting themselves parallel to the external field is shown in **Figure 2.1**. The decay of the transverse magnetization (magnetization in x-y plane) is called the Free Induction Decay. This helps in regaining the equilibrium state of the magnetization in the presence of the external field,  $B_0$ .

Time-varying magnetic field derived from the sum of all precessing protons spin fields would induce an emf (electro-motive force) which is detected through the corresponding flux changes by a receiver coil, as seen in the **Figure 2.1** (1).

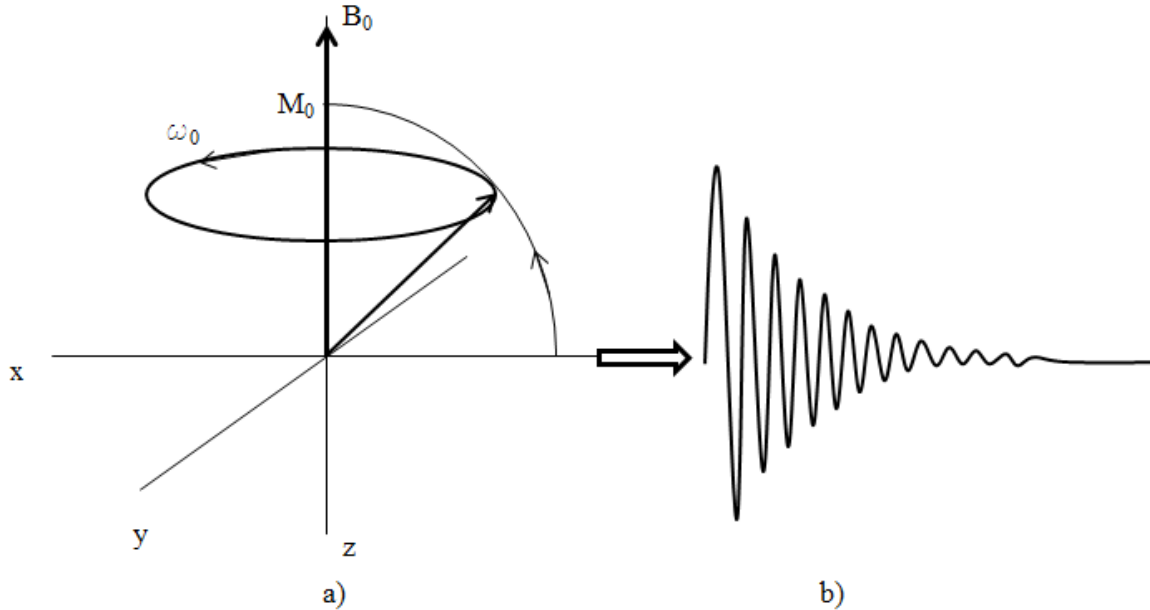


**Figure 2.1.** The precession of a spin after the application of an RF pulse, a), which generates an observable NMR signal called free induction decay (FID) signal in the absence of any magnetic gradients, b).

## 2.2 Magnetic Susceptibility

Several sources of magnetic field variation can be found in the body which can cause signal distortion, loss of signal, image artifacts and  $T_2^*$  losses. Extracorporeal objects include surgically implanted objects, iron-based tattoos, and certain cosmetic products like eye shadows; and also the internal magnetic susceptibility differences found between the tissues in the body (1). While the extracorporeal objects create distortion artifacts, the

internal susceptibility differences can be used to provide a unique contrast in the phase images (3). This attribute may provide special information about tissues, such as distinguishing lesions from normal tissue (3).

Magnetic susceptibility can be defined as the property of a substance, when placed within an external uniform magnetic field, which measures its tendency to get magnetized and alter the magnetic field around it (1).

The physical magnetic field (measured in Tesla) is given by:

$$\vec{B} = \mu \vec{H} \quad [2.2]$$

where,  $\mu$  is the permeability constant of the substance and  $\vec{H}$  is measured in Ampere/meter (A/m) which is approximately the same as  $\vec{B}$  field when there is no substance present (1). A relative permeability of a substance can be defined as  $\mu_r = \mu / \mu_0$ , where for free space  $\mu = \mu_0 = 4\pi \times 10^{-7} \text{Tm/A}$ , a universal constant. The induced magnetic field  $\vec{B}$  inside a substance is given by

$$\vec{B} = \mu_0 (\vec{H} + \vec{M}) \quad [2.3]$$

where  $\vec{M}$  is induced magnetization serving as a macroscopic source of internal field contribution of the electron spin inside the substance (1).

Magnetic susceptibility is viewed as the proportionality constant ( $\chi$ ) for the relation between the induced magnetization in a temporarily magnetized substance and an external magnetic field; and the value of this dimensionless constant describes the magnetic property of the substance (3).

$$\vec{M} = \chi \cdot \vec{H} \quad [2.4]$$

This provides the expression for an induced magnetic field in presence of the external magnetic field and the induced magnetization for a given object with susceptibility  $\chi$  (1). Eq. 2.3 can be written as:

$$\vec{B} = \mu_0 (1 + \chi) \vec{H}$$

$$\text{and, } \vec{B} = \mu_0 \left( \frac{1+\chi}{\chi} \right) \vec{M}$$

$$\text{Hence, } \vec{M} = \left[ \frac{\chi \cdot \vec{B}}{\mu_0(1+\chi)} \right] \approx (\chi \cdot \vec{B}) / \mu_0 \quad (\text{when } \chi \ll 1) \quad [2.5]$$

## 2.2.1 Types of Magnetic Susceptibility

Substances can be classified into diamagnetic, paramagnetic and ferromagnetic materials based on their macroscopic influence over the external magnetic field (1). The magnetization depends on the magnetic susceptibility of the object. For empty space, the value of  $\chi$  is zero, whereas a negative value of  $\chi$  represents a diamagnetic material, if the value of  $\chi$  is positive the material is paramagnetic (1). The terms ‘paramagnetic’ and ‘diamagnetic’ are used relative to the susceptibility of the water rather than vacuum, in MRI field. For ferromagnetic materials, the value of  $\chi$  is much larger than 1 (1). Eq. 2.3 is more suitable expression for the ferromagnetic materials, and, generally, the relevant information for human tissue imaging comes from susceptibility values which are relatively very small (1,3,4).

*Diamagnetic substances:*

Human tissues contain a significant amount of water, making most of the soft tissues diamagnetic in nature. Inert gases, crystal salts, such as NaCl, most organic molecules, and water are some examples of diamagnetic substances. Bone is slightly more diamagnetic than most of the soft tissues in the body (1).

*Paramagnetic substances:*

Iron is strongly paramagnetic so that even small amounts can be detected (1). Gadolinium is another good example of a paramagnetic substance and it is combined with a chelating agent to reduce its toxicity, so it can be used in MRI as a contrast agent to depict the vascular network in different regions. Copper, manganese, and dysprosium, are some other examples of paramagnetic ions that are used for MRI applications. Molecular oxygen is also slightly paramagnetic in nature (4).

*Ferromagnetic substances:*

Ferromagnetic materials, like a horseshoe magnet, can achieve constant magnetization even at a room temperature (4). Ferromagnetism arises from the individual atomic magnetic moments but results in much stronger induced magnetization, than paramagnetic materials, because of their special structural arrangement. The spins are arranged parallel to each other preferentially, making it a lower energy state. The presence of ferromagnetic materials in human tissues is rare compared to diamagnetic or paramagnetic substances. Most of the ferromagnetic signals in MRI originate from an external source rather than a biological tissue (4).

## 2.3 Gradient Echo Imaging

Although, MRI signal is acquired using the receiver coils, the signal is generated using a special set of steps that modify and direct the orientations of spin precession. The free induction decay generates an emf signal (1).

A series of RF pulses are applied to the region of interest which tip the equilibrium magnetization ( $M_0$ ) away from the external magnetic field and generate a signal, other than the free induction decay, in form of an echo which can be easily acquired by the receiver coils(1). A pulse sequence is the pattern of applying these RF pulses to generate the desired echo signal, and this pattern varies with the particular type of image to be produced. In MRI, additional external gradients coils are applied to the tissue sample in order to produce spatially dependent signal from a given tissue sample (2).

*Gradient coils* are used to induce linear variations in the main magnetic field ( $B_0$ ) (*Figure 2.2a*). There are three imaging gradient coils, one for each direction. The variation in the magnetic field permits localization of image slices as well as phase encoding and frequency encoding (2).

*Gradient echo (GRE) imaging* is one of the most important sequence types used in MRI today. GRE sequence has been used to rapidly acquire MRI data with high spatial resolution and low RF power deposition (5,6).

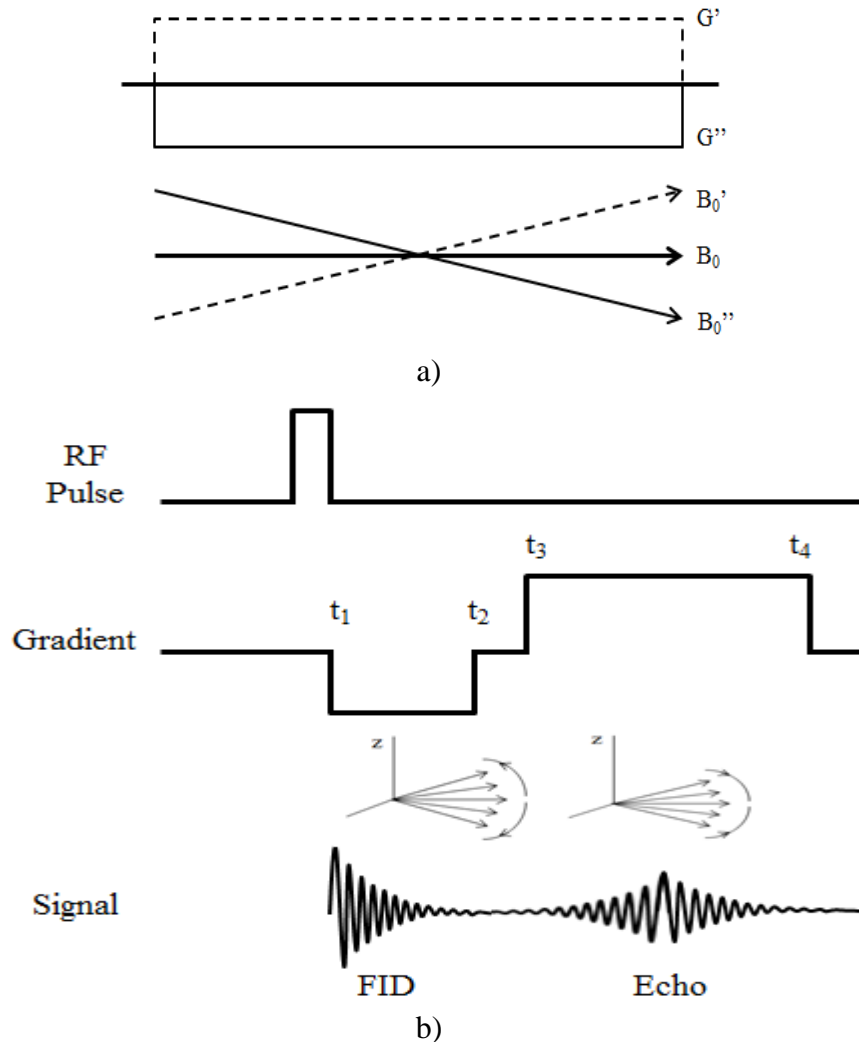


**Figure 2.2.** Basics of a gradient echo sequence. a) The effects of applying a positive or negative gradient field in presence of the main external magnetic field ( $B_0$ ), b) A simple representation of a gradient-echo pulse sequence.

A simple gradient echo sequence diagram can be seen in **Figure 2.2b**). The RF excitation pulse is followed by a negative gradient signal applied from time  $t_1$  to  $t_2$  along the direction of the main magnetic field ( $B_0$ ). The net magnetization vector that is tipped onto the transverse plane shows a linear change in precession frequencies (Larmor frequencies) at different  $z$ -locations (1). This can be understood by referring to Eq. 2.1 that

shows the relationship between the precession frequency and the main magnetic field acting on the spin. The presence of a gradient field causes a linear change in the magnetic field with respect to the position in z-direction (2). The transverse components of spins at different z-locations are shown projected onto the x-y plane below the negative gradient in **Figure 2.2b)** illustrating the dephasing of the signal (2).

Another gradient with reverse polarity is applied to the imaging sample from time  $t_3$  to  $t_4$ . The gradient being opposite in polarity induces rephasing of the signal causing an echo as shown below the positive gradient in **Figure 2.2b)**. The time between the RF pulse excitation and maximum gradient echo signal is called the Echo time (TE). This way the gradient echo permits the recovery of the signal using the gradients.

### 2.3.1 SWI Pulse Sequence

Gradient echo-based MRI is considered a conventional technique and is routinely used for nearly every medical application in both 2D and 3D data acquisition modes (4). For Susceptibility Weighted Imaging (SWI) data acquisition, a 3D, RF spoiled, velocity compensated, gradient echo sequence is used (Please refer to *Figure 2.3*) (4). The signal of this gradient echo sequence also depends on tissue properties like  $T_1$ ,  $T_2^*$  relaxation times, and the spin density (3).

*Gradient moment nulling* (GMN) is a method used to modify a gradient waveform in order to suppress the motion sensitivity of a pulse sequence (2). Gradient moments are values calculated from the integral of a given gradient waveform with time (2):

$$m_n = \int [t^n \cdot \vec{G}(t)] dt \quad [2.6]$$

where,  $m_n$  is the  $n$ th gradient moment of the gradient waveform  $G(t)$ . Gradient moments of a gradient waveform can be nulled, depending on the application, to various degrees and orders. Signal variations that lead to artifacts in the image are caused by the rapid and pulsatile flow of blood and cerebrospinal fluid. These artifacts include signal loss due to flow-induced dephasing, misregistration artifacts and the velocity induced phase (1,2,4). The phase for a spin moving with a constant velocity ( $v$ ) for a bipolar pulse  $G_x$  of duration  $2\tau$  is given by:

$$\varphi = \gamma \vec{G}_x \cdot \vec{v} \tau^2 \quad [2.7]$$

Motion or flow with constant velocity is compensated with first order GMN, by nulling the first moment of a gradient waveform, and is also called velocity compensation or flow compensation (1). For a velocity compensated pulse sequence, the velocity induced phase (given by Eq. 2.7) disappears, which leaves the desired susceptibility induced phase information (4).

**Figure 2.3** represents the original pulse sequence used for SWI data acquisition. A volume with several centimeters of slab thickness is excited using an RF pulse of low flip angle, which is then spatially resolved in 3D space by applying the frequency encoding, phase encoding and partition encoding gradients (1). Velocity compensation is applied in all three spatial directions- slice-select ( $G_s$ ), phase-encoding ( $G_p$ ) and readout ( $G_r$ ) directions to eliminate oblique flow artifacts (1). The partition gradients in slice-select and phase encoding directions are rewound after sampling the echo signal, whereas the readout gradient remains to dephase the spins (1).

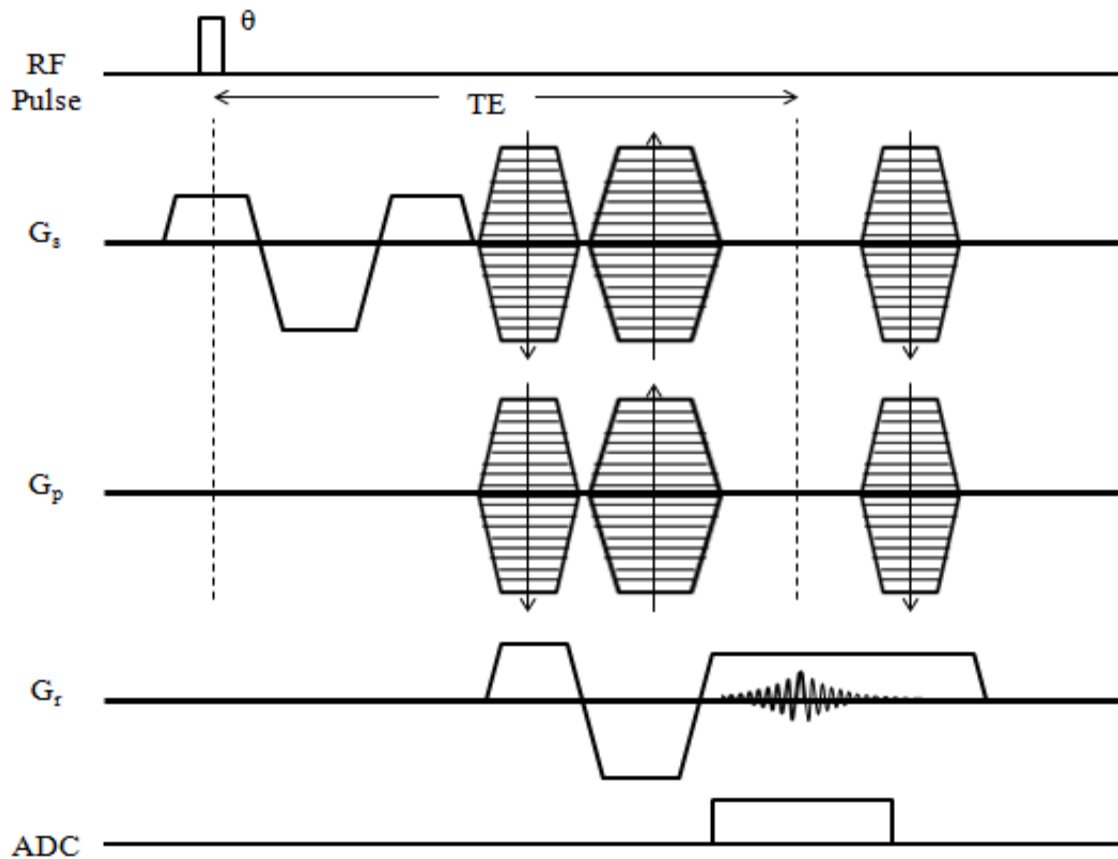


**Figure 2.3.** Pulse sequence diagram for a 3D gradient echo MR acquisition with flow compensation in all three directions to reduce the effects of pulsatility effects of the blood or cerebrospinal fluid flow. The pulse sequence includes first order gradient moment nulling in readout ( $G_r$ ) and slice-select ( $G_s$ ) directions. The partition encoding and phase encoding ( $G_p$ ) gradients are velocity compensated with respect to the echo.

### 2.3.2 Complex MR Signal

The two-dimensional precession of the spin in the transverse plane is represented by complex notation (1). Generally, the signal produced by the rotational motion of the spin

precession in presence of a constant magnetic field is acquired by two channels representing real and imaginary parts of a complex signal:

$$S_{xy}(t) = S_x(t) + i S_y(t) \quad [2.8]$$

where,  $S_x$  and  $S_y$  represent the real and imaginary channels of the signal (Please refer to **Figure 2.4**). This equation can be rewritten as:

$$S_{xy}(t) = |S_{xy}(0)| \cdot e^{i\varphi(\vec{r},t)} \quad [2.9]$$

where,  $|S_{xy}| = \sqrt{S_x^2 + S_y^2}$  is the magnitude and  $\varphi = \tan^{-1}\left(\frac{S_y}{S_x}\right)$  is the phase component of an MR signal. The phase component of the MR signal is dependent on the position of the spin and the phase accumulation with time (1). For a right handed system:

$$\varphi(\vec{r}, t) = -\omega_0 \cdot t + \gamma(B(\vec{r}))t$$

$$\text{or, } \varphi(\vec{r}, t) = -\gamma(B_0 - B(\vec{r}))t \quad [2.10]$$

As seen in the Eq. 2.10, the phase accumulated at time (t) depends on the larmor frequency ( $\omega_0$ ) and the variations in the main magnetic field due to local variation ( $B(\vec{r})$ ) (4). The variations in the main magnetic field are introduced by the external linear fields or structural susceptibility effects which are explained later.

### 2.3.3 Phase Aliasing

In MR imaging, phase is used to encode spatial information at a position ( $\vec{r}$ ). However, in addition to the position-dependent phase created by the spatial encoding gradients, there are unavoidably other forms of remnant or background phase present (1,3). These unwanted

spurious phase effects also need to be understood and dealt with before useful information from MR phase images can be extracted. A general change of phase over time is studied by simplifying the Eq. 2.10:  $\varphi(t) = \Delta\omega \cdot t$ , where,  $\Delta\omega$  represents the effective frequency that includes the original larmor frequency and magnetic field variation components.

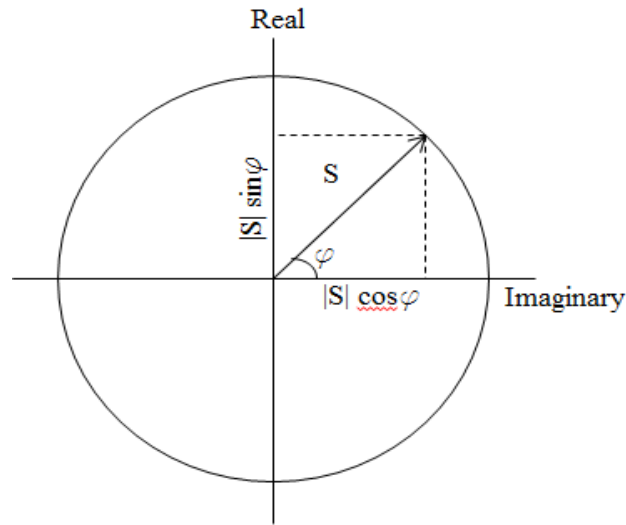


**Figure 2.4.** Complex representation of an MR signal acquired through ‘Real’ and ‘Imaginary’ channels.  $|S|$  represents the magnitude and  $\varphi$  is the phase component of an MR signal.

**Figure 2.4** shows the phase evolution in a complex domain. It is evident that the phase values lie within the range of  $-\pi$  to  $+\pi$ . Therefore, any phase values outside this interval are wrapped back within the interval of  $(-\pi, +\pi)$ . This phase wrapping is also called phase aliasing and the aliasing of phase continues as ‘ $t$ ’ increases (See **Figure 2.6a**) (1).

## 2.4 Magnetic Field Perturbations ( $\Delta B(\vec{r})$ )

The main magnetic field ( $B_0$ ) should ideally be homogeneous at all the parts of the sample. But, practically, there are local magnetic field variations found in the sample,

which can be caused by the imperfect gradient functioning, eddy currents, motion or susceptibility changes between the tissues (1,3,4).

As mentioned before, the phase information can be written as a function of the difference between the uniform field  $B_0$  and the local field  $B(\vec{r})$  variation at position  $\vec{r}$  and time  $t$ . We can rewrite Eq. 2.10 as:

$$\varphi(\vec{r}, t) = -\gamma(\Delta B(\vec{r})) \cdot t \quad [2.11]$$

where,  $\Delta B(\vec{r})$  represents the variation in the main magnetic field due to the presence of local magnetic field. The MR signal is acquired in form of an echo signal, and as mentioned before the time at which the center of the echo is received is represented as TE (Echo time) (1,2). Hence, the phase accumulated is given as:

$$\varphi(\vec{r}, t) = -\gamma \cdot (\Delta B(\vec{r})) \cdot TE \quad [2.12]$$

The above expression shows the dependence of the accumulated phase signal on the echo time (TE), static main magnetic field ( $B_0$ ) and the nonhomogeneous, spatially varying, local field distribution ( $\Delta B(\vec{r})$ ).

SWI uses very high spatial resolution and it incorporates the phase into the final image. The phase difference in the local tissue between two neighbouring voxels:

$$\Delta\varphi = -\gamma(\Delta B)TE \quad [2.13]$$

The magnetic susceptibility difference is perhaps the only source at this detail to affect the magnetic field. Due to the high spatial resolution, the background field inside a voxel can be regarded as homogeneous (7). The magnetic field variations in Eq. 2.13 can be

represented as the product of the magnetic susceptibility difference ( $\Delta\chi$ ) between the two voxels and the main magnetic field.

$$\Delta\varphi = -\gamma(\Delta\chi \cdot B_0)TE \quad [2.14]$$

The dependence of phase signal on the magnetic susceptibility distribution of a given tissue sample, the phase images offer a unique contrast between the tissue structures such the veins and the surrounding tissue due to the susceptibility difference between the deoxygenated blood in the veins and surrounding tissues is  $\Delta\chi \approx 0.45\text{ppm}$  in SI units (3,4).

#### 2.4.1 Selection of the echo time

According to Eq. 2.14, the phase signal is proportional to time. Hence, in order to obtain a stronger phase response, a higher echo time should be chosen ideally. Usually the focus of phase imaging is to study veins (8,9) and iron deposition (10–12) by acquiring at long TEs (~20ms). However, this long TE approach leads to both macroscopic and microscopic (subpixel size) aliasing. For imaging the veins, an echo time of 20 ms is usually used at 3T so that the phase for a vein parallel to the main magnetic field is close to  $\pi$  (4,13). For a vessel perpendicular to the main field, the phase is  $-\pi/2$  inside the vein, and the maximum is  $3\pi/2$  at the edge of this vein. Hence, phase aliasing occurs at the edge of this vein. Due to partial volume effects, both the phase inside and outside the vein will be integrated across the voxel leading to increased  $T_2^*$  effects. This causes signal loss and the blooming artifact that makes the object appear larger than it really is. Consequently, the smaller veins will appear thicker (up to the size of the voxel) in the magnitude image than it really is and the phase will be an inaccurate estimate of the real phase (14–16). This increase in apparent

size leads to a concomitant underestimate of susceptibility. Despite this, the magnetic moment (proportional to the product of the susceptibility times the volume of the object) will remain an invariant and can be correctly predicted (15–17). If absolute susceptibility is the goal, it would seem more appropriate to set as priority an echo time at which no intra-voxel phase aliasing will occur. Hence, for the structures with strong susceptibility, such as the air/bone-tissue interfaces, lower TEs are more suitable (18). This topic is covered in detail in *Chapter 3*.

#### 2.4.2 Geometric dependence

The net magnetization in an object within a uniform external magnetic field distorts the uniform field outside the object due to its magnetic susceptibility. The expression of phase difference in Eq. 2.14 shows the phase variation between two voxels due to the susceptibility difference between them, but for a bigger region of interest the field variations can be given as (19):

$$\Delta B(\vec{r}) = g_o \Delta \chi B_0 \quad [2.15]$$

where,  $g_o$  is factor dependent on the geometry of an object. Therefore, the spatial distribution of this deviation in the external applied field is a function of the geometry of the object (19). The local field deviation inside and around an object is of interest because it gives rise to local phase differences in MR imaging.

$$\text{and, } \Delta \varphi = -\gamma \cdot (g_o \Delta \chi B_0) \cdot TE \quad [2.16]$$

When discussing the effects of geometry on local field variations, we usually neglect the background field and assume that  $\chi \ll 1$  (4). If information of the object shape is analytically known, we can generate the effective phase information inside and outside the object. For example, the effective variations in the magnetic field, calculated using the Lorentz spherical term and Green's function, inside and outside a cylinder that makes an angle  $\theta$  to the main field are given by:

$$\Delta B_{\text{in}} = \frac{\Delta\chi \cdot B_0(3\cos^2\theta - 1)}{6},$$

$$\Delta B_{\text{out}} = \Delta\chi \cdot B_0 \sin^2\theta \cos 2\phi \frac{a^2}{\rho^2} \quad [2.17]$$

where,  $\Delta\chi = \chi_i - \chi_e$ ,  $\chi_i$  and  $\chi_e$  are the susceptibilities inside and outside the cylinder, respectively (See **Figure 2.5**). The derivation of these solutions can be found in literature (1,20). The analytical solution for a cylinder can be used to understand the field variations for a blood vessel by using the appropriate susceptibility values.

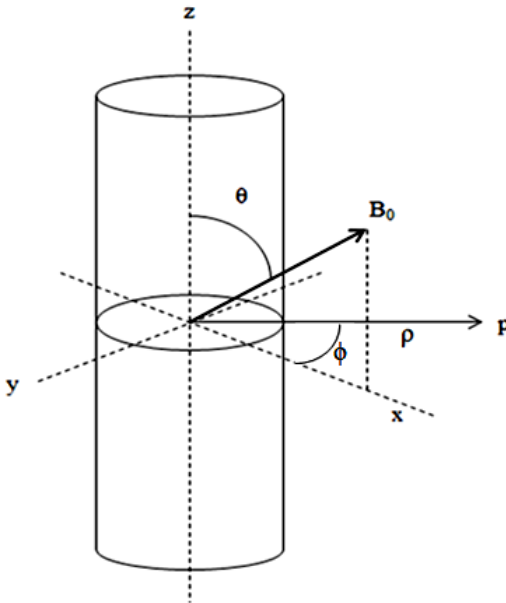


**Figure 2.5.** A cylinder with a radius ‘a’ placed at an angle  $\theta$  to the external magnetic field  $B_0$  and is the polar angle in the x-y plane of the point ‘p’ relative to the external field. The magnetic field variation outside the cylinder at a point ‘p’ with a distance  $\rho$  can be defined by Eq. 2.17.

For more complicated non-uniform structures, the expressions for magnetic field variations around the object are not so straightforward, hence are not available easily (1,3,4). The solution for finding the magnetic field perturbations due to non-uniform geometries will be discussed later in this chapter.

## 2.5 Background Field Removal

The phase images contain information about all magnetic fields, microscopic and macroscopic. The microscopic field information consists of the local susceptibility distribution and the macroscopic field includes the field changes caused by the geometry of the object, such air-tissue interface around the sinuses in the brain, and by inhomogeneities in the main magnetic field. The effective phase behavior can be written as the summation of these fields (1,3,20):

$$\varphi = -\gamma(\Delta B_{\text{main field}} + \Delta B_{\text{CS}} + \Delta B_{\text{global geometry}} + \Delta B_{\text{local field}}) \quad [2.18]$$

where,  $\Delta B_{\text{CS}}$  represents the field variations due to the chemical shift effects. The field variations due to chemical shift are different from the local field variations due to the susceptibility differences, since the latter depends on the geometry of the object (3).

In order to remove the field variations due to the inhomogeneities in the main magnetic field and the global geometries, processing techniques such as Homodyne High pass (HP) filter and sophisticated harmonic artifact reduction for phase data (SHARP) can be applied to the original phase images (3,4,21,22) (See **Figure 2.6**).

### 2.5.1 Homodyne high pass filter

HP-filtered image,  $\rho'(r)$ , is obtained by complex dividing the original image  $\rho(r)$  by a complex image ( $\rho_m(r)$ ) generated from truncating the central  $n \times n$  pixels from the original complex image and zero-filling the elements outside the central  $n \times n$  elements to get the same dimensions as the original image.

$$\rho'(r) = \rho(r)/\rho_m(r) \quad [2.19]$$

The central part of k-space, or frequency domain of the complex image, will contain the low frequency spatial changes of the main magnetic field (22). By generating an image based on the central part of the k-space and complex dividing it from the original complex data, we should get rid of main field inhomogeneity effects. This would also remove most of the unwanted field variations due to global geometries. **Figure 2.6b)** shows that most of the low frequency spatially varying fields that obscure the local inter-tissue phase differences of interest are removed after applying the homodyne high pass filter.

The filtered-phase images, with the background field changes almost completely removed in them, have been very helpful in differentiating one tissue from one another, depending on their susceptibilities (4). However, apart from removing the background field effects, the HP filter also tends to remove some of the physiologically relevant phase information from larger anatomic structures (3,4). This limits the use of filter size larger than  $64 \times 64$  since it introduces adverse effects on bigger objects with homogeneous distribution of susceptibility values inside them.

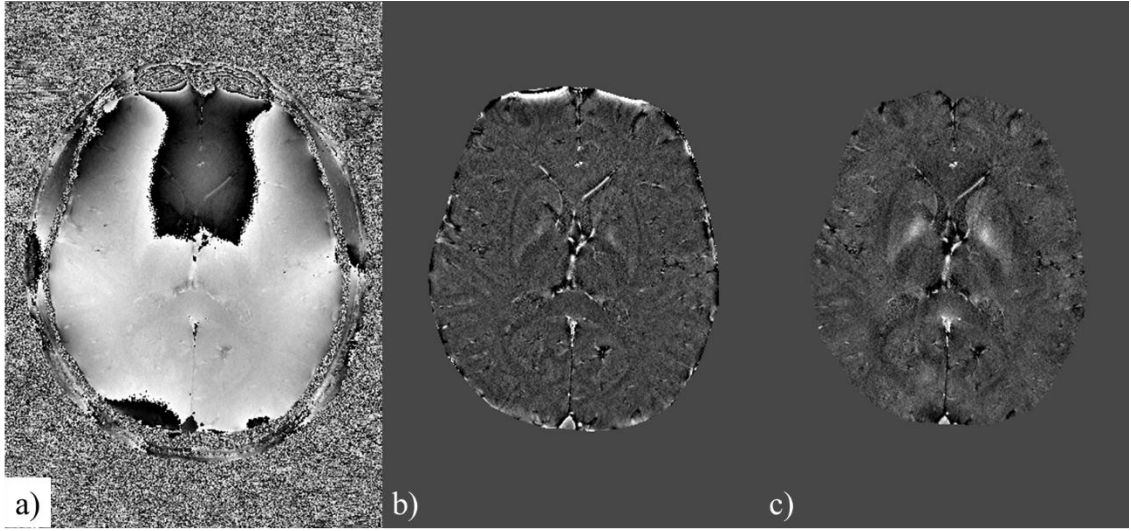


**Figure 2.6.** a) Original unfiltered phase image with imaging parameters: TE=20ms,  $B_0=3T$  with  $0.5 \times 0.5 \times 0.5 \text{mm}^3$  resolution and b) Homodyne high pass filtered phase image with filter size of  $64 \times 64$  pixels, c) phase images processed with SHARP algorithm (radius=6 pixels and th=0.05). The filtered phase images in b) and c) shows the underlying tissue information much clearly due to the reduced background field variations.

### 2.5.2 Sophisticated harmonic artifact reduction for phase data (SHARP)

The field variation, which can be extracted from the phase images using Eq. 2.13, can be considered as a combination of the background field ( $\Delta B_b(\vec{r})$ ) and the local field ( $\Delta B_l(\vec{r})$ ) as:

$$\Delta B(\vec{r}) = \Delta B_b(\vec{r}) + \Delta B_l(\vec{r}) \quad [2.20]$$

SHARP algorithm works on the principal that the background field variations can be approximated as a harmonic component of the phase data in the region of homogeneous susceptibility. Recognizing the background field as a harmonic function, recent studies

have suggested using the spherical mean value property (21,23). The spherical mean value property of the background field implies that:

$$\Delta B_b(\vec{r}) = \Delta B_b(\vec{r}) * s \quad [2.21]$$

where,  $s$  represents a normalized spherical kernel. Applying the spherical kernel to Eq. 2.20 and subtracting it from the original phase, we get

$$\Delta B'(\vec{r}) = \Delta B(\vec{r}) - \Delta B(\vec{r}) * s = \Delta B_l(\vec{r}) - \Delta B_l(\vec{r}) * s \quad [2.22]$$

The term  $\Delta B_b(\vec{r})$  will cancel out due to the relation shown in Eq. 2.21. The result of Eq. 2.22 is deconvolved to compensate for the signal loss to the local field variation caused by the spherical filtering as follows:

$$\Delta B_l(\vec{r}) = \Delta B'(\vec{r}) * (\delta - s)^{-1} \quad [2.23]$$

where,  $(\delta - s)^{-1}$  represents the regularized inverse kernel. An eroded mask of the brain, for example, is applied to remove any unreliable convolution results close to the boundary. The accuracy of the SHARP processed phase images is dependent on both the size of the spherical kernel and the regularization in the deconvolution process. The phase data processed using SHARP algorithm (**Figure 2.6c**) shows the preservation of the local field variations, unlike the considerable loss to the phase of large structures (such as the globus pallidus) caused by the homodyne high pass filter.

## 2.6 Forward Method for Calculating Field Perturbations

As explained earlier, changes in local magnetic field due to relative differences in biological tissue magnetic susceptibilities can provide a unique tissue contrast. The field

variations are dependent on the susceptibility differences and geometry of the object of interest. Hence, methods for estimating this induced static field inhomogeneity due to the presence of an arbitrarily shaped biological tissue in an external homogeneous magnetic field have been of considerable interest right from the early days of MR imaging (24,25). Apart from data correction, such methods can also help us better understand the tissue properties observed in MR experiments through better mathematical simulation of the tissue and its properties. A forward method is used where the induced field perturbation is calculated by convolving the susceptibility distribution with an analytically derived kernel; and this method can be rapidly implemented using fast Fourier transform (FFT) (26,27).

An object, when placed in an external magnetic field ( $B_0$ ), develops an induced magnetization,  $M$ , owing to its magnetic susceptibility property,  $\chi$ , as mentioned briefly in the earlier part of this chapter. The z-component of the induced magnetization is in the direction of the main magnetic field therefore it is much larger than x and y components. For magnetic materials, the net magnetic field  $B_z(\vec{r})$  and induced magnetization  $M_z(\vec{r})$  are related by using Eq. 2.5,

$$M_z(\vec{r}) \approx \frac{\chi(\vec{r})}{\mu_0} B_{0z} \quad [2.24]$$

where,  $\mu_0$  is the absolute permittivity of free space. The expression for the resulting net magnetic field distribution at any point 'r' due to the presence of induced magnetization  $M(\vec{r})$  can be expressed by (4,26):

$$B_z(\vec{r}) = B_0 + \frac{\mu_0}{4\pi} \int_{V'} d^3\vec{r}' \left\{ \frac{3M_z(\vec{r}') \cdot (\vec{z} - \vec{z}')^2}{|\vec{r} - \vec{r}'|^5} - \frac{M_z(\vec{r}')}{|\vec{r} - \vec{r}'|^3} \right\} \quad [2.25]$$

We need to find out the field deviation which can be expressed as  $B_{dz}(\vec{r}) = B_z(\vec{r}) - B_0$ .

Substituting Eq. 2.24 in the Eq. 2.25 we get,

$$B_{dz}(\vec{r}) = \frac{B_0}{4\pi} \int_{V'} d^3\vec{r}' \left\{ \frac{3\chi(\vec{r}) \cdot (\vec{z} - \vec{z}')^2}{|\vec{r} - \vec{r}'|^5} - \frac{\chi(\vec{r}')}{|\vec{r} - \vec{r}'|^3} \right\} \quad [2.26]$$

The above equation can be expressed as a convolution between the susceptibility distribution and a 3D Green's function (4):

$$B_{dz}(\vec{r}) = \frac{B_0}{4\pi} \int_{V'} d^3\vec{r}' (\chi(\vec{r}') \times g(\vec{r})) \quad [2.27]$$

$$\text{where, } g(\vec{r}) = \frac{1}{4\pi} \cdot (3\cos^2\theta - r^2) / r^5 \quad [2.28]$$

In the Fourier domain, the Green's function can be evaluated as (4,20):

$$g(k) = \frac{1}{3} - \frac{k_z^2}{k^2} \quad [2.29]$$

where,  $k^2 = k_x^2 + k_y^2 + k_z^2$  and  $k_x$ ,  $k_y$  and  $k_z$  are the coordinates in k-space. Using the Fourier Transformation (FT) and Inverse Fourier Transform ( $FT^{-1}$ ), Eq. 2.25 can be rewritten as:

$$B_{dz}(\vec{r}) = B_0 \cdot FT^{-1} \left[ FT(\chi(\vec{r}')) \cdot \left( \frac{1}{3} - \frac{k_z^2}{k_x^2 + k_y^2 + k_z^2} \right) \right] \quad [2.30]$$

The deviations in the magnetic field can now be used to predict the phase behavior using Eq. 2.13.

$$\varphi = -\gamma B_0 TE \cdot FT^{-1} \left[ FT(\chi(\vec{r}')) \cdot \left( \frac{1}{3} - \frac{k_z^2}{k_x^2 + k_y^2 + k_z^2} \right) \right] \quad [2.31]$$

The derivation shown above is valid for any arbitrarily shaped, finite, three-dimensional source structure (4,27). This expression is utilized on the brain model to simulate the phase images from the susceptibility maps generated for various geometries in the brain.

The continuous Green's function is derived assuming an infinite field of view. However, all the acquired MR data have a finite field of view (FOV) and are discretized. Thus, we always have a discretized object and a finite FOV to begin with while making such field estimation calculations (4). Hence, to obtain consistent results, a discrete Green's function should be used which is calculated using the finite discrete Fourier transformation of the spatial Green's functions.

The magnetic fields calculated based on a discrete Green's function are aliased (albeit to a lesser degree) in k-space due to finite FOV. The aliasing will increase when the object size increases and becomes comparable to FOV. The problem due to the finite sampling can be alleviated by increasing the size of the field of view relative to the object size (26,28). The forward method can be used accurately even when the object size (i.e., diameter) is as large as 60% of the field of view (4,20).

## **2.7 Susceptibility Mapping**

The ability to quantify local magnetic susceptibility makes it possible to measure the amount of calcium or iron in the body whether it is calcium in breast (29) or iron in the form of non-heme iron (such as ferritin or hemosiderin) or heme iron (deoxy-hemoglobin) (3). Susceptibility maps are produced using the SWI phase data which utilize the

information about the phase behavior around the objects to reconstruct the susceptibility distribution in that region (8).

The expression for reconstructing susceptibility distributions can be derived by rearranging the terms in the Eq. 2.31.

$$\chi(\vec{r}) = \frac{FT^{-1}[g^{-1}(k) \cdot \varphi(k)]}{\gamma \cdot B_0 \cdot TE} \quad [2.32]$$

where  $\chi(r)$  is the reconstructed susceptibility map,  $\varphi(k)$  is the phase information (filtered or unfiltered),  $g^{-1}(k)$  is inverse of the Green's function  $g(k)$  given in Eq. 2.29.

### 2.7.1 Regularized inverse process

The inverse process, however, produces a region in k-space which consists of unreliable information. This region is defined by the condition when  $g(k) = 0$ , i.e. points on or near the conical regions defined by  $k_x^2 + k_y^2 - 2k_z^2 = 0$ . Thus, the inverse process requires regularization to estimate the susceptibility map (8).

The simplest way to solve this inverse problem is to define a k-space truncation threshold (8,30) and construct a regularized inverse filter ( $G_{reg}^{-1}(k)$ ) as:

$$G_{reg}^{-1}(k) = \begin{cases} \left(\frac{1}{3} - \frac{k_z^2}{k^2}\right)^{-1}, & \text{when } \left|\frac{1}{3} - \frac{k_z^2}{k^2}\right| > th \\ \text{sgn}\left(\frac{1}{3} - \frac{k_z^2}{k^2}\right) \left(\frac{1}{3} - \frac{k_z^2}{k^2}\right)^2 th^{-3}, & \text{when } \left|\frac{1}{3} - \frac{k_z^2}{k^2}\right| \leq th \end{cases} \quad [2.33]$$

$G_{reg}^{-1}(k)$  is gradually reduced to 0 as  $\left|\frac{1}{3} - \frac{k_z^2}{k^2}\right|$  approaches 0. The region  $\left|\frac{1}{3} - \frac{k_z^2}{k^2}\right| \leq th$  in k-space is referred to as the ‘‘cone of singularities’’ in this thesis. Although constrained regularizations (21,31–33) have shown good overall results, they require longer

reconstruction times and assumptions about the contrast around a given object. Threshold-based, single orientation regularization methods (TBSO) (22,27,8,30) provide the least acquisition time and the shortest computational time to calculate susceptibility maps. However, their calculated susceptibility maps lead to underestimated susceptibility values ( $\chi$ ) and display severe streaking artifacts especially around structures with significant susceptibility differences, such as veins or parts of the basal ganglia such as globus pallidus.

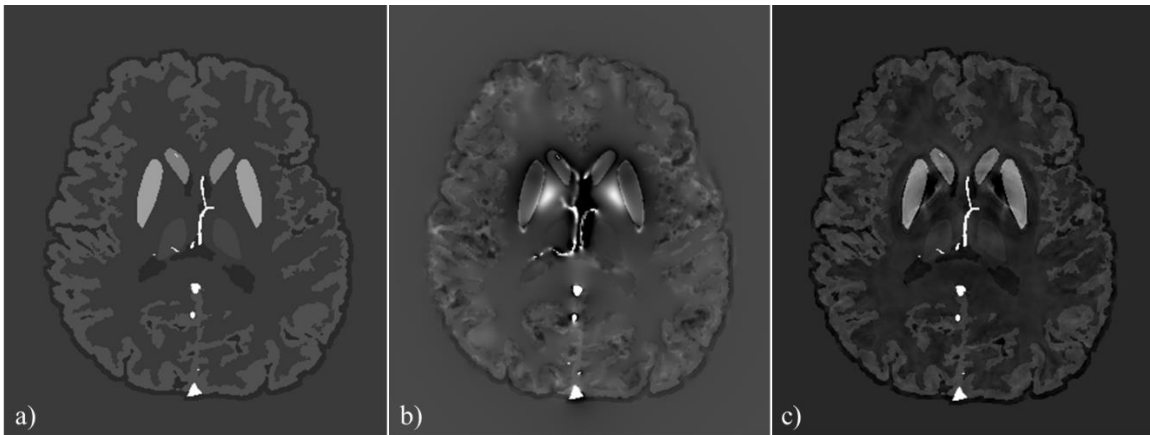


**Figure 2.7.** a) Original susceptibility map (SM) of a 3D brain model, b) Simulated phase generated by using the forward calculation of the magnetic field perturbations (Eq. 2.31) at  $TE=20\text{ms}$  and  $B_0=3\text{T}$ , c) SM reconstructed from phase information in b) using the inverse process (Eq. 2.32 and Eq. 2.33).

**Figure 2.7** demonstrates a simple example of the forward and inverse process to generate simulated phase images and reconstructed susceptibility maps. As we can see, the reconstructed SM is not exactly the same as the original SM (**Figure 2.7a**) and **2.7c**). The next chapter introduces a simulated brain model that is used to understand more about the general phase behavior in a human brain and to demonstrate how accurately the transformation of phase to susceptibility takes place.

### 2.7.2 Iterative SWIM

Due to the ill-posed nature of the inverse problem, streaking artifacts may be present both outside and inside the object of interest, depending on the regularization process that is used (See Eq. 2.33). Streaking artifacts will cause blurring of the edges, and may even be misinterpreted as certain structures when they appear in anatomical regions where such an object may be expected (9). Streaking artifacts can also lead to errors in quantifying the susceptibilities (9). Applying the geometry constrained iterative SWIM method, where the k-space/image domain approach iteratively fills in the relevant information inside the singularity region of the inverse filter, reduces the external streaking artifacts found in the original susceptibility map (9).

The initial susceptibility map is used to threshold the structure(s) of interest. The binary mask extracts the reconstructed susceptibility distribution inside the structure from the initial susceptibility map. The streaking artifacts associated with the structure are usually outside the structure; with less artifacts in the extracted susceptibility map. The k-space of the extracted susceptibility map is used to replace the singularity region in the k-space of the initial susceptibility map. This replacement will provide realistic data points in the singularity region and reconstruction of this new k-space using inverse Fourier transformation will produce a new susceptibility map with significantly reduced streaking artifacts. This procedure is repeated, by considering the new susceptibility map as the initial susceptibility map, until the error in the susceptibility value of the structure of interest between two consecutive iterations converges.

**Figure 2.8 c)** and **2.8e)** demonstrates the reduction in streaking artifacts around the vessels. The iterative method can be used to remove streaking artifacts associated with not only vessels but also other brain structures by selecting the binary masks of different regions of interest, including the basal ganglia structures. The main advantages of this iterative algorithm are its time efficiency and the preservation of susceptibility variation of the veins and other structures with high susceptibility values that are handled by the various thresholds.

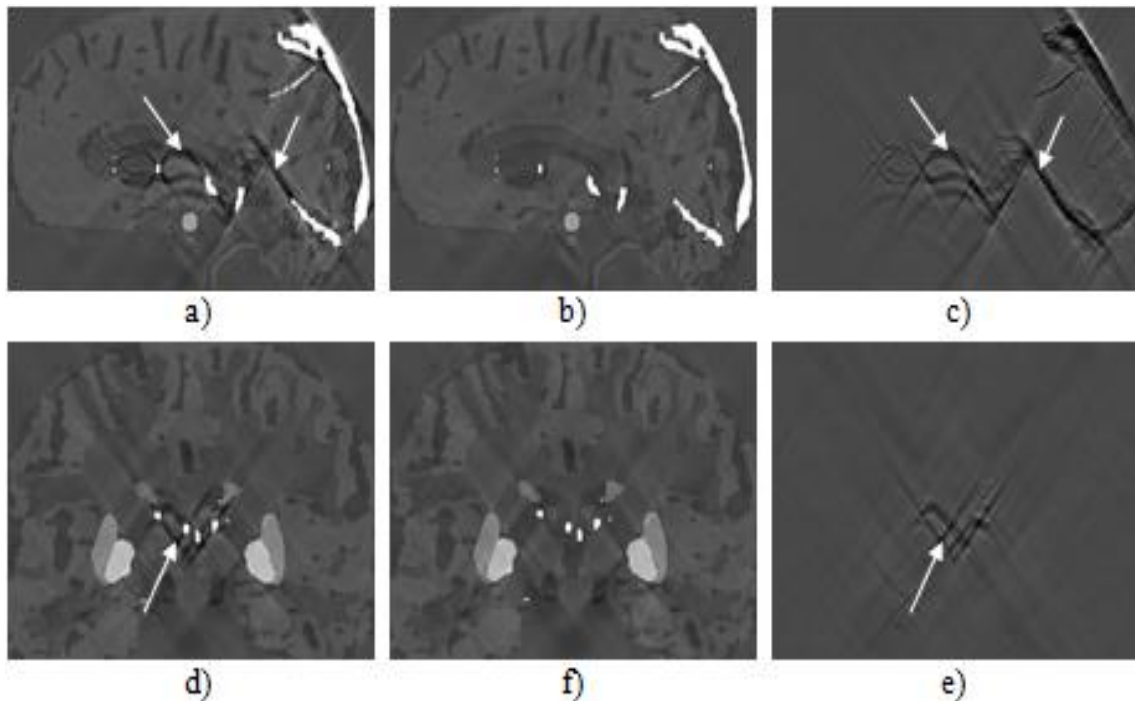


**Figure 2.8.** Susceptibility maps before and after the iterative method using veins as the structure-of-interest. a) Original susceptibility map in sagittal view, b) Iterative result of a) after three iterations, c) The difference map of a) and b), d) Same original susceptibility map as a) in coronal view, e) Iterative result of a) after three iterations in coronal view, f) The difference map of d) and e). White arrows indicate the streaking artifacts seen in the original susceptibility maps a) and d). The difference maps demonstrate that this streaking noise is almost completely removed after three iterations of iterative method.

## References

1. Haacke EM. Magnetic resonance imaging: physical principles and sequence design. New York, NY [u.a.: Wiley-Liss]; 1999.
2. Bernstein MA, King KF, Zhou XJ. Handbook of MRI Pulse Sequences. Elsevier; 2004. 1041 p.
3. Haacke EM, Mittal S, Wu Z, Neelavalli J, Cheng Y-CN. Susceptibility-Weighted Imaging: Technical Aspects and Clinical Applications, Part 1. Am J Neuroradiol. 2009 Jan 1;30(1):19–30.
4. Haacke EM, Reichenbach JR. Susceptibility Weighted Imaging in MRI: Basic Concepts and Clinical Applications. John Wiley & Sons; 2014. 916 p.
5. Edelstein WA, Hutchison JM, Johnson G, Redpath T. Spin warp NMR imaging and applications to human whole-body imaging. Phys Med Biol. 1980 Jul;25(4):751–6.
6. Haase A, Frahm J, Matthaei D, Hänicke W, Merboldt K-D. FLASH imaging: Rapid NMR imaging using low flip-angle pulses. J Magn Reson. 2011 Dec;213(2):533–41.
7. Reichenbach JR, Venkatesan R, Yablonskiy DA, Thompson MR, Lai S, Haacke EM. Theory and application of static field inhomogeneity effects in gradient-echo imaging. J Magn Reson Imaging JMRI. 1997 Apr;7(2):266–79.
8. Haacke EM, Tang J, Neelavalli J, Cheng YCN. Susceptibility mapping as a means to visualize veins and quantify oxygen saturation. J Magn Reson Imaging JMRI. 2010 Sep;32(3):663–76.
9. Tang J, Liu S, Neelavalli J, Cheng YCN, Buch S, Haacke EM. Improving susceptibility mapping using a threshold-based K-space/image domain iterative reconstruction approach. Magn Reson Med. 2013 May;69(5):1396–407.

10. Schweser F, Deistung A, Lehr BW, Reichenbach JR. Quantitative imaging of intrinsic magnetic tissue properties using MRI signal phase: an approach to in vivo brain iron metabolism? *NeuroImage*. 2011 Feb 14;54(4):2789–807.
11. Liu T, Khalidov I, de Rochefort L, Spincemaille P, Liu J, Tsiouris AJ, et al. A novel background field removal method for MRI using projection onto dipole fields (PDF). *NMR Biomed*. 2011 Nov;24(9):1129–36.
12. Li W, Wu B, Liu C. Quantitative susceptibility mapping of human brain reflects spatial variation in tissue composition. *NeuroImage*. 2011 Apr 15;55(4):1645–56.
13. Reichenbach JR, Barth M, Haacke EM, Klarhöfer M, Kaiser WA, Moser E. High-resolution MR venography at 3.0 Tesla. *J Comput Assist Tomogr*. 2000 Dec;24(6):949–57.
14. Cheng Y-CN, Hsieh C-Y, Neelavalli J, Liu Q, Dawood MS, Haacke EM. A complex sum method of quantifying susceptibilities in cylindrical objects: the first step toward quantitative diagnosis of small objects in MRI. *Magn Reson Imaging*. 2007 Oct;25(8):1171–80.
15. Schweser F, Deistung A, Lehr BW, Reichenbach JR. Differentiation between diamagnetic and paramagnetic cerebral lesions based on magnetic susceptibility mapping. *Med Phys*. 2010 Oct;37(10):5165–78.
16. Liu T, Surapaneni K, Lou M, Cheng L, Spincemaille P, Wang Y. Cerebral microbleeds: burden assessment by using quantitative susceptibility mapping. *Radiology*. 2012 Jan;262(1):269–78.
17. Liu S, Neelavalli J, Cheng Y-CN, Tang J, Mark Haacke E. Quantitative susceptibility mapping of small objects using volume constraints. *Magn Reson Med*. 2013 Mar 1;69(3):716–23.

18. Buch S, Liu S, Ye Y, Cheng Y-CN, Neelavalli J, Haacke EM. Susceptibility mapping of air, bone, and calcium in the head. *Magn Reson Med*. 2014 Jul 7;
19. Chu SC, Xu Y, Balschi JA, Springer CS. Bulk magnetic susceptibility shifts in NMR studies of compartmentalized samples: use of paramagnetic reagents. *Magn Reson Med*. 1990 Feb;13(2):239–62.
20. Cheng Y-CN, Neelavalli J, Haacke EM. Limitations of calculating field distributions and magnetic susceptibilities in MRI using a Fourier based method. *Phys Med Biol*. 2009 Mar 7;54(5):1169–89.
21. De Rochefort L, Liu T, Kressler B, Liu J, Spincemaille P, Lebon V, et al. Quantitative susceptibility map reconstruction from MR phase data using bayesian regularization: validation and application to brain imaging. *Magn Reson Med*. 2010 Jan;63(1):194–206.
22. Wang Y, Yu Y, Li D, Bae KT, Brown JJ, Lin W, et al. Artery and vein separation using susceptibility-dependent phase in contrast-enhanced MRA. *J Magn Reson Imaging JMRI*. 2000 Nov;12(5):661–70.
23. Sun H, Wilman AH. Background field removal using spherical mean value filtering and Tikhonov regularization. *Magn Reson Med*. 2014 Mar 1;71(3):1151–7.
24. Case TA, Durney CH, Ailion DC, Cutillo AG, Morris AH. A mathematical model of diamagnetic line broadening in lung tissue and similar heterogeneous systems: Calculations and measurements. *J Magn Reson* 1969. 1987 Jun 15;73(2):304–14.
25. Durney CH, Bertolina J, Ailion DC, Christman R, Cutillo AG, Morris AH, et al. Calculation and interpretation of inhomogeneous line broadening in models of lungs and other heterogeneous structures. *J Magn Reson* 1969. 1989 Dec;85(3):554–70.

26. Salomir R, de Senneville BD, Moonen CT. A fast calculation method for magnetic field inhomogeneity due to an arbitrary distribution of bulk susceptibility. *Concepts Magn Reson Part B Magn Reson Eng.* 2003 Jan 1;19B(1):26–34.
27. Neelavalli J, Cheng Y-CN, Jiang J, Haacke EM. Removing background phase variations in susceptibility-weighted imaging using a fast, forward-field calculation. *J Magn Reson Imaging JMRI.* 2009 Apr;29(4):937–48.
28. Marques J p., Bowtell R. Application of a Fourier-based method for rapid calculation of field inhomogeneity due to spatial variation of magnetic susceptibility. *Concepts Magn Reson Part B Magn Reson Eng.* 2005 Apr 1;25B(1):65–78.
29. Fatemi-Ardekani A, Boylan C, Noseworthy MD. Identification of breast calcification using magnetic resonance imaging. *Med Phys.* 2009 Dec;36(12):5429–36.
30. Shmueli K, de Zwart JA, van Gelderen P, Li T-Q, Dodd SJ, Duyn JH. Magnetic susceptibility mapping of brain tissue in vivo using MRI phase data. *Magn Reson Med.* 2009 Dec;62(6):1510–22.
31. Kressler B, de Rochefort L, Liu T, Spincemaille P, Jiang Q, Wang Y. Nonlinear Regularization for Per Voxel Estimation of Magnetic Susceptibility Distributions from MRI Field Maps. *IEEE Trans Med Imaging.* 2010 Feb;29(2):273–81.
32. Liu T, Liu J, de Rochefort L, Spincemaille P, Khalidov I, Ledoux JR, et al. Morphology enabled dipole inversion (MEDI) from a single-angle acquisition: comparison with COSMOS in human brain imaging. *Magn Reson Med.* 2011 Sep;66(3):777–83.
33. Wharton S, Schäfer A, Bowtell R. Susceptibility mapping in the human brain using threshold-based k-space division. *Magn Reson Med.* 2010 May 1;63(5):1292–304.

# Chapter 3: Susceptibility Mapping of Air, Bone and Calcium in the Head<sup>2</sup>

## 3.1 INTRODUCTION

Proton magnetic resonance (MR) imaging provides excellent contrast between tissues thanks to the presence of water as well as numerous independent tissue properties such as relaxation times, magnetization exchange, motion, chemical shift and magnetic susceptibility. The presence of proton molecules in the form of water is imperative to generate an MR signal in human imaging. Regions, such as brain sinuses, which have no signal cannot benefit from any of the usual tissue properties listed above except for susceptibility which usually affects tissues outside the source. Bones, on the other hand, generally have a very short  $T_2^*$ , except for diploë, the internal spongy part present between the compact layers of flat bones.

<sup>2</sup>Most of the contents of this chapter have been adapted with permission (license number: 3618941429267) from: Buch S, Liu S, Ye Y, Cheng YC, Neelavalli J, Haacke EM. *Susceptibility mapping of air, bone, and calcium in the head*. Magn Reson Med. 2014 Jul 7. doi: 10.1002/mrm.25350.

This causes considerable signal loss at conventional echo times (TEs) of greater than 10ms. However, at short TEs (~2.5ms), some signal is evident in the diploë. In this paper, we wish to image structures that have little to no MR signal, but are of clinical interest such as sinuses, bones and teeth. MR phase images contain essential information about local magnetic susceptibility sources in the brain (1–3). Appropriately processed, the phase images can be used to reconstruct the local susceptibility sources creating a new type of contrast in the form of susceptibility maps (4–6). Usually, the focus of susceptibility mapping has been on structures within the brain such as the basal ganglia, midbrain, veins and grey matter (5,7,8). Compared with these structures, the sinuses and the bones outside the brain have much stronger response to the magnetic field (9). These strong susceptibility sources, especially the air in the sinuses, usually create major non-local phase components, confounding the extraction of the phase information of the local tissues in the brain (4). In the past, every effort has been made to reduce such “phase artifacts” introduced by the sinuses (4,9–11). In fact, the susceptibility maps of these sinuses can be generated from the phase as well.

Previous studies have utilized the phase inside the brain (excluding the skull) only to generate a distribution of all the dipole sources outside the brain which is then used to remove the background field (11). However, the resulting susceptibility distribution does not reflect the susceptibilities of those various structures outside the brain accurately, since it represents susceptibility distribution generated only from phase behavior found in intracranial tissues. The main advances presented herein include: preserving the phase information within the tissue outside the brain (i.e., the skull and its associated tissue which

is usually discarded) and using an iterative susceptibility mapping approach that we introduce in this work by iteratively updating the predicted phase inside an object which has no signal. Specifically, we show that the susceptibility distributions of the sinuses, bones and teeth can be estimated using phase images that come from a high bandwidth gradient echo sequence with a short echo time on the order of few milliseconds to avoid distortion and signal loss at the air-tissue interfaces.

## 3.2 METHODS

### 3.2.1 3D brain model simulations

In order to test this concept, phase images were simulated for a 3D brain model which includes the basal ganglia, midbrain structures, major veins, grey matter (GM), white matter (WM), cerebrospinal fluid (CSF), the sinuses ( $\Delta\chi_{\text{sinus-water}} = +9.4\text{ppm}$ ) and the teeth ( $\Delta\chi_{\text{teeth-water}} = -3\text{ppm}$ ). Susceptibility values of the structures were taken from former studies (7,12) and from the susceptibility maps of *in vivo* human data (in ppm): red nucleus = 0.08, substantia nigra = 0.13, thalamus = 0.03, caudate nucleus = 0.06, putamen = 0.09, globus pallidus = 0.16, veins = 0.45, GM = 0.02, WM = -0.033 and CSF = 0 (susceptibility values are reported relative to that of cerebrospinal fluid). Absolute susceptibility of air,  $\chi_{(\text{v,air})}$ , is  $\sim 0.35\text{ppm}$  while  $\chi_{(\text{CSF})}$  is close to that of water  $\chi_{(\text{water})} = -9.05\text{ppm}$  at 293K (13). The brain model was created in a  $512 \times 512 \times 512$  matrix. The field variation induced by the brain model was calculated through the forward modeling approach (9,14,15), which can be expressed as:

$$\varphi(\vec{r}) = \gamma B_0 T E \cdot \left[ \chi(\vec{r}) * \left( \frac{1}{4\pi} \cdot \frac{3 \cdot \cos^2 \theta - 1}{r^3} \right) \right] \quad [3.1],$$

for a left-handed system.  $\theta$  is the azimuthal angle in the spherical coordinate system,  $r^2 = x^2 + y^2 + z^2$ , and “\*” represents the convolution operator (See *Chapter 2*, section 2.6) (16). The susceptibility maps of the brain model were zero padded to  $1024^3$  in the forward calculation. Phase images were calculated for  $B_0 = 3T$  and  $TE = 2.5ms$ . No filtering or other processing methods were applied to the simulated phase.

Susceptibility maps ( $\chi(\vec{r})$ ) were generated from the phase images ( $\varphi(\vec{r})$ ) using a single orientation QSM method by applying the regularized inverse filter with a truncation threshold of 0.1 (8):

$$\chi(\vec{r}) = \frac{FT^{-1}[g^{-1}(k) \cdot \varphi(k)]}{\gamma \cdot B_0 \cdot TE} \quad [2],$$

where FT represents Fourier transformation and  $\varphi(k) = FT[\varphi(\vec{r})]$ . The Green’s function in the Fourier domain can be represented as  $g(k) = 1/3 - k_z^2/k^2$ , where  $k^2 = k_x^2 + k_y^2 + k_z^2$  and  $g^{-1}(k)$  represents the regularized inverse of the Green’s function in the Fourier domain. In order to reduce the streaking artifacts induced by the singularities in the inverse process, a k-space/image domain iterative algorithm was used to replace the k-space data in the singularity region with reliable information derived from the geometry of the structures of interest (6,8).

### 3.2.2 Phase preservation outside the object of interest

One of the key features of our method is the inclusion of the phase in the tissue surrounding the sinuses. This is achieved by creating a mask,  $M_{head}$ , which is unity for brain and extra-cerebral tissues and zero for all other regions. The original magnitude images

acquired at an echo time of 2.5ms were utilized to generate  $M_{\text{head}}$  by keeping only the pixels whose intensities were above a given value, determined by the noise level in magnitude images. This mask was used to maintain the actual phase around the sinuses and bones. Another mask,  $M_{\text{brain}}$ , was set to one for brain tissue and zero for other regions. Susceptibility maps were generated by applying the brain mask,  $M_{\text{brain}}$ , or the head mask,  $M_{\text{head}}$ , to the simulated phase images and were compared to demonstrate the importance of preserving the extra-cerebral phase. Similarly, a mask,  $M_{\text{air/bone}}$ , was generated which is set to unity inside the sinuses and bones, and zero otherwise.

### 3.2.3 Phase replacement method

Although the iterative algorithm clearly improves the initial inversion results by increasing the accuracy of the susceptibility values and reducing the streaking artifacts, there is a considerable underestimation/bias seen in the measured  $\Delta\chi$  values inside the sinuses. The phase inside the sinuses is nulled using the  $M_{\text{head}}$  mask to generate:

$\varphi' = \varphi \cdot M_{\text{head}}$ . The external phase provides only partial information to reconstruct the local susceptibility.

In order to further improve the inversion result, the missing phase information inside the sinuses ( $\varphi'_{s(\text{inside})}$ ) was replaced with that generated from the forward field calculation using the current susceptibility distribution ( $\chi_i$ ) of the sinuses (9). The phase inside the structures is replaced iteratively until the susceptibility value inside the object converged. In each phase replacement step, the k-space/image domain algorithm was applied. The susceptibility distributions of the sinuses, bones and teeth were extracted using the mask

$M_{\text{air/bone}}$ . The k-space information of these extracted structures was used to update the missing k-space data inside the singularity region, i.e., where  $|g(k)| < 0.1$ . This process reduces the streaking artifacts caused by the sinuses, which would otherwise contaminate the susceptibility values inside other structures surrounding the sinuses, especially the teeth.

### 3.2.4 Tooth Phantom

In order to evaluate the accuracy of the reconstruction inside an object with no apparent signal, a phantom consisting of a premolar human tooth embedded in 6% agarose gel was made. The calcium in teeth has a very short  $T_2^*$  and low proton density (17,18). The imaging parameters were:  $TE_1 = 2.5\text{ms}$ ,  $TE_2 = 5\text{ms}$ ,  $TE_3 = 7.5\text{ms}$ ,  $FA = 15^\circ$ ,  $TR = 12\text{ms}$ ,  $BW = 473\text{Hz/pixel}$  and voxel size =  $0.7 \times 0.7 \times 1.4\text{mm}^3$ .

### 3.2.5 In vivo MR data acquisition

The *in vivo* MRI data were acquired from four healthy volunteers at three in-phase TE values for water and fat signals. The scans were run sagittally using a standard 3D SWI sequence, with whole neck-brain coverage on a 3T Verio scanner (Siemens Healthcare, Erlangen, Germany). The imaging parameters were the same as those in the tooth phantom study.

### 3.2.6 In vivo data processing

The following steps were performed to generate susceptibility maps for the sinuses, bones and teeth (see **Figure 3.1**):

1) For *in vivo* data, there is a spatially-variable phase offset term ( $\varphi_0$ ) present, along with the TE dependent phase ( $\varphi$ ), which will affect the accuracy of the QSM reconstruction (10,19,20).

$$\varphi' = \varphi + \varphi_0 \quad [3],$$

The multi-echo sequence uses a rephased-dephased-rephased readout gradient pattern. We selected the two echoes with rephased readout gradient to eliminate any inconsistencies in the phase offset term and the eddy current effects.  $\varphi_0$  can be calculated using the phase data acquired at TE = 2.5ms ( $\varphi'_{2.5}$ ) and TE = 7.5ms ( $\varphi'_{7.5}$ ) through complex division:

$$\varphi_0 = \left[ \arg \left( e^{i \cdot 3 \cdot \varphi'_{2.5}} / e^{i \cdot \varphi'_{7.5}} \right) \right] / 2 \quad [4],$$

A 3 by 3 median filter was applied to reduce the noise. Then,  $\varphi_0$  was removed from the original TE = 2.5ms data:

$$\varphi_{2.5} = \arg \left( e^{i \cdot \varphi'_{2.5}} / e^{i \cdot \varphi_0} \right) \quad [5].$$

A 3D guided phase unwrapping algorithm was used to unwrap the resultant 2.5ms data (21). The remnant phase effects due to global geometry of the head were reduced by quadratic fitting. Using higher order fit may remove relevant phase behavior of the global structures, such as sinuses.

2) A mask with zero for regions inside the sinuses and regions outside the head, and unity for brain tissue and extra-cerebral tissues,  $M_{\text{head}}$ , was generated from the original

magnitude images using a threshold determined by the noise level. This mask was applied to remove noisy pixels from the phase data;

3) Susceptibility maps were generated using the resultant phase images from Step 2, using Equation [2] with the regularization threshold of 0.1 (8). As mentioned in *Chapter 2*, the geometry constrained iterative method was utilized, where the k-space/image domain approach iteratively fills in the relevant information inside the singularity region of the inverse filter reducing the streaking artifacts found in the original susceptibility map. This relevant information is extracted from a structure of interest and as the filled in information is only pertaining to that particular structure, it should not change the distribution of the other structures nor does it use a low pass filter which would cause blurring. The phase inside the sinuses, bones and teeth was updated using the forward calculated phase at each iteration step, as described in section 3.2.3.

The mask,  $M_{\text{air/bone}}$ , generated using the magnitude images was used as a constraint to keep only those parts of the 3D data that were clearly sinus/bone but not tissue. The iterative algorithm was stopped when the relative change ( $\beta$ ) between the susceptibility maps obtained from previous and from the current iteration was sufficiently small at less than 5%. The relative change in the susceptibility maps was calculated as:  $(\chi_i - \chi_{i-1})/\chi_i$ , where  $\chi_i$  and  $\chi_{i-1}$  are the mean values of the susceptibility distributions inside a region-of-interest (ROI) within the sinuses, for the current and the previous iterations, respectively. Mean susceptibility values of sinuses, bones and teeth were measured using predefined ROIs. The original magnitude images were used as a reference for the ROIs as the sinuses, bones and teeth have no discernible MR signal in the magnitude image.

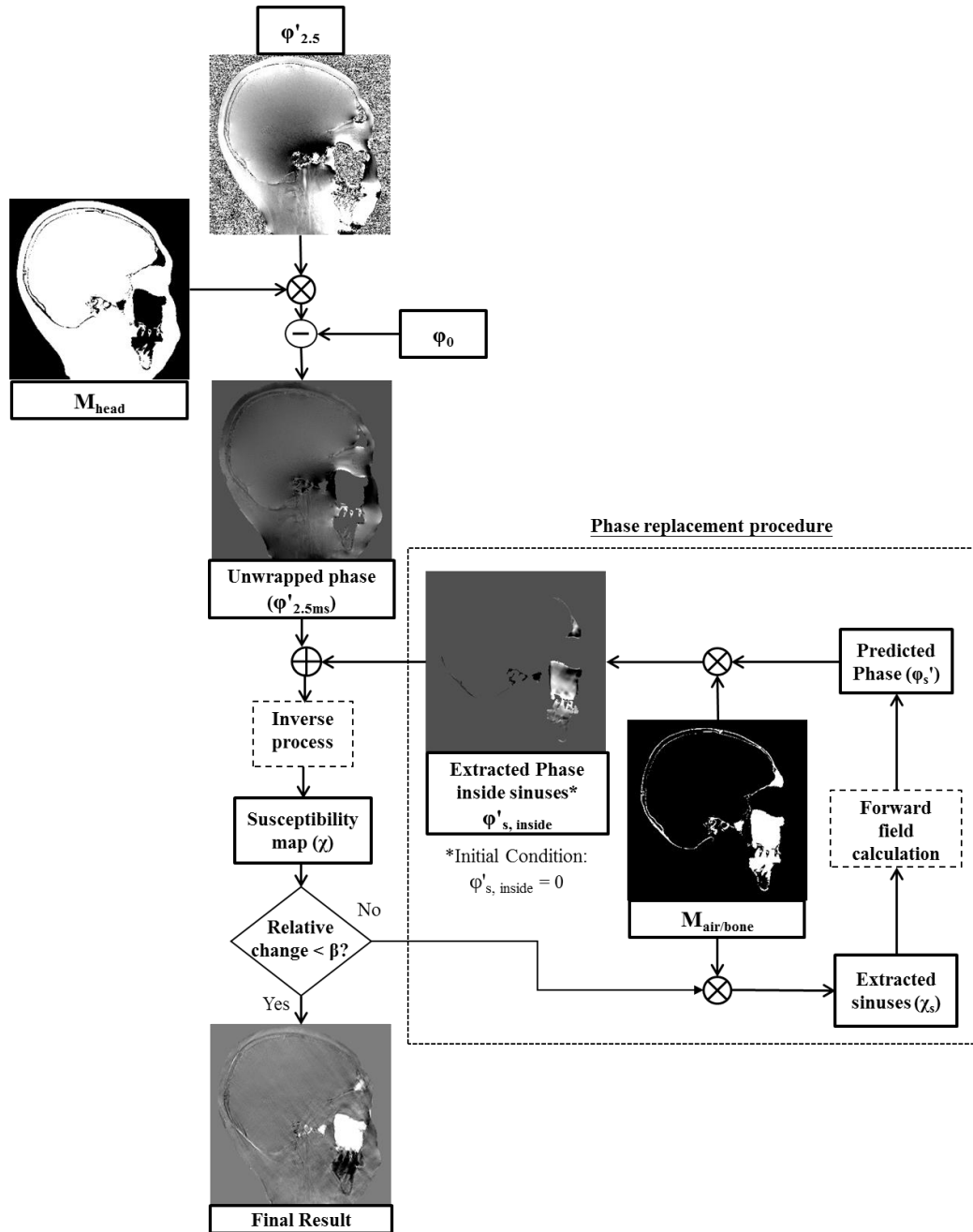


**Figure 3.1.** Illustration of the proposed sinus mapping process using short TE and phase replacement method. Phase replacement steps are repeated until the relative change of the mean susceptibility inside the sinuses is less than some chosen value of  $\beta$ . The mask,  $M_{\text{head}}$ , is used to remove the noisy pixels from phase images, whereas  $M_{\text{air/bone}}$  represents the mask of structures-of-interest for phase replacement process (in this case: sinuses, bones and teeth).

### 3.2.7 Background field removal

Outside of mapping the sinuses, bones and teeth, another application of this method is the removal of global phase effects caused by these strong susceptibility sources. Magnetic field perturbations induced by the extracted sinuses and bones were predicted by using the forward process (see Eq. (1)) with  $TE = 7.5\text{ms}$  and  $B_0 = 3\text{T}$  (9,14). The predicted phase was subtracted from the original phase data acquired at  $TE = 7.5\text{ms}$ .

In the final step, the conventional homodyne high pass filtering (with  $32 \times 32$  filter size) and sophisticated harmonic artifact reduction for phase (SHARP) data algorithm results were compared with the improved result after subtracting the background field predicted from the susceptibility maps of sinuses and bones (10,22).

### 3.3 RESULTS

**Figure 3.2a** shows a  $T_1$  image as part of the 3D dataset that is used to create a 3D numerical model (**Figure 3.2b**). The predicted field perturbation are shown in **Figure 3.2c** that are generated using Eq. 3.1. The results from the brain model simulations using different masks for the brain only,  $M_{\text{brain}}$ , versus whole head,  $M_{\text{head}}$ , are shown in **Figure 3.3**. Clearly, keeping the information from the skull region outside the brain has a major impact on the reconstruction of the sinus and bone susceptibilities.

Susceptibility maps generated from the tooth phantom showed a range of susceptibility values inside the tooth of  $\Delta\chi_{(\text{teeth-tissue})} = -3.1 \pm 1.2$  ppm (**Figure 3.4**). Similar to the simulation result shown in **Figure 3.6**, the first and second iterations were responsible for most of the changes in mapping out the susceptibility values inside the tooth.

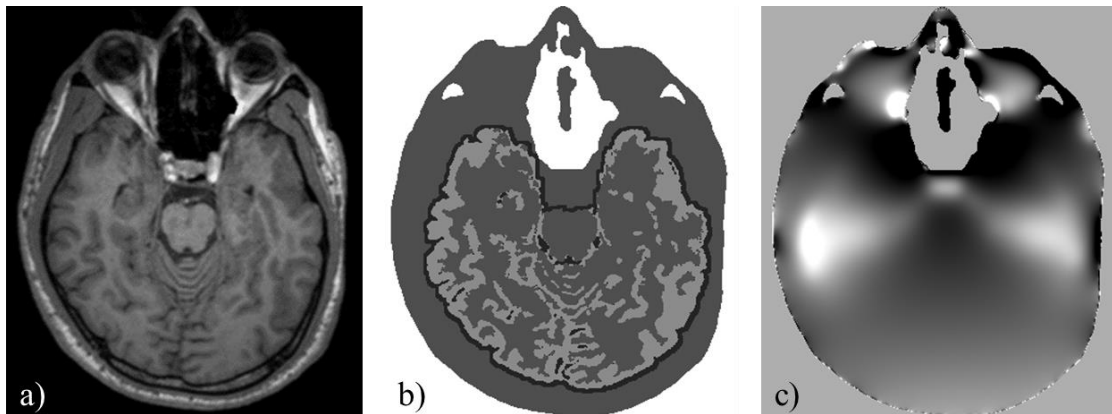


**Figure 3.2.** Simulation of the phase behavior using a 3D numerical model. a) In vivo  $T_1$ -weighted data used to generate the 3D model, b) 3D numerical brain model, and c) simulated phase of the air-tissue interfaces using Eq. 9.

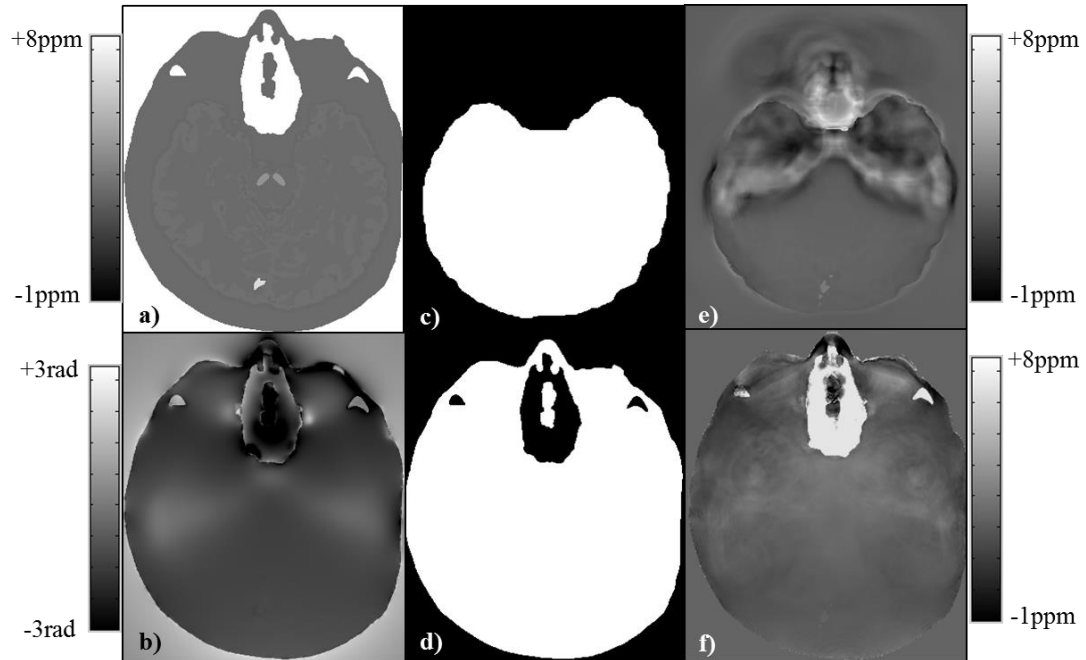


**Figure 3.3.** a) 3D brain model used to test the proposed concept; b) simulated phase image generated from a) by using a forward calculation ( $TE=2.5\text{ms}$  and  $B_0=3\text{T}$ ); c) brain mask ( $M_{\text{brain}}$ ); d) head mask ( $M_{\text{head}}$ ); e) measured susceptibility map resulting from the phase simulation keeping phase only inside the brain, by using the  $M_{\text{brain}}$  mask; and f) measured susceptibility map resulting from the phase simulation using phase information from all tissues surrounding the sinuses inside the head, by using the  $M_{\text{head}}$  mask. Note the major improvement in the shape and susceptibility of the ethmoid sinus.

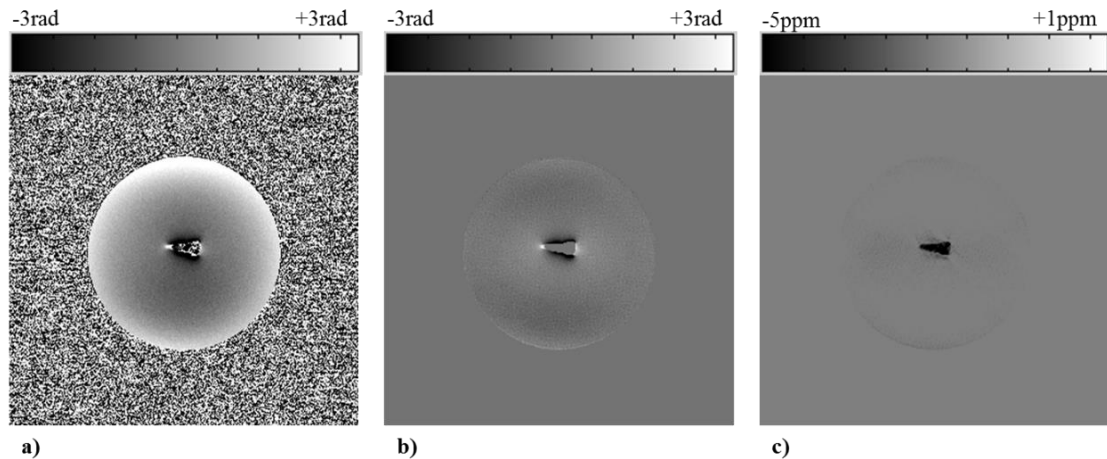


**Figure 3.4.** Susceptibility reconstruction of the tooth phantom. a) Original phase image at  $TE=2.5\text{ms}$ , b) processed phase image and c) reconstructed susceptibility map of the tooth

phantom generated after five phase replacement iterations. The mean susceptibility value inside the tooth is measured as  $\Delta\chi_{(\text{teeth-tissue})} = -3.1 \pm 1.2$ .

The reconstructed susceptibility maps, along with the magnitude images for the *in vivo* data are shown in **Figure 3.5**. The sagittal whole brain coverage provides more phase information especially around the mastoid sinuses. The measured susceptibility value inside the sinuses was increased in each iteration step, as shown in **Figure 3.6**.

The mean susceptibility converged at around +9.4ppm, the value originally assigned to the sinuses in the numerical brain model. It was noted that the standard deviation of the distribution was the least after the fourth iteration. This is confirmed by the results from the *in vivo* data shown in **Table 3.1**, which demonstrates the change in the susceptibility reconstruction with respect to the number of phase replacement iterations. According to this table, the relative change of 10%, 5% and 1% will require two, three and five phase replacement iterations, respectively. For this study, the phase replacement step was terminated after five iterations. Each iteration of the phase replacement method takes approximately 38 seconds for a matrix size of 512×512×256 on MATLAB (64-bit Windows system, 16GB RAM, Intel i7 CPU with 3.4GHz speed).

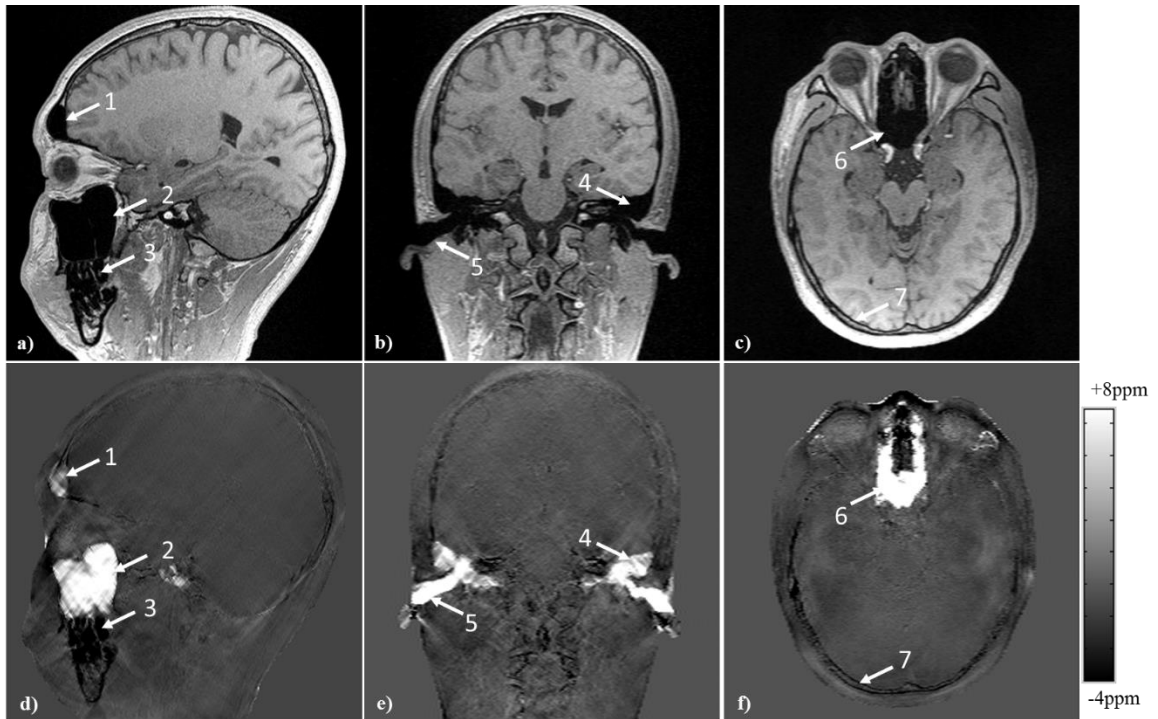


**Figure 3.5.** Comparison of the magnitude images (a, b and c) and susceptibility maps (d, e and f) in all three views, showing agreement spatially between the sinuses and teeth in the original magnitude images and their reconstruction in the susceptibility maps. Structures are identified by the white arrows: 1 – Frontal sinus, 2 – maxillary sinus, 3 – teeth, 4 – mastoid sinus, 5 – ear canal, 6 – ethmoid sinus, 7 – occipital skull bone.

**Table 3.1.** Mean susceptibility value ( $\Delta\chi_{(\text{sinus-tissue})}$ ), standard deviation and relative change, inside the sphenoid sinus of a healthy volunteer, as a function of the number of phase replacement iterations.

	<i>Phase replacement iterations</i>					
	Initial result	1	2	3	4	5
<b>Mean susceptibility (in ppm)</b>	6.28	7.90	8.60	8.89	9.10	9.16
<b>Standard deviation (in ppm)</b>	1.9	1.8	1.7	1.7	1.6	1.5
<b>Relative change of the mean (in %)</b>		23.8	8.9	3.4	2.2	0.7

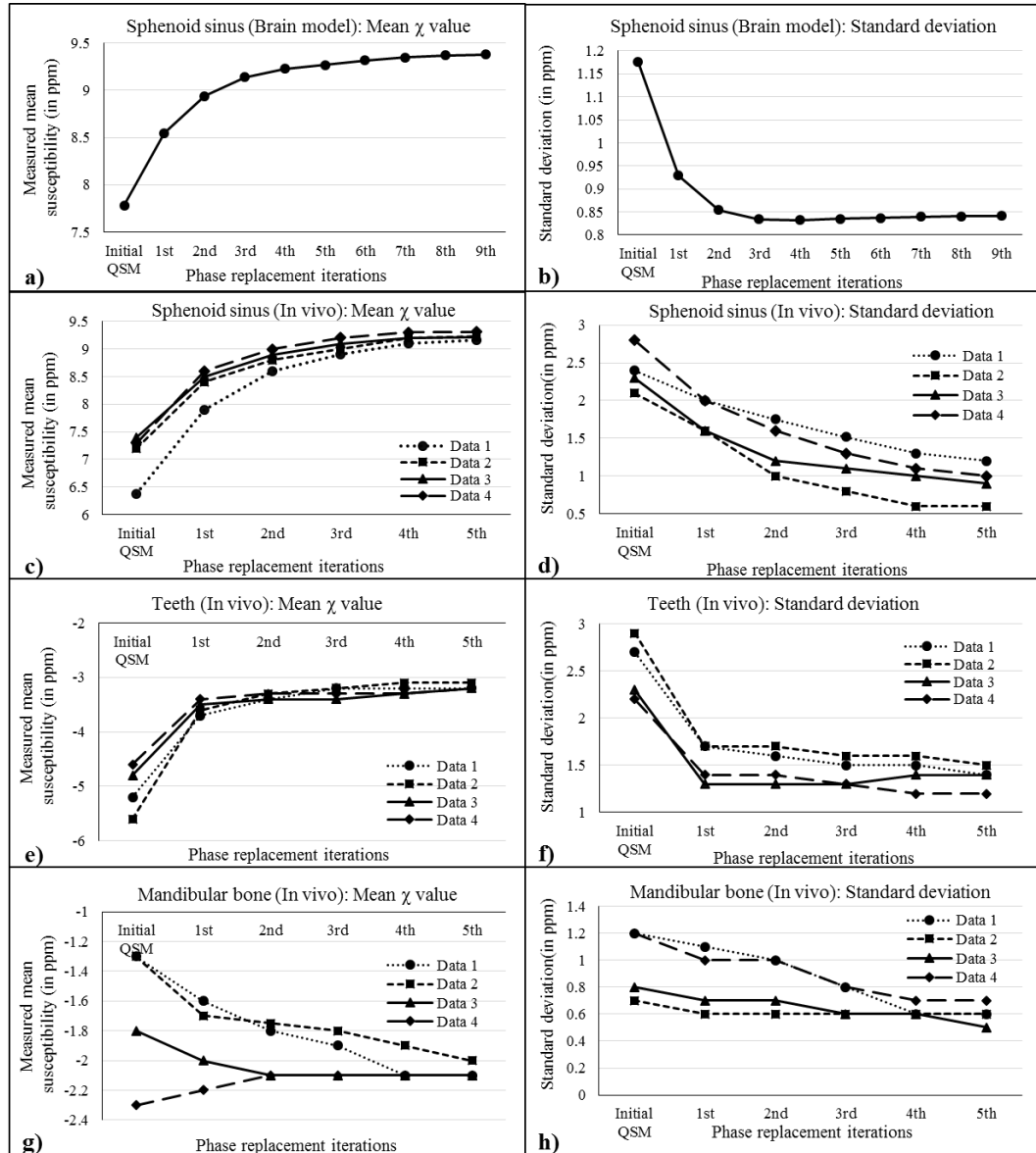


**Figure 3.6.** Measured mean susceptibility values and standard deviations inside the sphenoid sinus from the brain model (a and b); along with sphenoid sinus (c and d), teeth (e and f) and bone (g and h) from the in vivo data.

The results from the actual imaging data show good delineation of sinuses and teeth due to the preservation of phase in the skull and by updating the internal phase. Table 3.2 shows the susceptibility values for the different structures in four different healthy subjects.

**Table 3.2.** Measured susceptibility distributions (mean  $\pm$  standard deviation) inside the various sinuses ( $\Delta\chi_{(\text{sinus-tissue})}$ ), skull bone ( $\Delta\chi_{(\text{bone-tissue})}$ ) and teeth ( $\Delta\chi_{(\text{teeth-tissue})}$ ) from the 3D brain model and from the four healthy volunteers. These results were produced with five iterations of phase replacement method.

Structures	Brain	Healthy volunteers			
	Model	1	2	3	4
	Measured $\Delta\chi$ (in ppm)				
Sphenoid sinus	$9.3 \pm 0.6$	$9.1 \pm 1.3$	$9.2 \pm 0.6$	$9.2 \pm 1.0$	$9.3 \pm 1.1$
Maxillary sinus	$9.3 \pm 0.7$	$9.5 \pm 1.5$	$9.2 \pm 0.9$	$9.2 \pm 1.0$	$9.4 \pm 1.5$
Ethmoid sinus	$9.2 \pm 0.8$	$9.0 \pm 1.8$	$9.2 \pm 0.9$	$8.7 \pm 1.4$	$8.8 \pm 1.5$
Frontal sinus	$7.5 \pm 1.1$	$7.4 \pm 1.4$	$4.2 \pm 1.6$	$5.1 \pm 1.9$	$7.9 \pm 1.6$
Mastoid sinus	$9.0 \pm 0.6$	$6.5 \pm 1.3$	$6.6 \pm 1.2$	$6.3 \pm 0.9$	$6.6 \pm 1.5$
Ear canal	-	$9.2 \pm 1.5$	$9.0 \pm 1.1$	$9.1 \pm 1.4$	$8.9 \pm 1.6$
Teeth	$-2.9 \pm 0.4$	$-3.2 \pm 1.1$	$-3.1 \pm 1.0$	$-3.2 \pm 1.2$	$-3.2 \pm 1.1$
Skull – Occipital	-	$-2.0 \pm 0.6$	$-2.2 \pm 0.6$	$-2.1 \pm 0.6$	$-2.1 \pm 0.7$
Skull – Mandible	-	$-2.1 \pm 0.4$	$-2.0 \pm 0.7$	$-2.1 \pm 0.6$	$-2.1 \pm 0.5$

Initially, susceptibility values of  $\Delta\chi_{(\text{sinus-tissue})} = +9.4\text{ppm}$  and  $\Delta\chi_{(\text{teeth-tissue})} = -3.0\text{ppm}$  were assigned to the sinuses and the teeth for the brain model, respectively. Skull bone was not included in the brain model.

The mean susceptibility values in all the sinuses are much higher than other areas of the brain as expected. The mean susceptibility values in the ethmoid, maxillary and sphenoid sinuses range from +8.7ppm to +9.5ppm, while those in the mastoid and frontal sinuses are close to +7ppm. These are all close to the expected value of +9.4ppm for air. The reconstruction of the teeth provides a mean  $\Delta\chi_{(\text{teeth-tissue})} = -3.3\text{ppm}$ , thanks to the preserved phase inside the jaw. This agrees with the susceptibility value measured from the tooth phantom. The mean susceptibility inside a relatively homogeneous region of the skull bone was measured to be  $\Delta\chi_{(\text{bone-tissue})} = -2.1\text{ppm}$ . This agrees with the susceptibility found in a previous study (23). **Figure 3.7** demonstrates the removal of the global field caused by the strong susceptibility structures, such as sinuses and teeth. The profile plots (**Figure 3.7d** and **3.7h**) show the agreement between the original phase behavior at TE = 7.5ms and the predicted field generated from susceptibility maps as depicted in **Figure 3.5**.

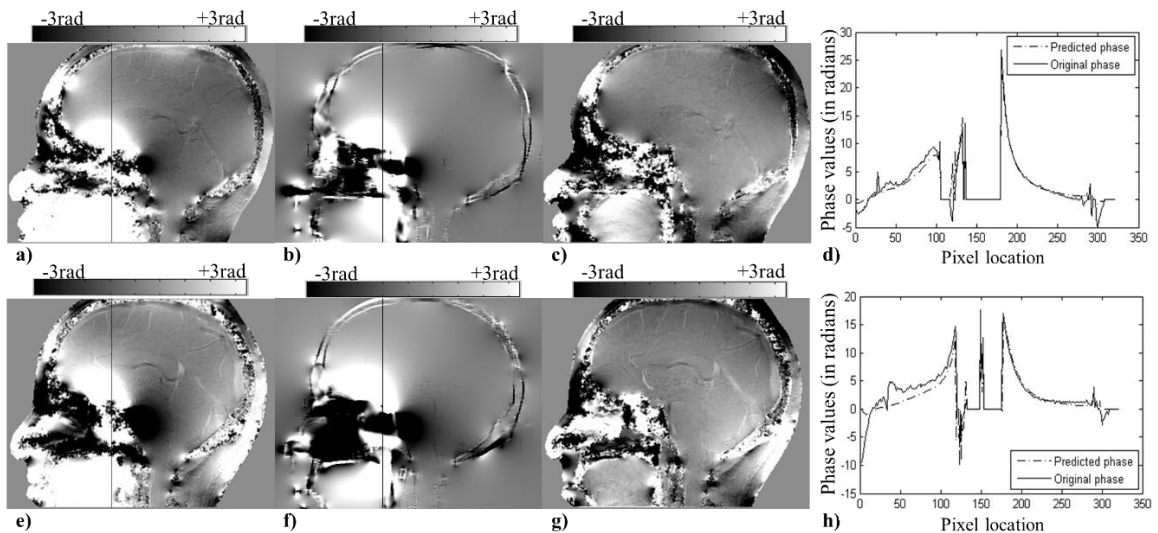


**Figure 3.7.** Background field removal using extracted susceptibility distributions inside the sinuses, bones and teeth for two different volunteers: (a-d) volunteer 1 and (e-h) volunteer 2. a) and e) original phase data acquired at TE = 7.5ms, b) and f) predicted magnetic perturbations TE=7.5ms and  $B_0=3\text{T}$ , c) and g) resultant phase information produced after

subtracting the predicted phase from original phase images. The phase profile plots (d and h), along the black lines, demonstrate that the predicted phase agrees with the original phase behavior outside the sinuses.

**Figure 3.8** demonstrates the advantages of using the susceptibility distribution of sinuses and bones for background field removal over conventional homodyne high-pass filtering and SHARP. In **Figure 3.8a** and **3.8b**, we can see that the remnant background field in the high-pass filtered results has been significantly reduced after the removal of the field predicted using the susceptibility distribution of sinuses and bones (short white arrows). The edges of the brain were eroded in the SHARP processed phase image, but were preserved when a mild high-pass filter was used (long white arrows in **Figure 3.8b** and **3.8c**). In addition, a remnant low-spatial frequency background phase component near the superior sagittal sinus (SSS) can be observed from the SHARP processed phase image (black arrow in **Figure 3.8c**).

The amplitude of this artifact was evaluated by measuring the background tissue in three regions adjacent to the SSS each with 200 pixels. The measured mean and standard error of the affected region (black arrow in **Figure 3.8f**) was  $99 \pm 4$ ppb in the SHARP processed QSM image and  $-21 \pm 4$ ppb in the HPF version, while the mean and standard deviations of the mean in the two adjacent regions were  $60 \pm 5$ ppb and  $-10 \pm 6$ ppb for SHARP processed QSM whereas, for the HPF results they were  $-10 \pm 4$ ppb and  $-12 \pm 4$ ppb. Clearly, there is a consistent susceptibility response for the background tissue for the HPF case but not for the SHARP filtered case (black arrows in **Figure 3.8b** and **3.8e**).

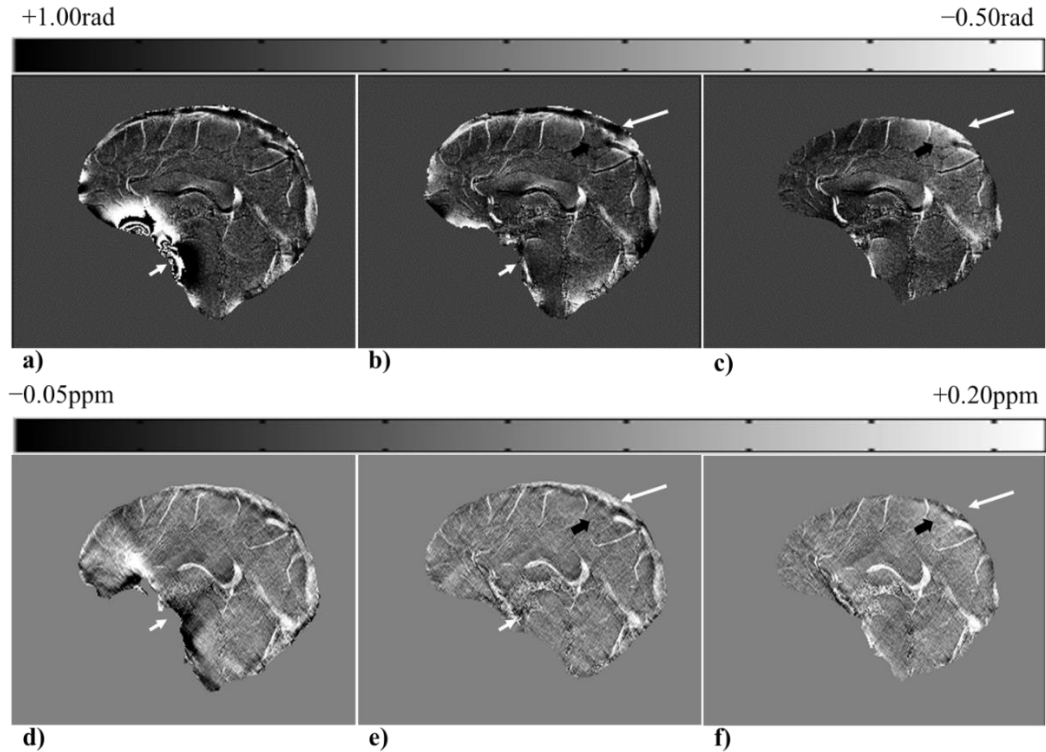


**Figure 3.8.** Improvement in phase processing using susceptibility maps of sinuses and bones. The phase images shown in this figure are acquired at  $TE=7.5\text{ms}$  and field strength of 3T. a) Conventional homodyne high pass (HP) filtering with  $32 \times 32$  filter size, b) homodyne HP filtered image ( $32 \times 32$  filter size) applied after subtracting the forward modeled phase generated from susceptibility maps of sinuses and bones, c) filtered phase image generated using SHARP method. d), e) and f) are the resultant susceptibility maps generated from phase images shown in a), b) and c), respectively. The white arrows demonstrate the areas of improvement using the forward modeled phase, namely the preservation of SSS (long arrow) and significant reduction of phase behavior caused by the air-tissue interfaces (short arrow). The effect of the improper boundary conditions due to the erosion of the brain near the SSS in the SHARP processed phase images is indicated by the black arrows.

### 3.4 DISCUSSION AND CONCLUSIONS

The problem with using phase images directly from a single echo has generally been the presence of unwanted background fields, originating from the air-tissue interfaces, as these effects confound the local phase changes in tissue caused by local susceptibility variations. In this paper, we have focused on imaging these confounding sources such as air (sinuses), bone and calcium (what one might call the *A, B, Cs of QSM*). Using both simulated and real data, we have shown that one can image these objects even though there is no signal inside them in most circumstances.

In this work, we proposed using relatively shorter echo times than the usual echo times used in QSM data acquisition when studying tissue susceptibilities in the brain. Usually the focus of phase imaging and quantitative susceptibility mapping is to study cerebral venous oxygen saturation (4,8) and iron deposition (5,7,24,25). This requires using long TEs (~20ms). However, there are practical problems with this long TE approach leading to both macroscopic and microscopic (relative to pixel size) aliasing. The former can be corrected while the latter leads to  $T_2^*$  signal loss and the blooming artifact that makes the object appear larger than it really is, especially for strong susceptibility objects. This increase in apparent size leads to a concomitant underestimate of susceptibility (26). For the *in vivo* data, the information in the skull is often lost or irrecoverable at long echo times but remains viable at very short echo times. With a high bandwidth sequence using a TE of 2.5ms, we were able to extract the susceptibility distribution while avoiding severe geometric distortion and  $T_2^*$  signal loss in the tissue regions surrounding the sinuses.

One key feature of this method is the use of the phase information around the structure of interest, which plays a critical role in better estimating the susceptibility value of the structure even when there is no signal inside the structure itself. The main idea here is to preserve the phase information surrounding a given structure in the skull and tissue, which is removed in routine QSM methods. By including structures near the edge of the susceptibility sources, a more complete set of phase (field) information is available and the inversion process works much better. To evaluate this concept, we used a 3D human brain model to produce susceptibility maps with and without the phase surrounding the sinuses. Due to the relatively large size of the sinuses and bones, removal of the internal phase, and using only the phase outside the structures (i.e., in the brain only) for QSM, the calculated susceptibility is prone to underestimation. The more spatial phase information provided to the inverse process, the more accurate the estimated susceptibility for the sinuses and bones. The inclusion of the extra-cerebral tissue also makes this technique unique over other susceptibility mapping/background removal techniques, in which the main goal was to remove the field induced by the susceptibility sources outside the brain and thus does not produce faithful geometry information of the sinuses (11). The shape and position of the sinuses as they appear in the susceptibility maps using our approach will depend on the binary masks generated from the magnitude images.

Air has a significantly higher susceptibility than other tissues in the brain. The streaking artifacts associated with the sinuses may contaminate the estimation of the susceptibility distribution inside the surrounding bones and teeth. We found that, using the geometry of the sinuses, the k-space/image domain iterative susceptibility algorithm can largely reduce

the streaking artifacts of the sinuses. This leads to better delineation of the susceptibility distributions of bones and teeth.

The method of phase replacement inside the sinuses provides more accurate phase information for the inversion than assuming zero or some arbitrary constant inside these structures. Because of their short  $T_2^*$ , teeth do not possess adequate signal. The resultant susceptibility maps of the tooth phantom that are generated using our method helps to validate the method of replacing the internal phase and to demonstrate the potential for imaging materials with no signal. The bone or calcium measurements are generally calculated using computed tomography (CT) (27). The results presented in **Figure 3.5** show that we can image the presence of bone and show its diamagnetic behavior, although we make no claim as to the ability to measure bone mineral density with this method at this stage.

Bones are more diamagnetic with respect to other tissues or water. The value we obtained agrees with the magnetic susceptibility of the bones,  $\Delta\chi_{\text{bone-tissue}} = -2.5\text{ppm}$ , found in previous studies (17,24). In addition, the teeth contain a calcified tissue called dentine. The collagen in the bones appears in the form of a trabecular framework, which is absent in teeth, making teeth inherently stronger and denser. Calcium hydroxyapatite (HA) is one of the major constituents of bones and teeth, and as shown in (23) it contributes to the greater diamagnetism in these structures. Teeth are composed of enamel, dentine and cementum. Enamel which is the outermost layer has higher concentration of HA than dentine and bones. Hence, as expected, the susceptibility maps reveal that the teeth are more diamagnetic than bones.

Similarly, keeping signal from tissues around the sinuses made it possible to create realistic susceptibility maps of the sinuses. The mastoid cavity showed lower susceptibilities than the rest of the sinuses. This may be caused in part by the trabecular pattern and the involvement of the air-cells within the sinuses that effectively reduce the overall susceptibility. The presence of a varying amount of sinus fluid should be considered, which will affect the overall susceptibility of the sinus. This can vary from person to person but should be easily handled with the approach described in this paper. The proposed method has shown promising results on the numerical brain model for all the sinuses, except for the frontal sinus (Table 3.2). The fact that the frontal sinus is closer to being parallel to the main magnetic field leads to little or no phase information outside the sinus; and hence shows reduced accuracy in the estimated susceptibility. The residual phase due to imperfect prediction of the forward field surrounding the frontal sinus can be seen in **Figure 3.8**. This orientation dependent drawback can be overcome by acquiring two acquisitions in different orientations (28).

There are several potential applications for mapping high susceptibility tissues outside of air, bones and calcium. First, this approach can be used to predict the air-tissue interface induced field variations and remove their phase effects from the original images. This would allow the use of a much smaller high-pass filter or even no high-pass filter at all. The predicted field using the sinus maps generated from a short echo can be used to process the phase images at any echo time, followed by a mild homodyne high pass filtering. This is particularly efficient for processing multi-echo phase data. On the other hand, processing using SHARP will require phase unwrapping at each echo. Background variation removal

using sophisticated methods, such as SHARP, has the disadvantage of losing the phase information at the edge of the extracted brain. This erosion, which is dependent on the kernel size, discards some important tissues in the cortex of the brain or major veins such as superior sagittal sinus and other cortical veins. Furthermore, unwanted remnant background field can be caused by the improper generation of the brain mask and the inclusion of noisy pixels with unreliable phase values. This can be corrected by the removal of the field predicted using the susceptibility distribution of sinuses and bones prior to applying SHARP. In addition, the accuracy of SHARP also depends on the deconvolution process (29) which may fail due to the erosion of the brain which leaves behind a low spatial frequency background phase component in the processed phase images (30), as observed near the SSS in the SHARP processed phase images (black arrow in **Figure 3.8c**). On the other hand, the use of a mild high-pass filter after the removal of the field induced by the sinuses and bones provides a more uniform response in the processed phase images. This could be advantageous in estimating the susceptibilities of the brain near the SSS. Second, this approach makes it possible to better image the spine and regions surrounding the eyes, which has not yet been done with great success using SWI, QSM or QSM based SWI (31,32). Third, one might consider studying inclusion in material science even for materials that contain no protons as long as they show susceptibility differences compared to the surrounding materials.

In conclusion, by preserving the signal outside the brain itself, phase images at short echo times provide a new approach for imaging high susceptibility objects such as sinuses, bones and teeth in the head. By replacing the phase inside these structures with the predicted

phase from the estimated field and using an iterative reconstruction approach, it is possible to provide a good estimate of the susceptibilities. Finally, these susceptibilities can be used to help remove the unwanted background fields prior to applying either SHARP or HPF.

## References

1. Haacke EM, Xu Y, Cheng Y-CN, Reichenbach JR. Susceptibility weighted imaging (SWI). *Magn Reson Med*. 2004;52(3):612–8.
2. Wu Z, Mittal S, Kish K, Yu Y, Hu J, Haacke EM. Identification of calcification with MRI using susceptibility-weighted imaging: A case study. *J Magn Reson Imaging*. 2009;29(1): 177–82.
3. Haacke EM. *Magnetic resonance imaging: physical principles and sequence design*. First edition; Wiley-Liss; 1999.
4. Haacke EM, Tang J, Neelavalli J, Cheng YCN. Susceptibility mapping as a means to visualize veins and quantify oxygen saturation. *J Magn Reson Imaging*. 2010;32(3):663–76.
5. Shmueli K, de Zwart JA, van Gelderen P, Li T-Q, Dodd SJ, Duyn JH. Magnetic susceptibility mapping of brain tissue in vivo using MRI phase data. *Magn Reson Med*. 2009;62(6):1510–22.
6. Liu J, Liu T, de Rochefort L, et al. Morphology enabled dipole inversion for quantitative susceptibility mapping using structural consistency between the magnitude image and the susceptibility map. *NeuroImage*. 2012;59(3):2560–8.
7. Wharton S, Bowtell R. Whole-brain susceptibility mapping at high field: a comparison of multiple- and single-orientation methods. *NeuroImage*. 2010;53(2):515–25.

8. Tang J, Liu S, Neelavalli J, Cheng YCN, Buch S, Haacke EM. Improving susceptibility mapping using a threshold-based K-space/image domain iterative reconstruction approach. *Magn Reson Med*. 2013;69(5):1396–407.
9. Neelavalli J, Cheng Y-CN, Jiang J, Haacke EM. Removing background phase variations in susceptibility-weighted imaging using a fast, forward-field calculation. *J Magn Reson Imaging*. 2009;29(4):937–48.
10. Schweser F, Deistung A, Lehr BW, Reichenbach JR. Quantitative imaging of intrinsic magnetic tissue properties using MRI signal phase: an approach to in vivo brain iron metabolism? *NeuroImage*. 2011;54(4):2789–807.
11. Liu T, Khalidov I, de Rochefort L, Spincemaille P, Liu J, Tsiouris AJ, Wang Y. A novel background field removal method for MRI using projection onto dipole fields (PDF). *NMR Biomed*. 2011;24(9):1129–36.
12. Li W, Wu B, Liu C. Quantitative Susceptibility Mapping of Human Brain Reflects Spatial Variation in Tissue Composition. *NeuroImage*. 2011;55(4):1645–56.
13. Lide DR. *CRC Handbook of Chemistry and Physics*, 87th Edition. CRC Press; 2006. 2608 p.
14. Koch KM, Papademetris X, Rothman DL, de Graaf RA. Rapid calculations of susceptibility-induced magnetostatic field perturbations for in vivo magnetic resonance. *Phys Med Biol*. 2006;51(24):6381–402.
15. Marques J p., Bowtell R. Application of a Fourier-based method for rapid calculation of field inhomogeneity due to spatial variation of magnetic susceptibility. *Concepts Magn Reson Part B Magn Reson Eng*. 2005;25B(1):65–78.
16. Cheng Y-CN, Neelavalli J, Haacke EM. Limitations of calculating field distributions and magnetic susceptibilities in MRI using a Fourier based method. *Phys Med Biol*. 2009;54(5):1169–89.

17. Horch RA, Nyman JS, Gochberg DF, Dortch RD, Does MD. Characterization of <sup>1</sup>H NMR Signal in Human Cortical Bone for Magnetic Resonance Imaging. *Magn Reson Med.* 2010;64(3):680–7.
18. De Rochefort L, Brown R, Prince MR, Wang Y. Quantitative MR susceptibility mapping using piece-wise constant regularized inversion of the magnetic field. *Magn Reson Med.* 2008;60(4):1003–9.
19. Haacke EM, Petropoulos LS, Nilges EW, Wu DH. Extraction of conductivity and permittivity using magnetic resonance imaging. *Phys Med Biol.* 1991;36(6):723.
20. Kim D-H, Choi N, Gho S-M, Shin J, Liu C. Simultaneous imaging of in vivo conductivity and susceptibility. *Magn Reson Med.* 2013; doi: 10.1002/mrm.24759.
21. Arevalillo-Herráez M, Gdeisat MA, Burton DR. Hybrid robust and fast algorithm for three-dimensional phase unwrapping. *Appl Opt.* 2009;48(32):6313–23.
22. Wang Y, Yu Y, Li D, Bae KT, Brown JJ, Lin W, Haacke EM. Artery and vein separation using susceptibility-dependent phase in contrast-enhanced MRA. *J Magn Reson Imaging.* 2000;12(5):661–70.
23. Hopkins JA, Wehrli FW. Magnetic susceptibility measurement of insoluble solids by NMR: magnetic susceptibility of bone. *Magn Reson Med.* 1997;37(4):494–500.
24. Haacke EM, Cheng NYC, House MJ, Liu Q, Neelavalli J, Ogg RJ, Khan A, Ayaz M, Kirsch W, Obenaus A. Imaging iron stores in the brain using magnetic resonance imaging. *Magn Reson Imaging.* 2005;23(1):1–25.
25. Zheng W, Nichol H, Liu S, Cheng Y-CN, Haacke EM. Measuring iron in the brain using quantitative susceptibility mapping and X-ray fluorescence imaging. *NeuroImage.* 2013;78:68–74.
26. Liu S, Neelavalli J, Cheng Y-CN, Tang J, Mark Haacke E. Quantitative susceptibility mapping of small objects using volume constraints. *Magn Reson Med.* 2013;69(3):716–23.

27. Homolka P, Beer A, Birkfellner W, Nowotny R, Gahleitner A, Tschabitscher M, Bergmann H. Bone mineral density measurement with dental quantitative CT prior to dental implant placement in cadaver mandibles: pilot study. *Radiology*. 2002;224(1):247–52.
28. Liu T, Spincemaille P, de Rochefort L, Kressler B, Wang Y. Calculation of susceptibility through multiple orientation sampling (COSMOS): a method for conditioning the inverse problem from measured magnetic field map to susceptibility source image in MRI. *Magn Reson Med*. 2009;61(1):196–204.
29. Sun H, Wilman AH. Background field removal using spherical mean value filtering and Tikhonov regularization. *Magn Reson Med*. 2014;71(3):1151–7.
30. Zhou D, Liu T, Spincemaille P, Wang Y. Background field removal by solving the Laplacian boundary value problem. *NMR Biomed*. 2014;27(3):312–9.
31. Liu S, Mok K, Neelavalli J, Cheng Y-CN, Tang J, Ye Y, Haacke EM. Improved MR venography using quantitative susceptibility-weighted imaging. *J Magn Reson Imaging*. 2013; doi: 10.1002/jmri.24413.
32. Gho SM, Liu C, Li W, Jang U, Kim EY, Hwang D, Kim DH. Susceptibility map-weighted imaging (SMWI) for neuroimaging. *Magn Reson Med*. 2013; doi: 10.1002/mrm.24920.

# **Chapter 4: Estimation of Phase Change Induced by Blood Flow in Presence of Background Gradients ( $G'$ )**

## **4.1 INTRODUCTION**

Susceptibility weighted imaging (SWI) has been widely used to image venous blood, microbleeds, iron, calcium and any other substances that lead to local susceptibility changes. The MR phase data obtained from a gradient-echo sequence has also been used to perform quantitative susceptibility mapping (1–3). The internal phase for blood vessels is constituted by the moving spins based on the blood flow and it given by Eq. 2.7 (4,5). However, in order to study the local variations caused by susceptibility differences, the

phase term due to flow needs to be suppressed. Therefore, the zeroth as well as first moments of the imaging gradients are nulled for the SWI sequence (4) (See **Figure 2.3** in *Chapter 2*).

Although the phase accumulation due to constant velocity in the presence of imaging gradients is designed to be zero, there are other sources of phase shift for a blood vessel that need to be studied. One of the major sources comes from the perturbations in the main magnetic field induced by the magnetic susceptibility changes at the air/bone-tissue interfaces. These inhomogeneities will lead to an extraneous gradient, despite the perfectly designed flow compensation sequence.

In this chapter, this internal phase term due to blood flow, in presence of these additional unwanted background gradients, was studied using a 3D numerical model, which consists of air-tissue interfaces. In addition, the simulation results were validated using *in vivo* data (double-echo sequence) by using the phase replacement method to generate sinus/bone susceptibility maps (See *Chapter 3*, sections 3.2.3 and 3.2.6) (6). Furthermore, the magnitude data of the first echo were used to identify the major arteries and generate masks. Using the arterial masks, the phase for arteries can be nulled to reduce flow induced artifacts in quantitative susceptibility mapping.

## 4.2 THEORY

### 4.2.1 Evaluating the effect of background gradients on flow compensation

In this section, it is assumed that first gradient moment nulling is applied, and only the components in  $x$  direction are considered for simplicity. The field inhomogeneity ( $\Delta B(x(t))$ ) induced phase of the moving isochromat can be calculated, for a left-handed system, as (4):

$$\varphi(t) = \gamma \int_0^t \Delta B(x(t)) dt \quad [4.1]$$

For a velocity  $\vec{v}$ , the position of the spin isochromat is  $x(t) = x_0 + \vec{v}(x_0)t$ , where  $x_0$  is the initial position. Assuming the velocity is locally constant in time up to TE, we get  $x(t) = x(TE) + \vec{v}(x_0)(t - TE)$ . Eq. 4.1 becomes:

$$\begin{aligned} \varphi(t) &= \gamma \int_0^{TE} \Delta B(x(TE) + \vec{v}(x_0)(t - TE)) dt \\ \varphi(TE) &= \gamma \Delta B(x(TE)) TE - \frac{1}{2} [\gamma \vec{v}(x_0) \cdot \vec{G}'(x(TE)) TE^2] \end{aligned} \quad [4.2]$$

where,  $\vec{G}'(x(TE))$  represents the gradient of field inhomogeneities at  $x(TE)$ :

$$\vec{G}'(x(TE)) = \nabla (\Delta B(x(TE))) \quad [4.3]$$

Traditionally, the phase of an isochromat of spins with motion due to the applied gradient is compensated through gradient moment nulling. However, even with full flow compensation, there is still remnant phase due to the presence of main field inhomogeneities. For a left-handed system, the phase inside a vessel on the phase images acquired with a flow compensated gradient-echo sequence, from Eq. 4.2, is given as:

$$\varphi(\mathbf{r}) = \gamma\Delta B(\mathbf{r})TE - \frac{1}{2}\gamma\vec{v} \cdot \vec{G}'(\mathbf{r})TE^2 \quad [4.4]$$

assuming local constant velocity  $\vec{v}$ , and  $\vec{G}'(\mathbf{r})$  is the background field gradient.

The first term is the phase of stationary tissue, while the second term represents the extra flow-related phase due to the background field gradient  $\vec{G}'(\mathbf{r})$ . It is this phase term that causes failure in flow compensation as well as possible signal decay due to the phase dispersion across a voxel. In the head,  $\vec{G}'(\mathbf{r})$  is dominantly attributed to the air/bone tissue interfaces induced field variations. In order to study the effects of  $\vec{G}'$ , the field variation caused by air/bone-tissue interfaces in the head must be determined. In this chapter, small field variations due to imperfectly shimmed fields are ignored.

#### 4.2.2 Echo shift in the presence of the background gradients

Due to the presence of an extraneous gradient, the acquired echo is shifted from the center of the k-space. **Figure 4.1** shows a simplified, typical read gradient which produces a gradient echo at time TE. When a negative background gradient ( $G_x'$ ) is superimposed to the imaging gradient ( $G_x$ ), the effective dephasing gradient becomes  $-(G_x + G_x')$  whereas the rephasing gradient during the readout, becomes  $(G_x - G_x')$ . Thus in this case, the resultant echo time shifts to the right and increases to TE'. Similarly, in case of a positive background gradient of same strength, the echo time will shift to the left.

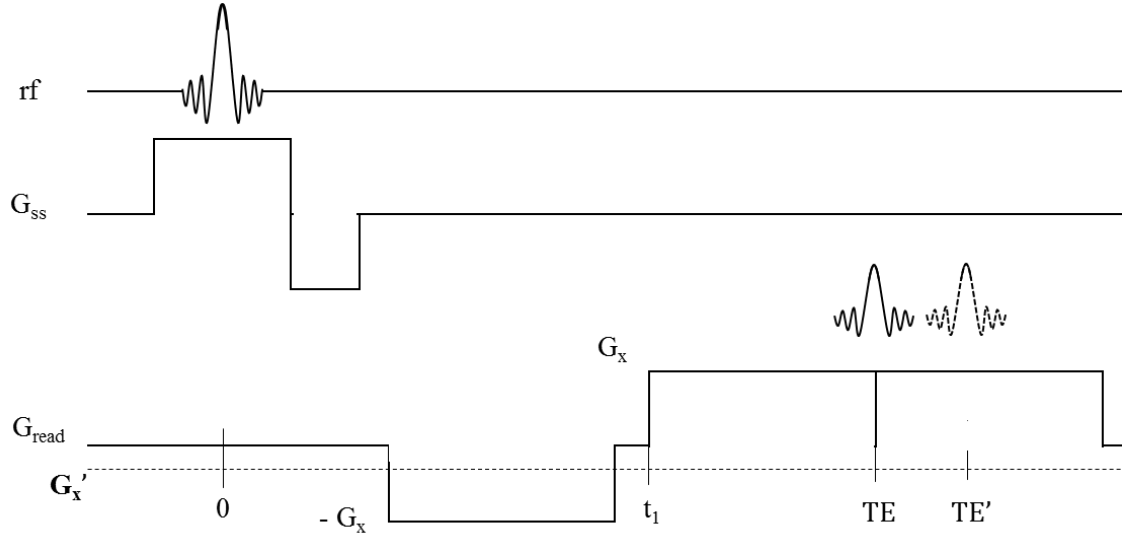


**Figure 4.1.** A negative background gradient ( $G_x'$ ) in the readout direction and the induced echo shift. The center of the sampling period represents the ideal echo time, TE. However, in presence of an extraneous gradient ( $G_x'$ ), the shifted echo occurs at the time  $TE'$ .

Assuming that  $n = N/2$ , where  $N$  is the total number of sampling points, and the sampling interval,  $\Delta t = T_s/N$ , where  $T_s$  is the total sampling time. The ideal time of echo, TE, can be expressed as:  $TE = t_1 + n\Delta t$ , where  $t_1$  marks the beginning of the sampling period (See **Figure 4.1**).

When the echo occurs at  $t = TE'$ , the effects of dephasing and rephasing gradients null each other, such that:

$$\int_0^{TE'} G_x^{\text{total}}(t) dt = 0, \quad [4.5]$$

$$\text{where, } TE' = t_1 + n'\Delta t \quad [4.6]$$

Solving for equality in Eq. 4.5 by referring to **Figure 4.1**:

$$-G_x n \Delta t + G_x n' \Delta t + G'_x (t_1 + n \Delta t) = 0 \quad [4.7]$$

From Eqs. 4.6 and 4.7, TE' is given by

$$TE' = \frac{G_x}{G_x + G'_x} \cdot (t_1 + n \Delta t) = \frac{G_x}{G_x + G'_x} \cdot TE \quad [4.8]$$

Assuming that  $n_{\text{shift}}$  is the number of sample points by which the echo is shifted, ( $n_{\text{shift}} \Delta t = TE' - TE$ ). From Eq. 4.8, we get

$$n_{\text{shift}} \Delta t = -\frac{G'_x}{G_x + G'_x} \cdot TE$$

$$\text{For } |G_x| \gg |G'_x|, \quad n_{\text{shift}} \approx \frac{G'_x TE}{G_x \Delta t} \quad [4.9]$$

When  $|n_{\text{shift}}| \geq 2n$ , the echo will be completely out of the sampling window. This will cause the voxel signal to disappear.

An echo shift of  $n_{\text{shift}} \Delta t$  corresponds to a shift in k-space by,  $k_{\text{shift}} = n_{\text{shift}} \Delta k$  (4). According to the Fourier transform shift theorem, a shift in k-space causes a phase dispersion across a given voxel by:

$$\Delta \varphi = -2\pi k_{\text{shift}} \Delta x = -2\pi n_{\text{shift}} / N \quad [4.10]$$

Due to the phase distribution  $\Delta \varphi$  (ranging from  $-\Delta \varphi / 2$  to  $+\Delta \varphi / 2$ ) across the voxel, the resultant voxel signal is dephased signal:

$$\rho_n = \rho_0 \left[ \frac{1}{\Delta \varphi} \int_{-\Delta \varphi}^{\Delta \varphi} e^{i\varphi} d\varphi \right] = \rho_0 \text{sinc}(\Delta \varphi / 2) \quad [4.11]$$

where,  $\rho_0$  is the homogeneous spin density.

## 4.3 METHODS

### 4.3.1 Background gradient simulations

In the head, the background field is mainly induced by the air-tissue interfaces. In order to study these phase changes due to the presence of background gradients ( $G'$ ), the effects of global field changes caused by air-tissue interfaces in the head must be evaluated (small field variations due to imperfectly shimmed fields are ignored).

In order to study these background gradients, a map of field perturbations was simulated from a 3D model of the susceptibility ( $\chi(\vec{r})$ ) generated from a  $T_1$ -MPRAGE data of a normal brain, by assuming the susceptibility difference of  $\Delta\chi_{\text{air-water}} = +9.4\text{ppm}$ . Absolute susceptibility of air,  $\chi_{(\text{v,air})}$ , is  $\sim 0.35\text{ppm}$  while  $\chi_{(\text{CSF})}$  which is close to that of water,  $\chi_{(\text{v,water})} = -9.05\text{ppm}$  at  $293^\circ\text{K}$  (7). The brain model is created using a  $512 \times 512 \times 512$  matrix. The field variation induced by the brain model can be calculated through the forward modeling approach (8–10), which is expressed as:

$$\Delta B(\vec{r}) = \left[ \chi(\vec{r}) * \left( \frac{1}{4\pi} \cdot \frac{3\cos^2\theta - 1}{r^3} \right) \right] \quad [4.12]$$

for a left-handed system. Here,  $\theta$  is the azimuthal angle in the spherical coordinate system,  $r^2 = x^2 + y^2 + z^2$ , and “\*” represents the convolution operator (11).

The background gradient  $G'$  can be calculated from the field maps, using Eq. 4.3. The phase induced by the blood flow in presence of background gradient  $G'$  inside a vessel were generated as:

$$\varphi_{G'} = -\frac{1}{2} \gamma [\overline{G'_x} \cdot \overline{v_x} + \overline{G'_y} \cdot \overline{v_y} + \overline{G'_z} \cdot \overline{v_z}] T_E^2. \quad [4.13].$$

#### 4.3.2 Validation using *in vivo* data

Two double-echo data were acquired for 1) predicting the background gradients and, hence, 2) validating the prediction of the flow induced internal phase for the arteries in a data acquired using a flow-compensated sequence. The first double-echo data was collected with a relatively lower resolution of  $1.3 \times 1.3 \times 1.3 \text{mm}^3$  and no flow-compensation, to generate the sinus maps. The imaging parameters used were:  $TE_1/TE_2 = 2.5/5 \text{ms}$ ,  $TR = 20 \text{ms}$ ,  $FA = 13^\circ$ , bandwidth = 531 Hz/pxl. The second double-echo data was acquired with higher resolution of  $0.63 \times 0.63 \times 1.3 \text{mm}^3$ , fully flow-compensated with imaging parameters:  $TE_1/TE_2 = 7.5/17.5 \text{ms}$ ,  $TR = 25 \text{ms}$ ,  $FA = 15^\circ$ , receiver bandwidth = 480 Hz/pixel (for each TE) and matrix size of  $384 \times 384 \times 144$ . The echo shifts was corrected by detecting the maximum value across k-space of the given data, and shifting the k-space such that this peak value, representing the center of the echo, was assigned to central element of the matrix (12).

The sinus/bone susceptibility maps were produced from the low resolution, short TE data using the phase replacement method (6). The sinus maps were registered and interpolated to match the imaging resolution and FOV of the high resolution flow-compensated data. The background gradient maps were generated using the predicted field, calculated from the susceptibility reconstruction of the air-tissue and air-bones interfaces. Based on Eq. 4.13, the flow-induced changes in phase were simulated from these background gradient maps, assuming  $v = 60 \text{cm/s}$  for middle cerebral arteries (MCAs) (13–15). The directional vector of the blood velocity was calculated by manually measuring the angles in different sections of the MCAs.

In order to suppress this confounding arterial phase, a binary mask segmenting the arteries was created by setting a threshold to the magnitude images at the shorter TE. To generate better susceptibility maps, the phase inside the arteries was set to zero using the arterial mask after the background field was removed using sophisticated harmonic artifact reduction for phase data (SHARP) (16). Next, susceptibility maps were generated using the geometry constrained susceptibility mapping (iterative SWIM) algorithm (17).

## 4.4 RESULTS

### 4.4.1 Numerical Simulations of the background gradients ( $G'$ )

The field perturbations were simulated using the 3D numerical model, as shown in *Chapter 3, Figure 3.2*. **Figure 4.2** demonstrates the background gradient components calculated from the field maps (as described in Eq. 4.3). The background gradient is much higher near the air-tissue interfaces, where some of the major blood vessels are situated such as the MCAs. The background gradient peaked at 1.5mT/m, measured at a distance of 1.5mm from the air-tissue interface. The values inside the brain, 4mm away from the ethmoid sinus, the background gradient was measured as high as 0.7mT/m (**Figure 4.2j** to **4.2l**). The predicted phase induced by flow in presence of the background gradients are shown in **Figure 4.3**.

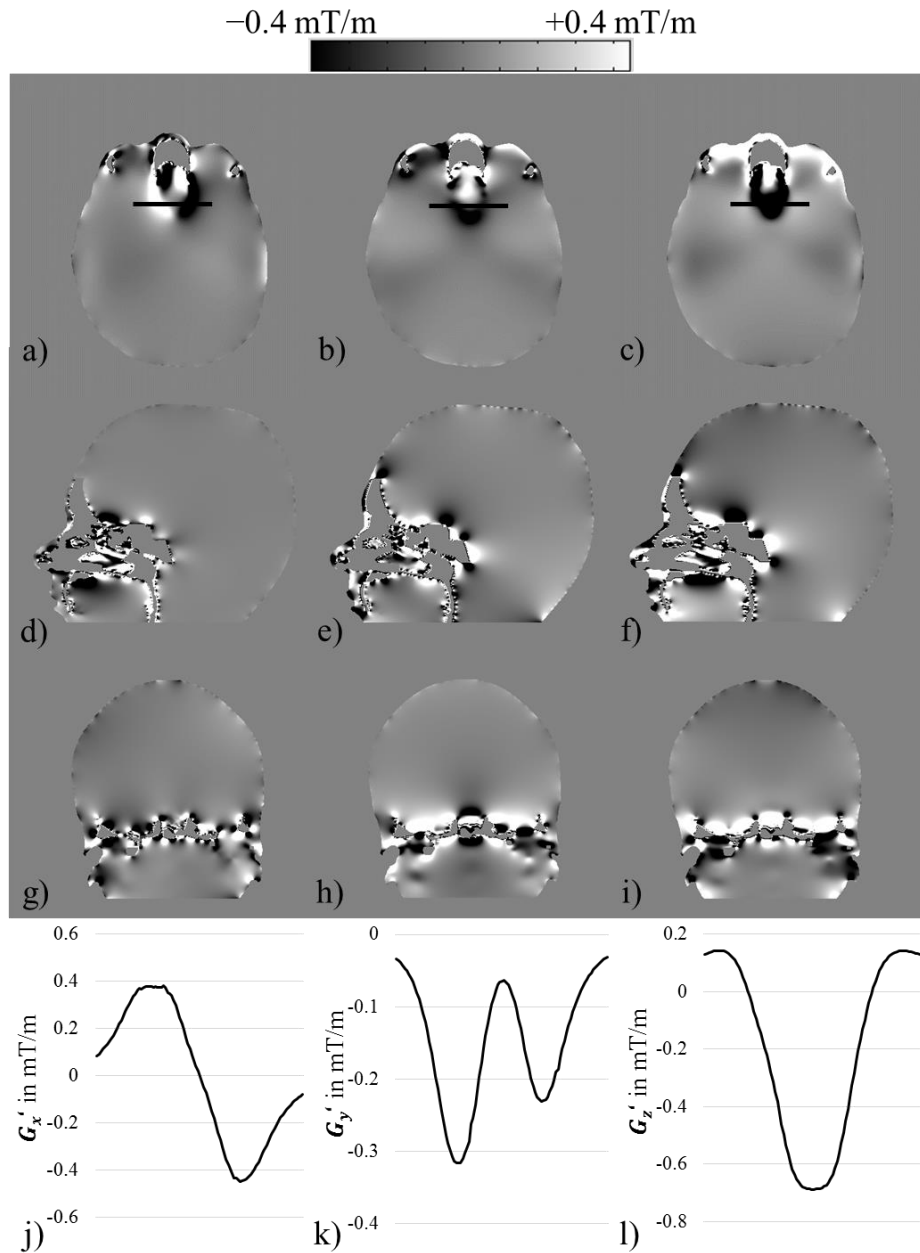


**Figure 4.2.** Calculated background gradient deviations along three dimensions: (a, d and g) along x-direction,  $G'_x$ ; (b, e and h) along y-direction,  $G'_y$ ; and (c, f and i) along z-direction,  $G'_z$ ; shown in transverse, sagittal and coronal planes. The profiles in j), k) and l) were measured along the black lines shown in a), b) and c), respectively.

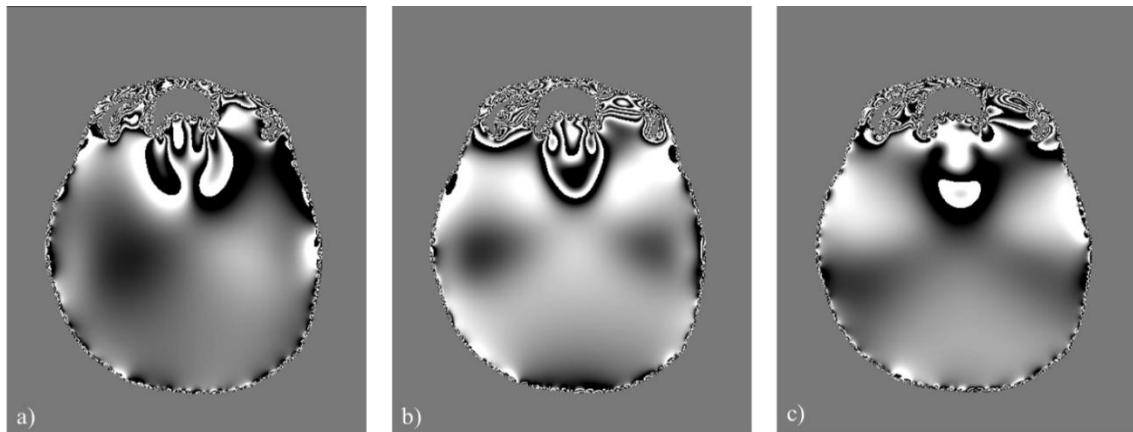


**Figure 4.3.** Phase accumulation due to flow in presence of the background gradient ( $G'$ ) in: a) x-direction (left-right), b) y-direction (up-down) and c) in z-direction (perpendicular to the plane of the image); for blood flow velocity of 60cm/s and TE = 20ms.

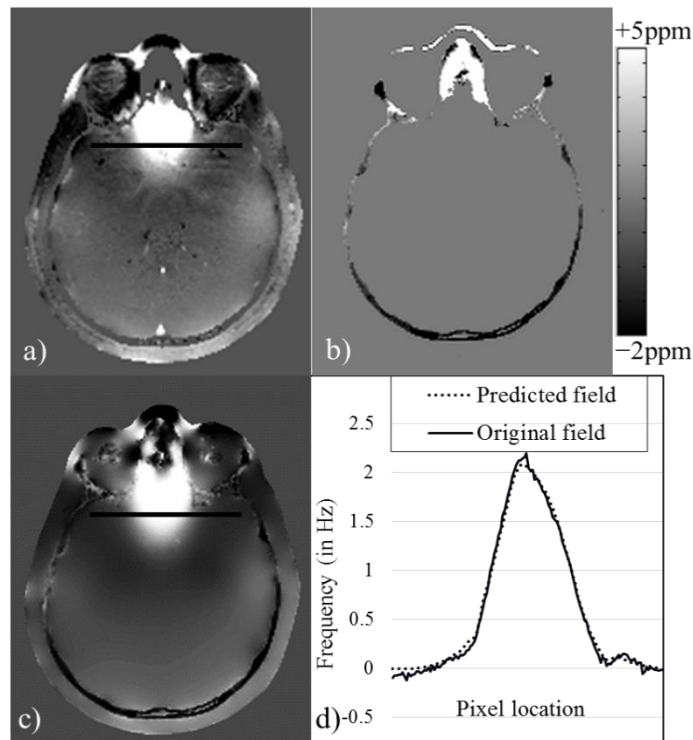


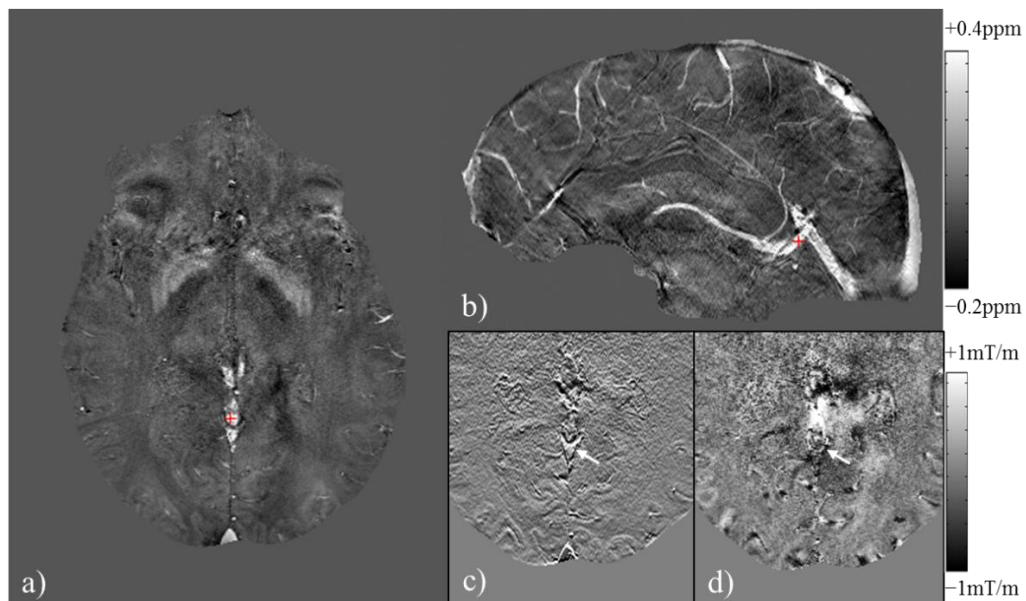
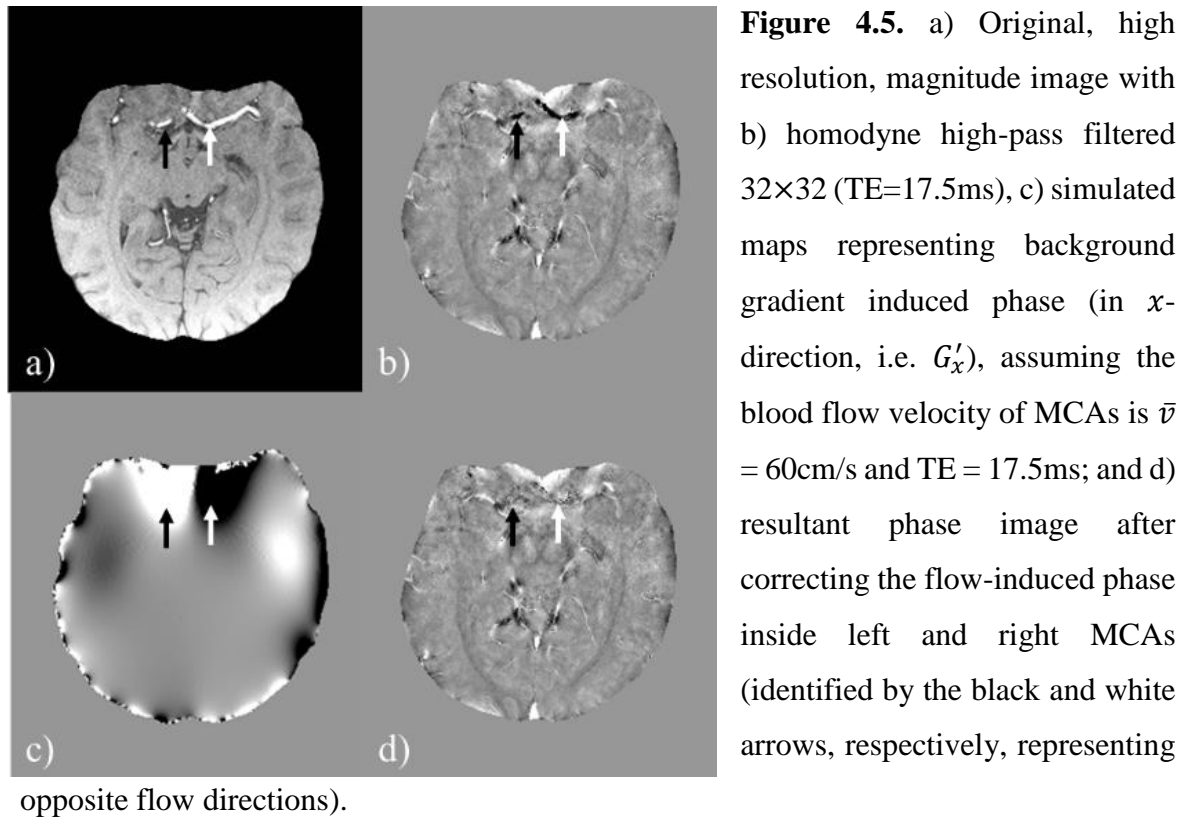
**Figure 4.4.** a) Original, low resolution, unwrapped phase image (TE = 2.5ms), b) sinus maps generated from a, c) the predicted field ( $\Delta B$ ) generated from the sinus shown in b, d) frequency profiles generated along the black line in a and c. Note the agreement between the original phase and predicted field.

#### 4.4.2 In vivo data analysis

The susceptibility distributions of the air or sinuses and bones (**Figure 4.4b**) are generated from the low resolution, non-flow compensated, short TE (TE=2.5ms) phase images (**Figure 4.4a**). The predicted field (**Figure 4.4c**) produced from these sinus maps are in good agreement with the original phase image, as demonstrated in **Figure 4.4d**.

The background gradient maps produced from the predicted field are validated by comparing the flow-induced phase maps generated in the presence of these background gradients with the high resolution data acquired using a fully flow compensated sequence.

The phase image in **Figure 4.5b** attests the aforementioned flow-induced phase in the left and right MCAs (L-MCA and R-MCA). The arteries can be easily distinguished using the magnitude images (**Figure 4.5a**) with relatively high signal due to the time-of-flight (TOF) effect. The arteries were extracted using a simple intensity-based threshold to generate a binary mask. Using this mask, the predicted flow effects were extracted from **Figure 4.5c** to correct the internal phase offset for L-MCA and R-MCA, as demonstrated in **Figure 4.5d**.



The background gradient strength due to the local structures such as veins, which has relatively higher susceptibility than other brain tissues, were analyzed from the flow-compensated data. The  $G'$  gradients inside the vein of Galen were measured in y and z directions:  $G'_y \approx 0.4\text{mT/m}$  and  $G'_z \approx 0.3\text{mT/m}$  (**Figure 4.6**). In addition, arterial phase suppression improves the quality of QSM data, as demonstrated in **Figure 4.7**. While the blood flow induces unwanted phase inside arteries causing false enhancement, it also produces non-local streaking artifacts in the susceptibility maps.

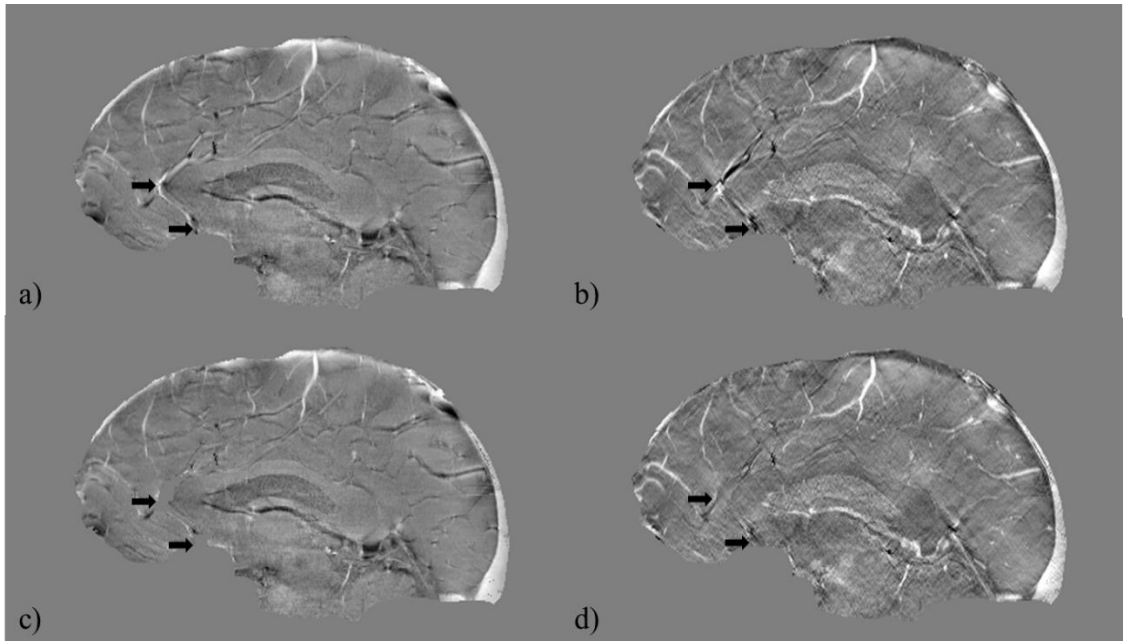


**Figure 4.7.** Phase images and susceptibility maps with and without the suppression of phase from the arteries. a) SHARP processed result using the original phase images, b) susceptibility map produced from a), c) SHARP processed result using the phase images generated after setting the phase inside the arteries to zero, d) susceptibility map produced from c).

## 4.5 DISCUSSION AND CONCLUSIONS

The quality and accuracy of QSM depend on proper flow compensation, as any flow induced phase will cause false enhancement of the vessels phase images and bias and streaking artifacts in the susceptibility maps. In this chapter, the effects of the background field gradient were evaluated quantitatively. This study also demonstrated the potential to predict the flow induced phase from the background field gradient.

As shown in Figures 4.4, the unwanted phase accumulated inside a blood vessel due to blood flow in the presence of background gradients are much stronger near the air-tissue interfaces. For every  $2\pi$  wrap on the predicted flow-induced phase behavior in Figure 4.4 (at  $v = 60\text{cm/s}$ ), we can predict that even for  $1/10^{\text{th}}$  of the velocity, i.e. for  $v = 6\text{cm/s}$ , there will be the corresponding  $18^\circ$  shift in phase inside a vessel in presence of the background gradients. For example, in presence of this small velocity, with the hematocrit of 44% and venous oxygen saturation of 70%, the predicted phase inside the vein parallel to the main field can be  $0.1\pi$  at an echo time of 17.5ms at 3T. On the other hand, the predicted phase due to the susceptibility of venous blood is around  $0.3\pi$  (4,18). Therefore, even with this small speed, there is an approximately 30% error in the phase inside the vein and therefore a 30% error in the estimated susceptibility, if solely the phase inside the vein was used for susceptibility quantification. However, for veins in the central part of the brain (as shown in **Figure 4.6**) it is not expected that the  $G'$ -velocity phase will have a significant impact on the phase measurement or susceptibility quantification of the vein, because of the relatively small background field gradient and slow flow.

The geometric configurations of water and air compartments are the major factors generating the global susceptibility-induced field distortion in the human head. Therefore, for our computer simulations, only the susceptibility differences of water and air were included. The calculated background gradients are simulated with the assumption of a homogeneous main magnetic field. These background gradients can also be determined by various background field removal algorithms (16,19). However, this approach will introduce another source of errors in the phase of the veins, especially in regions close to the edge of the brain, even though the actual background field gradient is small (20).

In practice, the field distortions due to the geometrical effect may be partially compensated by proper shimming of the static magnetic field. However, removing static magnetic field variations due to the air/tissue interfaces would be hard to accomplish with the current shimming methods. The background gradient measured from the high resolution 3D numerical model was as high as 0.7mT/m inside the brain, 4mm away from the ethmoid sinus. According to Eq. 4.9, for a high resolution data with  $(0.5\text{mm})^3$  resolution,  $\text{BW}/\text{pixel} = 400\text{Hz}/\text{pxl}$ ,  $\text{TE} = 17.5\text{ms}$ ,  $N_x = 512$  and  $G'_x = 0.7\text{mT/m}$  acquired with a symmetric echo readout, the effective echo can occur at a shift of  $n_{\text{shift}} \approx 158$  sample points from center of the sampling window. This leads to a uniform phase dispersion of  $-0.62\pi$  across a voxel and a signal loss of 15% (4).

There are a few limitations in this study. Due to the nonlinear nature of blood flow, remnant phase maybe present in regions where acceleration can no longer be neglected. However, for an accurate estimate of the acceleration induced phase requires knowledge of the flow pattern and the geometry of the arteries. Furthermore, the flow in the vessels is not

uniform flow, and any spatial variation of the velocity may cause extra signal decay (4). The extent of which needs to be studied further. The predictions were made using mean velocities throughout the cardiac cycle for the MCAs. The upper and lower limits of both the  $G'$ -velocity phase and the acceleration phase are dependent on the systolic and diastolic velocities. Any misregistration or motion may also lead to additional errors in estimating both the  $G'$ -velocity phase and the acceleration phase. Finally, any imperfect shimming of the main magnetic field will cause an extra gradient and further exacerbation of the  $G'$  induced phase effect.

Lastly, we have shown that it is viable to suppress the confounding arterial phase, by creating a binary mask of the arteries using the short TE magnitude images. The extraction of the arteries using a simple thresholding may not be perfect, particularly in the regions near the edges of the arteries. However, considering a laminar flow pattern, the flow near the edges of the arteries is expected to be slow and, therefore, will not lead to large phase shifts. Thus, missing the edges of the arteries in the binary mask should not seriously affect the suppression of the confounding phase of the arteries.

In conclusion, the numerical model and the sinus maps (from the *in vivo* data) were used to validate that the quality of flow compensation is related to the presence of background field gradients. Removing the acceleration and  $G'$  motion induced phase from the arteries can improve the quality of the QSM results.

## References

1. Haacke EM, Tang J, Neelavalli J, Cheng YCN. Susceptibility mapping as a means to visualize veins and quantify oxygen saturation. *J Magn Reson Imaging JMRI*. 2010 Sep;32(3):663–76.
2. Wharton S, Schäfer A, Bowtell R. Susceptibility mapping in the human brain using threshold-based k-space division. *Magn Reson Med*. 2010 May 1;63(5):1292–304.
3. De Rochefort L, Liu T, Kressler B, Liu J, Spincemaille P, Lebon V, et al. Quantitative susceptibility map reconstruction from MR phase data using bayesian regularization: validation and application to brain imaging. *Magn Reson Med*. 2010 Jan;63(1):194–206.
4. Haacke EM. *Magnetic resonance imaging: physical principles and sequence design*. New York, NY [u.a.: Wiley-Liss; 1999.
5. Bernstein MA, King KF, Zhou XJ. *Handbook of MRI Pulse Sequences*. Elsevier; 2004. 1041 p.
6. Buch S, Liu S, Ye Y, Cheng Y-CN, Neelavalli J, Haacke EM. Susceptibility mapping of air, bone, and calcium in the head. *Magn Reson Med*. 2014 Jul 7;
7. Haynes WM. *CRC Handbook of Chemistry and Physics, 94th Edition*. 94 edition. CRC Press; 2013. 2668 p.
8. Neelavalli J, Cheng Y-CN, Jiang J, Haacke EM. Removing background phase variations in susceptibility-weighted imaging using a fast, forward-field calculation. *J Magn Reson Imaging JMRI*. 2009 Apr;29(4):937–48.
9. Marques J p., Bowtell R. Application of a Fourier-based method for rapid calculation of field inhomogeneity due to spatial variation of magnetic susceptibility. *Concepts Magn Reson Part B Magn Reson Eng*. 2005 Apr 1;25B(1):65–78.

10. Koch KM, Papademetris X, Rothman DL, de Graaf RA. Rapid calculations of susceptibility-induced magnetostatic field perturbations for in vivo magnetic resonance. *Phys Med Biol.* 2006 Dec 21;51(24):6381–402.
11. Cheng Y-CN, Neelavalli J, Haacke EM. Limitations of calculating field distributions and magnetic susceptibilities in MRI using a Fourier based method. *Phys Med Biol.* 2009 Mar 7;54(5):1169–89.
12. Feng W, Neelavalli J, Haacke EM. Catalytic multiecho phase unwrapping scheme (CAMPUS) in multiecho gradient echo imaging: removing phase wraps on a voxel-by-voxel basis. *Magn Reson Med.* 2013 Jul;70(1):117–26.
13. Blaber AP, Bondar RL, Stein F, Dunphy PT, Moradshahi P, Kassam MS, et al. Complexity of middle cerebral artery blood flow velocity: effects of tilt and autonomic failure. *Am J Physiol.* 1997 Nov;273(5 Pt 2):H2209–16.
14. Kofke WA, Brauer P, Policare R, Penthany S, Barker D, Horton J. Middle cerebral artery blood flow velocity and stable xenon-enhanced computed tomographic blood flow during balloon test occlusion of the internal carotid artery. *Stroke J Cereb Circ.* 1995 Sep;26(9):1603–6.
15. Valdueza JM, Balzer JO, Villringer A, Vogl TJ, Kutter R, Einhüpl KM. Changes in blood flow velocity and diameter of the middle cerebral artery during hyperventilation: assessment with MR and transcranial Doppler sonography. *AJNR Am J Neuroradiol.* 1997 Dec;18(10):1929–34.
16. Schweser F, Deistung A, Lehr BW, Reichenbach JR. Quantitative imaging of intrinsic magnetic tissue properties using MRI signal phase: an approach to in vivo brain iron metabolism? *NeuroImage.* 2011 Feb 14;54(4):2789–807.

17. Tang J, Liu S, Neelavalli J, Cheng YCN, Buch S, Haacke EM. Improving susceptibility mapping using a threshold-based K-space/image domain iterative reconstruction approach. *Magn Reson Med*. 2013 May;69(5):1396–407.
18. Haacke EM, Reichenbach JR. *Susceptibility Weighted Imaging in MRI: Basic Concepts and Clinical Applications*. John Wiley & Sons; 2014. 916 p.
19. Liu T, Khalidov I, de Rochefort L, Spincemaille P, Liu J, Tsiouris AJ, et al. A novel background field removal method for MRI using projection onto dipole fields (PDF). *NMR Biomed*. 2011 Nov;24(9):1129–36.
20. Haacke EM, Liu S, Buch S, Zheng W, Wu D, Ye Y. Quantitative susceptibility mapping: current status and future directions. *Magn Reson Imaging*. 2015 Jan;33(1):1–25.

# **Chapter 5: Measuring the Changes in Cerebral Oxygen Extraction Fraction**

## **5.1 INTRODUCTION**

Oxygen extraction fraction (OEF) represents the amount of oxygen consumed from the blood by the surrounding tissue during its passage through the capillary network. For a healthy subject, the cerebral metabolic rate of oxygen ( $CMRO_2$ ) is maintained by regulating the OEF along with the cerebral blood flow. The complex physiology of blood flow and oxygen saturation levels in the blood modulates the MRI signal in the veins (1–4). Neural activity creates local changes in cerebral hemodynamics, which in turn can be detected using functional magnetic resonance imaging (fMRI) techniques through the blood-oxygen-level-dependent (BOLD) response (1,2). The BOLD effect is a function of cerebral blood flow (CBF), cerebral blood volume (CBV), and oxygen consumed by the brain tissues (5,6), and relative changes in this hemodynamic response are used as a surrogate to detect neuronal activity.

Despite its broad spread utility in the neurosciences, the BOLD fMRI technique suffers from limited temporal and spatial resolution. Furthermore, the specificity of the technique is difficult to assess because measurements may be contaminated by larger vessels representing an integrated effect from a larger territory than desired (7,8).

Accepted values for venous oxygen saturation level ( $Y_v$ ) and  $CMRO_2$  in the literature are reported by positron emission tomography (PET) studies (9,10) and have identified these parameters as critical markers in disease states such as stroke and tumor (11,12). However, PET imaging is a relatively low spatial-resolution technique and involves injection of a radioactive labeled isotope, which requires equipment that is not widely available and has risk for the patient. MRI-based methods have been proposed to measure oxygenation in the brain, including the combination of fMRI BOLD and CBF measurements for calibrated estimates of  $CMRO_2$  changes (13,14). These calibrated fMRI techniques, however, only measure relative changes in metabolism with comparatively low resolution (15). A recent alternate approach based on  $T_2$  relaxation in MRI,  $T_2$ -relaxation-under-spin-tagging (TRUST), allows quantification of  $Y_v$  and  $CMRO_2$ , but only offers measurements from a single slice placed judiciously in the brain (16).

Our goal is to introduce a method that provides high-resolution, quantitative measurements of the changes in OEF in the presence of physiological challenges, particularly, the administration of vasodynamic agents such as caffeine and acetazolamide (brand name Diamox). Using the susceptibility maps that are generated from gradient echo phase data, the susceptibility changes and the corresponding oxygen saturation level for a given vein can be quantified (3,17,18). The measurements of OEF changes are based on

the variation of susceptibility differences between cerebral veins and the surrounding brain parenchyma, instigated by vasodynamic agents. The measured susceptibility differences are related to oxygen saturation because the intravascular concentration of deoxyhemoglobin, a paramagnetic species, changes with the venous oxygenation level (17,19). Using a proposed approach to improve the accuracy of susceptibility mapping, we have the capability and potential to image the hemodynamics of the brain, monitor the damage, and show that changes induced by vasodynamic agents such as caffeine or acetazolamide, can be quantified.

## 5.2 THEORY

### 5.2.1 Relation between measured susceptibility and local OEF

Susceptibility maps measure the shift in susceptibility between two tissues (such as a vein and the surrounding tissue), hence, providing an endogenous oxygenation-dependent contrast (3). Hemoglobin in red blood cells is the primary carrier of oxygen in the body, and its reduced form is deoxyhemoglobin, which is found in venous blood. Decreased oxygenation corresponds to an increased concentration of deoxyhemoglobin, which is paramagnetic, due to the higher spin state of heme iron. This is reflected in the increased susceptibility of venous blood with respect to the surrounding brain parenchyma.

From the measured susceptibility shift ( $\Delta\chi$ ), OEF for each vessel can be quantified (5):

$$\Delta\chi = \mathbf{Hct} \cdot \mathbf{OEF} \cdot \Delta\chi_{\text{do}}, \text{ where } \mathbf{OEF} = (Y_a - Y_v) \quad [5.1]$$

where,  $\Delta\chi_{do} = 0.27$  ppm (in cgs) is the susceptibility difference between fully deoxygenated and fully oxygenated blood, and implicitly we assume that the tissue has the same susceptibility as fully oxygenated blood. Hematocrit (Hct) is the percent fraction of blood volume that consists of red blood cells. By assuming the arterial oxygen saturation ( $Y_a = 95 - 98\%$ ),  $Y_v$  can be measured.

## 5.3 METHODS

### 5.3.1 Forced value iterative SWIM

The iterative method has proven to be effective in reducing the external streaking artifacts and improving the susceptibility value for the structure-of-interest (*See Chapter 2, section 2.7.2*) (18). However, the streaking inside the object is still carried forward in the iterations. One way to reduce the artifacts inside a major vein like the superior sagittal sinus would be to smooth these values or to set them to uniform value before applying iterative algorithm. The idea is to remove the effect of the streaking artifacts inside the vessel by giving it a uniform distribution to start with. The critical issue here is whether this will still allow the process to converge to the correct susceptibility value despite setting it to an initial empirical value.

The concept of using a uniform initial value was tested using the 3D brain model consisting of basal ganglia and mid brain structures, grey and white matter with veins. The susceptibility maps of the brain model were generated using the iterative SWIM algorithm with and without setting constant initial susceptibility values of 0.30ppm, 0.45ppm,

0.70ppm and 1.0ppm to the veins. The veins were assigned a uniform value only for the first iteration; and the subsequent iterations were carried out conventionally.

### 5.3.2 Instigation of physiological challenges

We compared the susceptibility maps before and after ingestion of 200 mg NoDoz pill for caffeine (Novartis Consumer Health Inc, Parsippany, NJ, USA) and 1000mg Diamox IV or Acetazolamide (Sagent Pharmaceuticals, Schaumburg, IL, USA) to examine the changes in oxygenation levels in the veins. Caffeine will affect both blood flow and neural activity. Vasoconstriction due to caffeine reduces the blood flow and increases the OEF in order to retain the  $CMRO_2$  levels (20–26). Similarly, Acetazolamide is known to be a potent vasodilating agent, and, hence, will cause an increase in cerebral blood flow (27–30). This effect will provide an opposite physiological state to the caffeine challenge, causing a decrease in OEF. The caffeine and Diamox doses were administered on two separate days.

### 5.3.3 Selection of echo time (TE) for phase-susceptibility measurements

Susceptibility of the structure-of-interest is one of the major factors in selecting the echo time. There is a trade-off involved between higher phase SNR at longer TEs versus less  $T_2^*$  signal decay and less phase wrapping at shorter TEs (See *Chapter 2*, section 2.4.1). As a compromise, we used an echo time of  $TE = 15ms$  for the 3T acquisition to avoid phase wrapping between the vessel and background tissue, while maintaining a maximum expected phase difference of between 2 and 3 radians for the physiological range of  $Y_v$  (50 – 75%) (31).

### 5.3.4 Data acquisition

Initially, susceptibility weighted imaging (SWI) data were acquired, using the MRAV sequence, once before the intake of acetazolamide or caffeine and then every 15 minutes for four time points (32,33). Acquiring data at different time points was essential to study the variation in susceptibility values based on the functional dynamics caused by the drug and to select the time point that provided the peak change.

Five healthy volunteers were then scanned once before and once after (at the selected time point) the administration of caffeine and Diamox. All data were acquired using an rf-spoiled, fully flow compensated 3D sequence with the imaging parameters: TE = 15ms, FA = 13°, TR = 24ms, BW = 119Hz/pixel, voxel size = 0.5×0.5×0.5mm<sup>3</sup>, and matrix size = 448×336.

### 5.3.5 Image processing

The original phase images were unwrapped using Laplacian method (34,35), followed by background field removal using sophisticated harmonic artifact reduction for phase (SHARP) method (36) to generate the processed phase map at TE=15ms. Signal-to-noise ratio (SNR) in the magnitude images were estimated as the ratio of mean over standard deviation of values measured within a homogeneous region of white matter. By using the arterial binary mask generated from the magnitude data, the flow artifacts inside the arteries were suppressed. The proposed method of forced value iterative SWIM (initial value of 0.45ppm for veins) was used to produce the local susceptibility distribution maps.

The susceptibility distribution was measured inside the major cerebral veins: right and left internal cerebral veins, right and left thalamo-striate veins, right and left septal veins, vein of Galen and straight sinus. The change in susceptibility value between the normal brain state ( $\Delta\chi_{\text{Normal}}$ ) and post-drug or active ( $\Delta\chi_{\text{Active}}$ ) state were used to quantitatively study the effect on the tissue oxygen consumption variation ( $\Delta\text{OEF}$ ), based on Eq. 1:

$$\frac{\Delta\text{OEF}}{\text{OEF}_{\text{Normal}}} = \frac{\Delta\chi_{\text{Active}} - \Delta\chi_{\text{Normal}}}{\Delta\chi_{\text{Normal}}} \quad [2]$$

### 5.3.6 Statistical Analysis

Paired-sample t-tests were performed to assess the differences in QSM before and after the caffeine or Diamox challenge across the subjects. P values of less than 0.05 were considered to indicate statistical significance. All data were expressed as mean  $\pm$  standard deviation.

## 5.4 RESULTS

### 5.4.1 Numerical simulations

**Figure 5.1** demonstrates the reduction in internal streaking artifacts for the straight sinus as compared to the conventional iterative SWIM method. The two rows of images with different contrasts are used to be able to visualize the veins and other structures of the 3D brain model in the first row and to visualize the internal streaking for veins in the second row. The mean and standard deviation of the susceptibility distribution inside the straight sinus was measured as  $\Delta\chi = 0.41 \pm 0.04$  ppm for the conventional method. Whereas, for the forced value iterative SWIM method, the measured susceptibility distribution were

measured as  $\Delta\chi = 0.45 \pm 0.01$  ppm and  $\Delta\chi = 0.46 \pm 0.02$  ppm for assuming the initial value as 0.45ppm and 0.70ppm inside the veins, respectively.

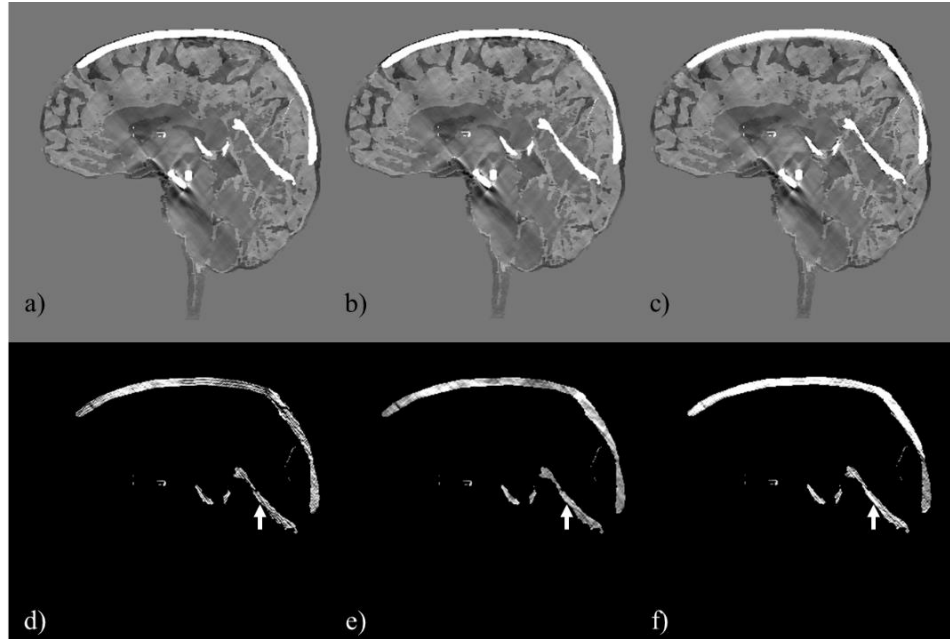


**Figure 5.1.** Simulated susceptibility maps produced from a 3D numerical model using a) conventional iterative algorithm, b) the proposed method by assigning 450ppb to veins and c) by assigning 700ppb to veins. Images d, e and f are contrast modified versions of a, b, and c to visualize the extent of internal streaking artifacts.

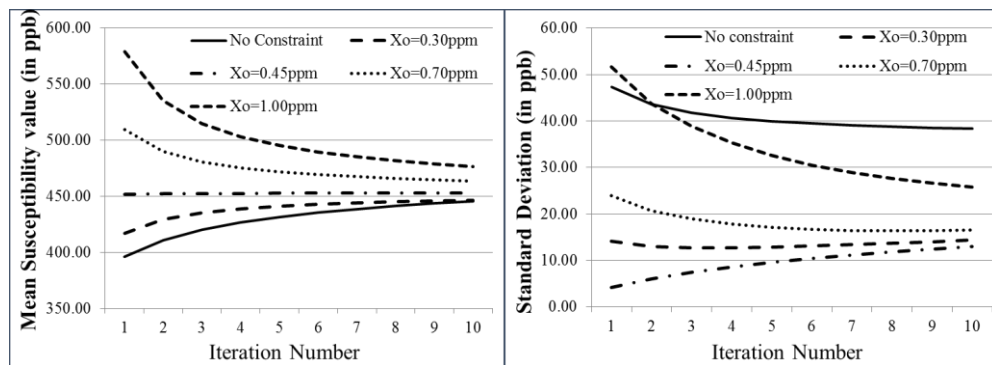


**Figure 5.2.** Mean (a) and standard deviation (b) of the susceptibility measured inside the superior sagittal sinus at each iteration of the iterative SWIM algorithm. Different initial values ( $\chi_0$ ) were set to the veins. Independent of the choice of starting point, the values tend to converge close to the expected susceptibility of 0.45 ppm. The use of proper initial value reduces the streaking artifacts inside the veins.

**Figure 5.2** demonstrates that, independent of the choice of the initial value, the mean susceptibility value inside the straight sinus stays at or approaches the correct susceptibility value of 0.45 ppm. This is expected as only a small cone of k-space elements is modified (regularization threshold =0.1), whereas the other remaining k-space components outside the cone of singularity drive the value back to the true susceptibility.

The iterative results, when the initial value of 0.45 ppm was used, were the best in terms of the highest accuracy in the mean susceptibility value (0.453 ppm) and the lowest standard deviation (0.013 ppm). With no constraint on the values inside the straight sinus, the final measured susceptibility value was 0.446 ppm inside the straight sinus, but the standard deviation increased to 0.038 ppm due to the streaking artifacts.

#### 5.4.2 *In vivo* data analysis

SNR of the gradient echo magnitude images and the susceptibility maps were measured as  $\text{SNR}_{\text{mag}} = 17.8 \pm 2.1$ . Similar to the numerical simulations, the results from the *in vivo* data (**Figure 5.3**) demonstrate the improvement in the susceptibility reconstruction of the veins. The susceptibility value inside the straight sinus, without initial constraints, were measured to be  $0.41 \pm 0.14\text{ppm}$ , respectively. On the other hand, when the starting value of 0.45ppm initial value was used, the susceptibility value inside the straight sinus increased to  $0.45 \pm 0.06\text{ppm}$ . Likewise, the susceptibility of a small peripheral vein improved from  $0.32 \pm 0.09\text{ppm}$  to  $0.36 \pm 0.04\text{ppm}$  (the vein is identified by white arrows in **Figure 5.3c** and **5.3d**)).

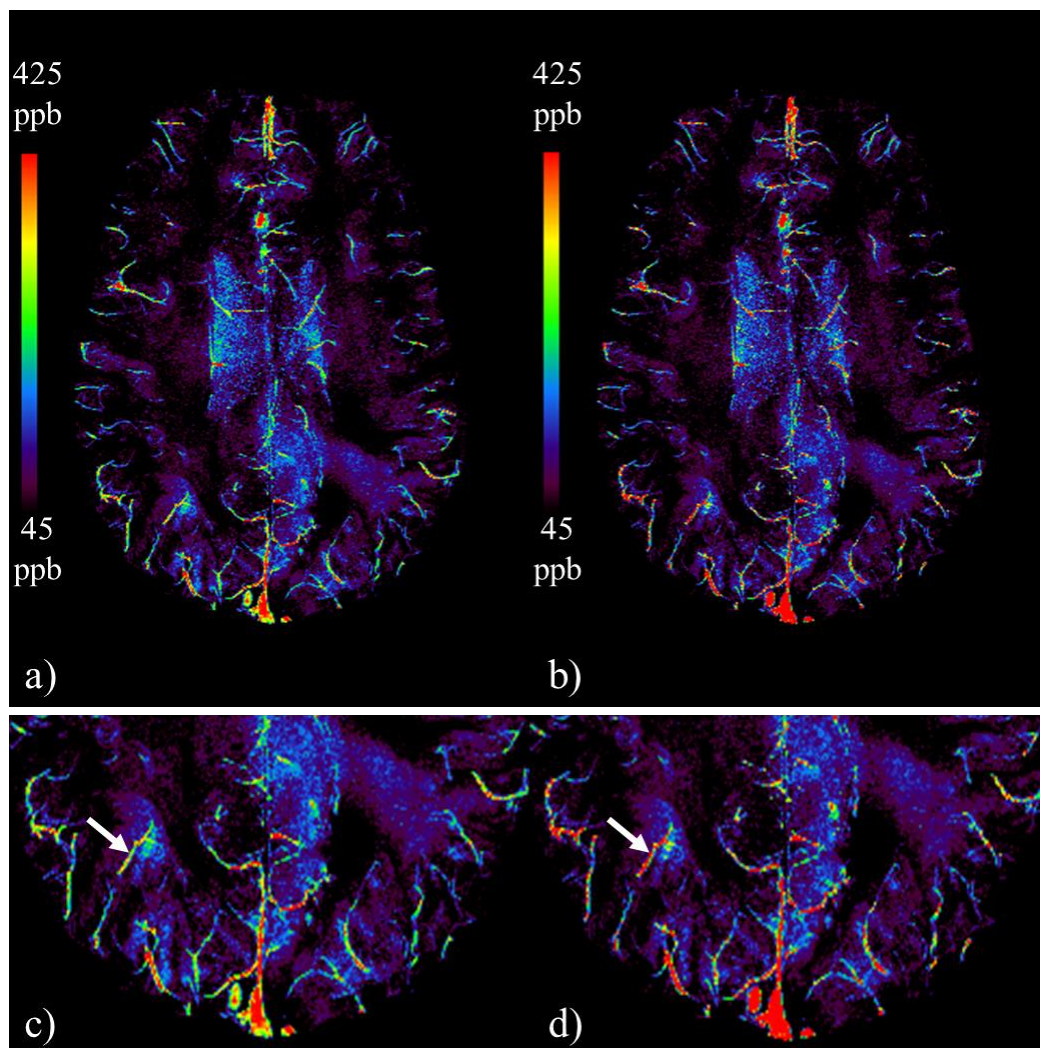


**Figure 5.3.** a) Susceptibility maps generated using the conventional iterative technique, and b) susceptibility maps generated using the forced value iterative method. Note the improvement in the susceptibility distribution, inside the veins of different sizes, in d) with respect to the conventional iterative SWIM results in c).

There is a clear increase in the susceptibility of venous blood, as can be seen from the brighter venous vessels in **Figure 5.4a)** to **Figure 5.4e)**, indicating an increase in deoxyhemoglobin levels post caffeine administration. Similarly, **Figure 5.4f)** to **Figure 5.4j)** indicate a decrease in deoxyhemoglobin levels post Diamox administration.

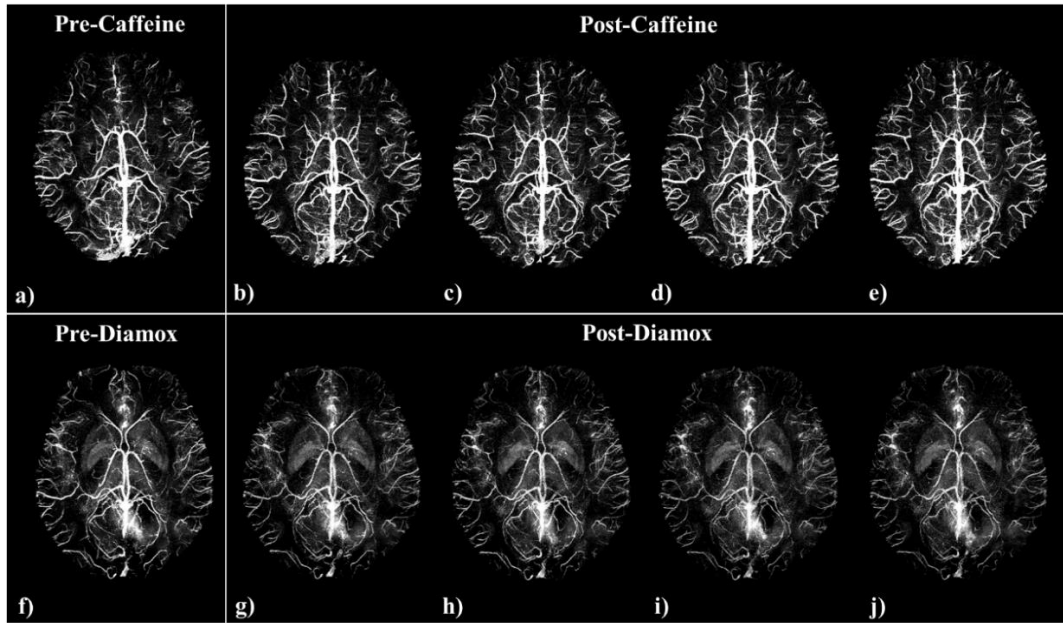


**Figure 5.4.** Evaluation of dynamic changes in venous susceptibility distribution due to the administration of caffeine and Diamox. Phase data is acquired for four time points after the drug ingestion, at an interval of 15 minutes. a) and f) Susceptibility maps for the data acquired before caffeine and Diamox intake, respectively, b-e) susceptibility maps for the data at four times points after caffeine intake, g-j) susceptibility maps the data at four times points after Diamox intake.

The measured susceptibility values inside internal cerebral veins, for the caffeine test are as follows: Pre:  $0.47 \pm 0.06\text{ppm}$ , Post: Time 1:  $0.53 \pm 0.07\text{ppm}$ , Time 2:  $0.58 \pm 0.10\text{ppm}$ , Time 3:  $0.61 \pm 0.08\text{ppm}$ , Time 4:  $0.61 \pm 0.09\text{ppm}$ ; and for the Diamox test are as follows: Pre:  $0.46 \pm 0.08\text{ppm}$ , Post: Time 1:  $0.38 \pm 0.09\text{ppm}$ , Time 2:  $0.36 \pm 0.06\text{ppm}$ , Time 3:  $0.36 \pm 0.08\text{ppm}$ , Time 4:  $0.37 \pm 0.07\text{ppm}$ . The susceptibility value reaches the peak after the second time point, and stays consistent for the third and the fourth time points. Hence, we selected the second time point (30minutes after dose administration) to analyse the post-drug intake functional state. The profile plots across the internal cerebral veins,

demonstrating the effects of caffeine/Diamox intake on susceptibility values, are shown in

**Figure 5.5.**

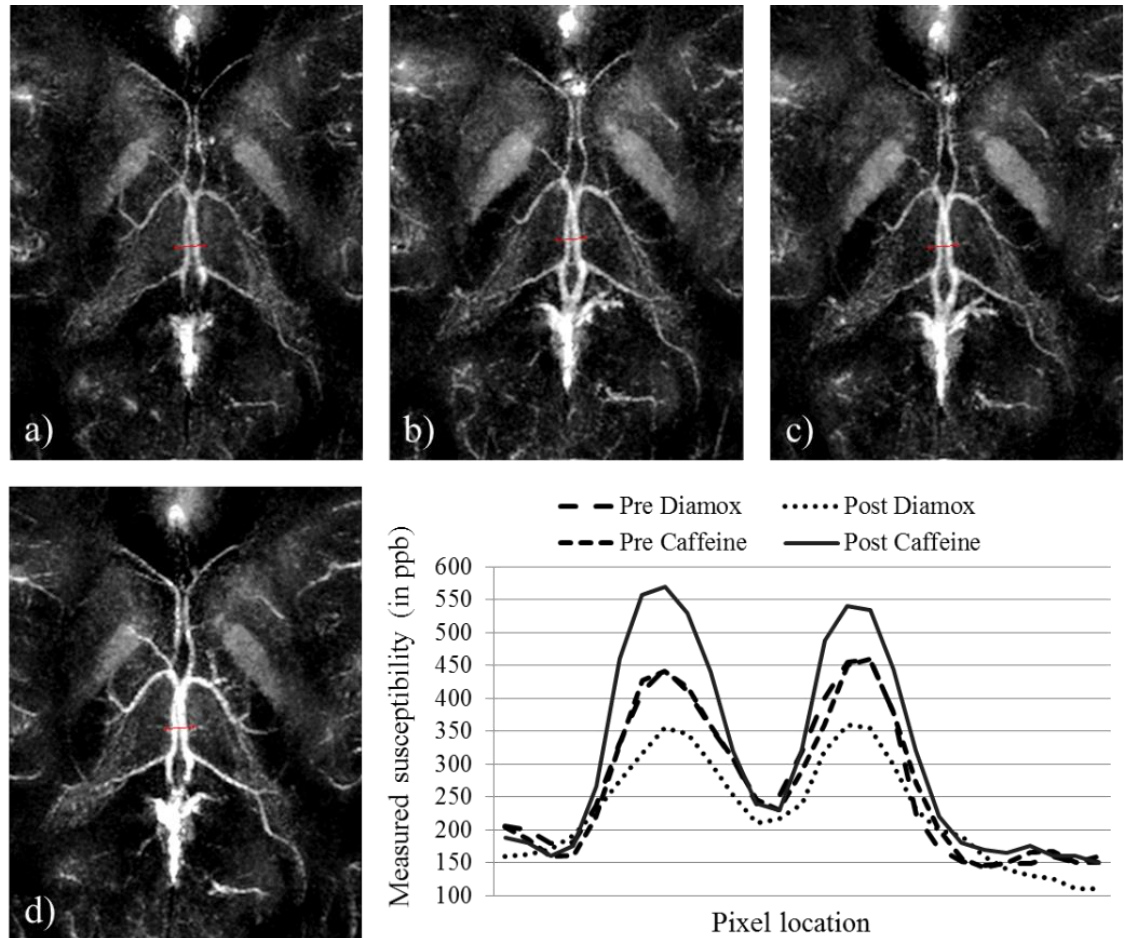


**Figure 5.5.** Susceptibility maps generated from the data acquired: a) post-Diamox administration, b and c) pre-Diamox and pre-caffeine administration, d) post-caffeine administration for healthy volunteers. The profile plot demonstrates the variation in susceptibility values across the internal cerebral veins caused by these altered brain states.

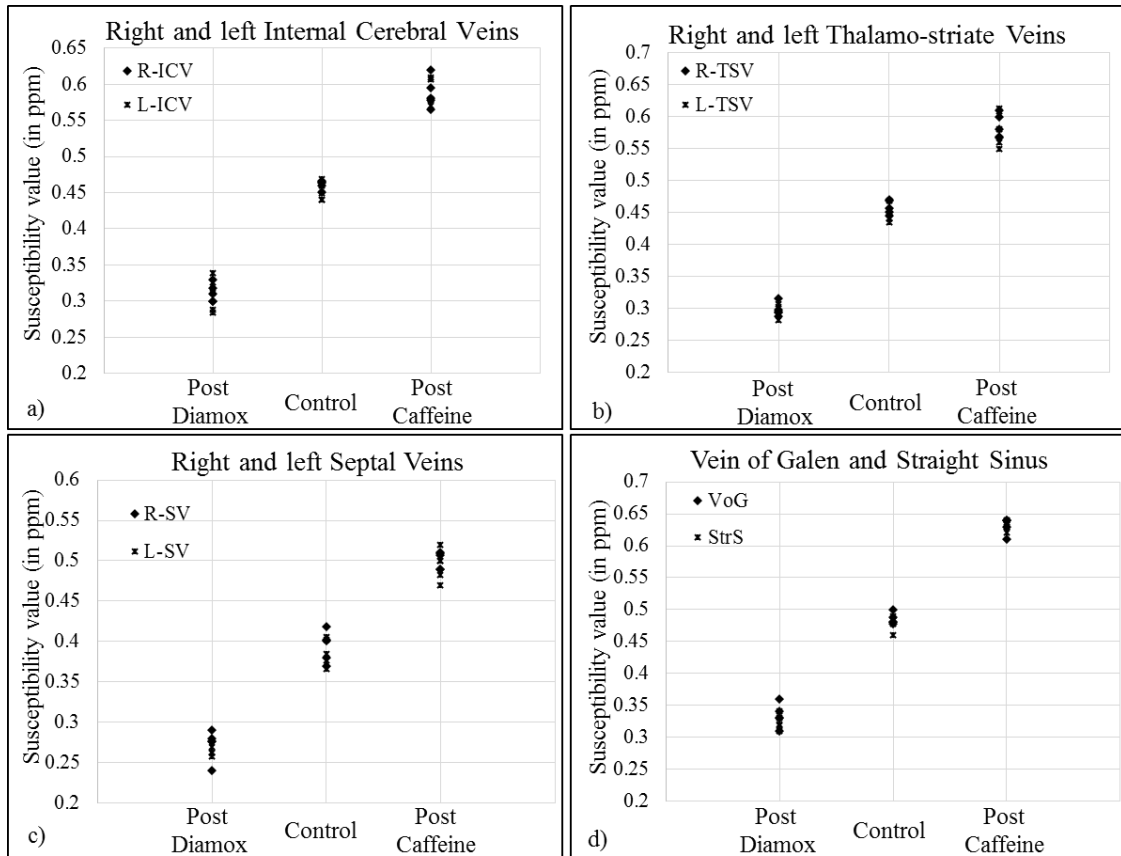


**Figure 5.6.** Susceptibility values measured inside the major cerebral veins across five healthy volunteers. The phase data was acquired before and after the administration of Diamox and Caffeine with  $TE = 15\text{ms}$  and voxel resolution =  $(0.5\text{mm})^3$ . Each drug test was performed on separate days. The susceptibility values generated from the data acquired pre-administration of these drugs were averaged. R-ICV, L-ICV: right and left internal cerebral veins; R-TSV, L-TSV: right and left thalamo-striate veins; R-SV, L-SV: right and left septal veins; VoG: Vein of Galen; StrS: Straight sinus.

As shown in **Figure 5.6**, compared to the pre-caffeine values, there is a statistically significant increase in susceptibility inside the internal cerebral veins ( $\Delta\chi_{\text{Caffeine-Normal}} = +0.15 \pm 0.04 \text{ ppm}$ ;  $p < 0.01$ ) at 30-min post-caffeine. Similarly, the post-Diamox results showed a statistically significant decrease in the measured susceptibility inside the internal cerebral veins ( $\Delta\chi_{\text{Diamox-Normal}} = -0.14 \pm 0.05 \text{ ppm}$ ;  $p < 0.01$ ). Assuming  $\Delta\chi_{do} = 0.27 \text{ ppm}$

(cgs) and Hematocrit = 44% in Eq. 1, the venous oxygen saturation level (inside the internal cerebral veins (ICVs)) for normal physiological conditions, post-caffeine and post-Diamox for the first volunteer were calculated as (mean  $\pm$  standard deviation):  $Y_{\text{Normal}} = 69.1 \pm 3.3$  %,  $Y_{\text{Caffeine}} = 60.5 \pm 2.8$  % and  $Y_{\text{Diamox}} = 79.1 \pm 4.0$ %. The inter-subject error in mean values of venous oxygen saturation over the five subjects were measured inside the ICVs as:  $\sigma_{Y_{\text{Normal}}} = \pm 0.7\%$ ,  $\sigma_{Y_{\text{Caffeine}}} = \pm 1.2\%$ ,  $\sigma_{Y_{\text{Diamox}}} = \pm 1.2\%$ .

For the caffeine challenge, the percentage change in OEF for pre and post caffeine results was calculated as (mean  $\pm$  inter-subject variability)  $+29.1 \pm 1.7\%$ ; and for the Diamox challenge, the percentage change in OEF for pre and post Diamox results was calculated as  $-32.3 \pm 1.5$  % for the right internal cerebral veins (see **Table 5.1** for the change in OEF measurements).

Vein	$\frac{\Delta\text{OEF}}{\text{OEF}_{\text{Pre-Diamox}}}\%$	$\frac{\Delta\text{OEF}}{\text{OEF}_{\text{Pre-Caffeine}}}\%$	Vein	$\frac{\Delta\text{OEF}}{\text{OEF}_{\text{Pre-Diamox}}}\%$	$\frac{\Delta\text{OEF}}{\text{OEF}_{\text{Pre-Caffeine}}}\%$
<b>R-ICV</b>	$-32.6 \pm 2.1\%$	$+27.0 \pm 3.8\%$	<b>L-ICV</b>	$-31.7 \pm 5.1\%$	$+29.9 \pm 3.2\%$
<b>R-TSV</b>	$-34.9 \pm 3.1\%$	$+27.8 \pm 6.4\%$	<b>L-TSV</b>	$-34.1 \pm 3.1\%$	$+30.4 \pm 5.1\%$
<b>R-SV</b>	$-30.7 \pm 6.1\%$	$+27.4 \pm 7.4\%$	<b>L-SV</b>	$-31.1 \pm 3.6\%$	$+28.1 \pm 8.1\%$
<b>VoG</b>	$-31.1 \pm 4.7\%$	$+30.3 \pm 2.5\%$	<b>StrS</b>	$-32.0 \pm 2.4\%$	$+32.0 \pm 2.4\%$

**Table 5.1.** Mean  $\pm$  standard deviation of the percentage change in oxygen extraction fraction for cerebral veins of different vessel sizes, across five healthy subjects, measured before and after administration of Diamox and caffeine. R-ICV, L-ICV: right and left internal cerebral veins; R-TSV, L-TSV: right and left thalamo-striate veins; R-SV, L-SV: right and left septal veins; VoG: Vein of Galen; StrS: Straight sinus.

## 5.5 DISCUSSION AND CONCLUSIONS

In this chapter, we have proposed a new MRI method to quantify *in vivo* local OEF changes in the brain and demonstrated the method with imaging studies on human volunteers. These physiological parameters are currently clinically unavailable using non-invasive MRI techniques, and have the potential to provide novel information about brain function and disease. One such example is the presence of asymmetrically prominent cortical veins (APCV), seen in ischemic stroke, which are hypothesized to be related to increased venous deoxyhemoglobin (37). This is likely caused by hypo-perfusion that leads to a compensatory OEF increase to maintain oxygen metabolism before the onset of brain tissue infarction. On the other hand, if there is no visible decrease, this could be because collaterals maintain the oxygenation level in the stroke region (38,39) and improved brain tissue viability (40). These physiological changes can be detected and quantified using susceptibility mapping techniques.

Applying the geometry constrained iterative SWIM method reduces mostly the streaking artifacts outside the structure of interest, found in the original susceptibility map. As compared to the conventional iterative method for susceptibility mapping, applying an initial uniform value inside the veins, for only the first iteration, reduced not only the external streaking artifacts, but also the streaking inside the veins. The plots shown in **Figure 5.2** demonstrate that the method is robust against the errors made in assuming the initial value, as the measured susceptibility value converges towards the actual value. However, the closer the assumed value to the actual value, the faster the convergence.

Hence, it is advantageous to have *a priori* information of the susceptibility value for the structure-of-interest. Consistent with the simulated results, the susceptibility maps reconstructed from the *in vivo* data (**Figure 5.3**) using initial value constraint method showed improvement over conventional iterative SWIM. Moreover, as explained in *Chapter 4*, the flow artifact inside the arteries, such as middle and anterior cerebral arteries, are introduced due to the presence of background gradients and acceleration effects. By suppressing these artifacts using the arterial binary masks, helps in improving the susceptibility maps (See **Figure 4.7**).

In addition to measuring the oxygen saturation at a normal brain state, it is essential to involve special physiological challenges, such as vasodilation or vasoconstriction, to determine brain health and onset of a disease/stroke. Caffeine-related antagonism reduces the ability of adenosine to contribute to functional increases in cerebral blood flow (CBF) (20,24,25,41). Since brain activity remains constant or even increases, the decrease of CBF in the presence of caffeine should, thus, increase the oxygen extraction fraction (OEF) in order to maintain  $CMRO_2$ . The increased OEF leads to the increase of the concentration of deoxyhemoglobin in the blood; therefore, we would expect to see higher susceptibility values in the post caffeine case (39). This is validated in our study when caffeine introduction caused a decrease in the venous oxygen saturation levels from normal ( $Y_{Normal} = 69.1 \pm 3.3 \%$ ) to post-caffeine ( $Y_{Caffeine} = 60.5 \pm 2.8 \%$ ). Similarly, the decrease in venous oxygen saturation in the presence of a vasodilating agent, Diamox ( $Y_{Diamox} = 79.1 \pm 4.0\%$ ), is also within our expectations. Furthermore, these results are in good agreement with a

previous study on caffeine (3,42–44). Results of the Diamox challenge are close to the previously measured value for carbogen intake  $Y_{\text{carbogen}}=80\%$  ( $\Delta\chi_{do}=0.27$  ppm) (42).

Ideally, the measured variation should reflect the exact physiological alterations in the local venous vasculature where oxygen exchange between the cerebral vessels and tissue occurs during neural activation. In reality, the sensitivity is confounded by the partial volume effect due to the limited voxel resolution. There is much room for improvement by introducing techniques of compressed sensing, which will help in saving the acquisition time that could be utilized to increase the spatial resolution, temporal resolution or SNR (45–47).

In order to calculate the venous oxygen saturation levels, several physiological parameters such as arterial oxygenation saturation level ( $Y_a$ ) and total hemoglobin concentration (Hct) are, in general, assumed fixed for all subjects. However, hematocrit values are dependent on the age and sex of the subject with normal levels ranging from 40.7% to 50.3% for males and 36.1% to 44.1% for females (48). Making an assumption within these ranges of Hct, the error propagation may cause a considerable change from the actual value. For this study, the percentage change in OEF values before and after the drug intake were calculated, which is independent of Hct. Monitoring  $CMRO_2$  to see if it remains the same after these challenges will require perfusion measurements as well in the future (49,50).

Field et al. (2003) reported a higher caffeine-induced response, i.e. CBF reduction, in heavy caffeine users (>300 mg/day) (51). Consequently, the susceptibility values of veins

should be larger as well. However, they investigated the subjects after more than 30 hrs of caffeine deprivation, when typical withdrawal symptoms, such as headache and fatigue, reach a maximum in intensity (41). In contrast to their study design, we did not recruit heavy caffeine users. We consider it a more realistic scenario that the users are not in a state of severe withdrawal when the subjects refrain from caffeine intake 24 hrs prior to the scan.

In conclusion, this chapter demonstrates an improvement in the iterative algorithm for susceptibility mapping and evaluates the variation in oxygen extraction fraction before and after a vasoconstricting caffeine challenge as well as a vasodilating Diamox challenge using quantitative susceptibility mapping. These vascular effects of acetazolamide and caffeine, in normal human subjects, were proven to be large enough to be easily measured with susceptibility mapping for all people. Therefore, this susceptibility difference can serve as a sensitive biomarker for measuring reductions in cerebro-vascular reserve through abnormal vascular response, an increase in oxygen consumption during reperfusion hyperoxia or locally varying oxygen saturation levels in the region surrounding damaged tissue.

## References

1. Ogawa S, Lee TM, Kay AR, Tank DW. Brain magnetic resonance imaging with contrast dependent on blood oxygenation. *Proc Natl Acad Sci USA*. 1990 Dec; 87(24):9868–72.
2. Ogawa S, Menon RS, Tank DW, Kim SG, Merkle H, Ellermann JM, et al. Functional brain mapping by blood oxygenation level-dependent contrast magnetic resonance

- imaging. A comparison of signal characteristics with a biophysical model. *Biophys J*. 1993 Mar;64(3):803–12.
3. Haacke EM, Tang J, Neelavalli J, Cheng YCN. Susceptibility mapping as a means to visualize veins and quantify oxygen saturation. *J Magn Reson Imaging JMRI*. 2010 Sep;32(3):663–76.
  4. Kwong KK, Belliveau JW, Chesler DA, Goldberg IE, Weisskoff RM, Poncelet BP, et al. Dynamic magnetic resonance imaging of human brain activity during primary sensory stimulation. *Proc Natl Acad Sci U S A*. 1992 Jun 15;89(12):5675–9.
  5. Haacke EM, Lai S, Reichenbach JR, Kuppusamy K, Hoogenraad FG, Takeichi H, et al. In vivo measurement of blood oxygen saturation using magnetic resonance imaging: a direct validation of the blood oxygen level-dependent concept in functional brain imaging. *Hum Brain Mapp*. 1997;5(5):341–6.
  6. Rauscher A, Sedlacik J, Barth M, Haacke EM, Reichenbach JR. Noninvasive assessment of vascular architecture and function during modulated blood oxygenation using susceptibility weighted magnetic resonance imaging. *Magn Reson Med*. 2005 Jul;54(1):87–95.
  7. Logothetis NK. What we can do and what we cannot do with fMRI. *Nature*. 2008 Jun 12;453(7197):869–78.
  8. Van Zijl PC, Eleff SM, Ulatowski JA, Oja JM, Uluğ AM, Traystman RJ, et al. Quantitative assessment of blood flow, blood volume and blood oxygenation effects in functional magnetic resonance imaging. *Nat Med*. 1998 Feb;4(2):159–67.
  9. Hr S. Blood flow and metabolism by PET. *Cardiol Clin*. 1994 May;12(2):303–15.
  10. Leenders KL, Perani D, Lammertsma AA, Heather JD, Buckingham P, Jones T, et al. Cerebral Blood Flow, Blood Volume and Oxygen Utilization. *Brain*. 1990 Feb 1;113(1):27–47.

11. Sobesky J, Zaro Weber O, Lehnhardt F-G, Hesselmann V, Neveling M, Jacobs A, et al. Does the mismatch match the penumbra? Magnetic resonance imaging and positron emission tomography in early ischemic stroke. *Stroke J Cereb Circ.* 2005 May;36(5):980–5.
12. Miles KA, Williams RE. Warburg revisited: imaging tumour blood flow and metabolism. *Cancer Imaging Off Publ Int Cancer Imaging Soc.* 2008;8:81–6.
13. Haacke EM, Cheng NYC, House MJ, Liu Q, Neelavalli J, Ogg RJ, et al. Imaging iron stores in the brain using magnetic resonance imaging. *Magn Reson Imaging.* 2005 Jan;23(1):1–25.
14. Chiarelli PA, Bulte DP, Wise R, Gallichan D, Jezzard P. A calibration method for quantitative BOLD fMRI based on hyperoxia. *NeuroImage.* 2007 Sep 1;37(3):808–20.
15. Hyder F, Herman P, Sanganahalli BG, Coman D, Blumenfeld H, Rothman DL. Role of Ongoing, Intrinsic Activity of Neuronal Populations for Quantitative Neuroimaging of Functional Magnetic Resonance Imaging–Based Networks. *Brain Connect.* 2011 Sep;1(3):185–93.
16. Xu F, Ge Y, Lu H. Noninvasive quantification of whole-brain cerebral metabolic rate of oxygen (CMRO<sub>2</sub>) by MRI. *Magn Reson Med.* 2009 Jul;62(1):141–8.
17. Haacke EM, Reichenbach JR. *Susceptibility Weighted Imaging in MRI: Basic Concepts and Clinical Applications.* John Wiley & Sons; 2014. 916 p.
18. Tang J, Liu S, Neelavalli J, Cheng YCN, Buch S, Haacke EM. Improving susceptibility mapping using a threshold-based K-space/image domain iterative reconstruction approach. *Magn Reson Med.* 2013 May;69(5):1396–407.
19. Haacke EM. *Magnetic resonance imaging: physical principles and sequence design.* New York, NY [u.a.: Wiley-Liss; 1999].

20. Mathew RJ. Caffeine induced changes in cerebral circulation. *Stroke J Cereb Circ.* 1986 Dec;17(6):1337.
21. Cameron OG, Modell JG, Hariharan M. Caffeine and human cerebral blood flow: a positron emission tomography study. *Life Sci.* 1990;47(13):1141–6.
22. Sutherland GR, Peeling J, Lesiuk HJ, Brownstone RM, Rydzy M, Saunders JK, et al. The effects of caffeine on ischemic neuronal injury as determined by magnetic resonance imaging and histopathology. *Neuroscience.* 1991;42(1):171–82.
23. Mulderink TA, Gitelman DR, Mesulam M-M, Parrish TB. On the use of caffeine as a contrast booster for BOLD fMRI studies. *NeuroImage.* 2002 Jan;15(1):37–44.
24. Addicott MA, Yang LL, Peiffer AM, Burnett LR, Burdette JH, Chen MY, et al. The effect of daily caffeine use on cerebral blood flow: How much caffeine can we tolerate? *Hum Brain Mapp.* 2009 Oct;30(10):3102–14.
25. Chen Y, Parrish TB. Caffeine's effects on cerebrovascular reactivity and coupling between cerebral blood flow and oxygen metabolism. *NeuroImage.* 2009 Feb 1;44(3):647–52.
26. Fujima N, Kudo K, Terae S, Ishizaka K, Yazu R, Zaitso Y, et al. Non-invasive measurement of oxygen saturation in the spinal vein using SWI: quantitative evaluation under conditions of physiological and caffeine load. *NeuroImage.* 2011 Jan 1;54(1):344–9.
27. Yamauchi H, Okazawa H, Kishibe Y, Sugimoto K, Takahashi M. The effect of acetazolamide on the changes of cerebral blood flow and oxygen metabolism during visual stimulation. *NeuroImage.* 2003 Sep;20(1):543–9.
28. Hedera P, Lai S, Lewin JS, Haacke EM, Wu D, Lerner AJ, et al. Assessment of cerebral blood flow reserve using functional magnetic resonance imaging. *J Magn Reson Imaging JMRI.* 1996 Oct;6(5):718–25.

29. Grossmann WM, Koeberle B. The dose-response relationship of acetazolamide on the cerebral blood flow in normal subjects. *Cerebrovasc Dis Basel Switz*. 2000 Feb;10(1):65–9.
30. Okazawa H, Yamauchi H, Sugimoto K, Toyoda H, Kishibe Y, Takahashi M. Effects of acetazolamide on cerebral blood flow, blood volume, and oxygen metabolism: a positron emission tomography study with healthy volunteers. *J Cereb Blood Flow Metab Off J Int Soc Cereb Blood Flow Metab*. 2001 Dec;21(12):1472–9.
31. Haacke EM, Liu S, Buch S, Zheng W, Wu D, Ye Y. Quantitative susceptibility mapping: current status and future directions. *Magn Reson Imaging*. 2015 Jan;33(1):1–25.
32. Ye Y, Hu J, Wu D, Haacke EM. Noncontrast-enhanced magnetic resonance angiography and venography imaging with enhanced angiography. *J Magn Reson Imaging JMRI*. 2013 Dec;38(6):1539–48.
33. Haacke EM, Mittal S, Wu Z, Neelavalli J, Cheng Y-CN. Susceptibility-Weighted Imaging: Technical Aspects and Clinical Applications, Part 1. *Am J Neuroradiol*. 2009 Jan 1;30(1):19–30.
34. Ghiglia DC, Romero LA. Robust two-dimensional weighted and unweighted phase unwrapping that uses fast transforms and iterative methods. *J Opt Soc Am A*. 1994 Jan 1;11(1):107–17.
35. Abdul-Rahman HS, Gdeisat MA, Burton DR, Lalor MJ, Lilley F, Moore CJ. Fast and robust three-dimensional best path phase unwrapping algorithm. *Appl Opt*. 2007 Sep 10;46(26):6623–35.
36. De Rochefort L, Liu T, Kressler B, Liu J, Spincemaille P, Lebon V, et al. Quantitative susceptibility map reconstruction from MR phase data using bayesian regularization:

- validation and application to brain imaging. *Magn Reson Med*. 2010 Jan;63(1):194–206.
37. Xia S, Utriainen D, Tang J, Kou Z, Zheng G, Wang X, et al. Decreased oxygen saturation in asymmetrically prominent cortical veins in patients with cerebral ischemic stroke. *Magn Reson Imaging*. 2014 Dec;32(10):1272–6.
  38. Yamauchi H, Fukuyama H, Nagahama Y, Nabatame H, Ueno M, Nishizawa S, et al. Significance of increased oxygen extraction fraction in five-year prognosis of major cerebral arterial occlusive diseases. *J Nucl Med Off Publ Soc Nucl Med*. 1999 Dec;40(12):1992–8.
  39. Fantini S. A haemodynamic model for the physiological interpretation of in vivo measurements of the concentration and oxygen saturation of haemoglobin. *Phys Med Biol*. 2002 Sep 21;47(18):N249–57.
  40. Li M, Hu J, Miao Y, Shen H, Tao D, Yang Z, et al. In Vivo Measurement of Oxygenation Changes after Stroke Using Susceptibility Weighted Imaging Filtered Phase Data. *PLoS ONE*. 2013 May 13;8(5):e63013.
  41. Nehlig A, Daval JL, Debry G. Caffeine and the central nervous system: mechanisms of action, biochemical, metabolic and psychostimulant effects. *Brain Res Brain Res Rev*. 1992 Aug;17(2):139–70.
  42. Sedlacik J, Rauscher A, Reichenbach JR. Quantification of modulated blood oxygenation levels in single cerebral veins by investigating their MR signal decay. *Z Für Med Phys*. 2009;19(1):48–57.
  43. Jain V, Langham MC, Wehrli FW. MRI estimation of global brain oxygen consumption rate. *J Cereb Blood Flow Metab*. 2010 Sep;30(9):1598–607.

44. Ge Y, Zhang Z, Lu H, Tang L, Jaggi H, Herbert J, et al. Characterizing brain oxygen metabolism in patients with multiple sclerosis with T2-relaxation-under-spin-tagging MRI. *J Cereb Blood Flow Metab.* 2012 Mar;32(3):403–12.
45. Donoho DL. Compressed sensing. *IEEE Trans Inf Theory.* 2006 Apr;52(4):1289–306.
46. Lustig M, Donoho D, Pauly JM. Sparse MRI: The application of compressed sensing for rapid MR imaging. *Magn Reson Med.* 2007 Dec;58(6):1182–95.
47. Candes EJ, Tao T. Near-Optimal Signal Recovery From Random Projections: Universal Encoding Strategies? *IEEE Trans Inf Theory.* 2006 Dec;52(12):5406–25.
48. Rinsler M. Clinical Diagnosis and Management by Laboratory Methods. *J Clin Pathol.* 1981 Feb;34(2):228.
49. Uludağ K, Dubowitz DJ, Yoder EJ, Restom K, Liu TT, Buxton RB. Coupling of cerebral blood flow and oxygen consumption during physiological activation and deactivation measured with fMRI. *NeuroImage.* 2004 Sep;23(1):148–55.
50. Wu CW, Gu H, Lu H, Stein EA, Chen J-H, Yang Y. Mapping functional connectivity based on synchronized CMRO<sub>2</sub> fluctuations during the resting state. *NeuroImage.* 2009 Apr 15;45(3):694–701.
51. Field AS, Laurienti PJ, Yen Y-F, Burdette JH, Moody DM. Dietary caffeine consumption and withdrawal: confounding variables in quantitative cerebral perfusion studies? *Radiology.* 2003 Apr;227(1):129–35.

## Chapter 6: Future Directions

### Measuring bone density using phase replacement method

As discussed in Chapter 3, the phase replacement process helps in improving the susceptibility reconstruction inside an object, with unreliable MR signal present initially (1). This was evaluated on large and complex structures such as sinuses and bones; and this approach has further potential applications in field of material science and non-destructive testing. Another potential application would be to determine the bone density measurements (which are generally calculated using CT (2,3)) based on the reconstructed susceptibility distributions of the skull and teeth . In order to validate this, the susceptibility maps can be compared with the standard CT results. Ability to measure the bone density using MR, at high resolution, can prove to be essential in determining attenuation correction for PET-MR systems (4–7).

## Background field removal using sinus maps

In addition, as the replacement of the unreliable signal inside an object of interest helps in improving the accuracy of the susceptibility estimation and, hence, can be also used to reduce the artifacts in the resultant images if the given object is a source of an unwanted field. For example, removal of the background field by predicting the field perturbations caused the susceptibility distributions of sinuses and bones and subtracting it from the original phase (1,8).

Although the field predictions were close to the original phase data, there is a small remnant phase still present in the subtraction result. The main reasons that can cause this are: 1) the phase term induced by the geometry of the head and 2) the air-tissue interfaces due to the air outside the head. Further research needs to be done to study these two aspects. Ideally, the predicted field from the air/bone mapping process should remove all the background field caused by the air/bone-tissue interfaces, discarding the need of any further filtering.

## Artifacts due to the acceleration term

As seen in *Chapter 4*, the blood flow in presence of the background gradients can create false phase term inside the arteries, which in turn can introduce significant streaking artifacts in the susceptibility maps. These background gradients are produced by the air/bone-tissue interface induced field inhomogeneities in head, which are considered and evaluated in this thesis using a numerical phantom and *in vivo* data.

However, apart from the background gradient term, there is a need to consider the effects of motion, misregistration and also acceleration due to the pulsatile nature of blood flow in arteries. This could be achieved by acquiring an interleaved scan with positive polarity of the gradients for the first two echoes and negative polarity for the second set of the same two echo times. Nevertheless, one of the effective solutions for the false phase term is to generate binary masks of the arteries using the first echo magnitude image, and use it to discard the internal phase and, hence, improving the SWIM results (as shown in **Figure 4.8** in *Chapter 4*).

### Cerebral blood flow and CMRO<sub>2</sub> measurements

In *Chapter 5*, the forced initial value iterative method demonstrates the added improvement in SWIM results by reducing the streaking artifacts inside the veins. In addition, vasodynamic agents, such as caffeine and Diamox were tested on healthy volunteers to evaluate the efficacy of susceptibility mapping technique to detect the changes in the cerebral venous blood oxygenation levels. These challenges can be tested on patients suffering from traumatic brain injury, stroke or vascular pathologies to study the viability of the affected brain tissues throughout a treatment procedure (9–17). Furthermore, to see if the CMRO<sub>2</sub> remains the same after these challenges will require perfusion measurements as well in the future (18–22). By combining the approaches explained in *Chapter 3, 4 and 5*, we can get a highly reliable measure of oxygen saturation in the jugular veins without background field effects, flow effects or filter effects.

## References

1. Buch S, Liu S, Ye Y, Cheng Y-CN, Neelavalli J, Haacke EM. Susceptibility mapping of air, bone, and calcium in the head. *Magn Reson Med*. 2014 Jul 7;
2. Homolka P, Beer A, Birkfellner W, Nowotny R, Gahleitner A, Tschabitscher M, et al. Bone mineral density measurement with dental quantitative CT prior to dental implant placement in cadaver mandibles: pilot study. *Radiology*. 2002 Jul;224(1):247–52.
3. Burghardt AJ, Link TM, Majumdar S. High-resolution Computed Tomography for Clinical Imaging of Bone Microarchitecture. *Clin Orthop*. 2011 Aug;469(8):2179–93.
4. Kops ER, Herzog H. Alternative methods for attenuation correction for PET images in MR-PET scanners. *IEEE Nuclear Science Symposium Conference Record, 2007 NSS '07*. 2007. p. 4327–30.
5. Beyer T, Weigert M, Quick HH, Pietrzyk U, Vogt F, Palm C, et al. MR-based attenuation correction for torso-PET/MR imaging: pitfalls in mapping MR to CT data. *Eur J Nucl Med Mol Imaging*. 2008 Jun;35(6):1142–6.
6. Zaidi H. Is MR-guided Attenuation Correction a Viable Option for Dual-Modality PET/MR Imaging? *Radiology*. 2007 Sep 1;244(3):639–42.
7. Kops ER, Qin P, Müller-Veggian M, Herzog H. MRI Based Attenuation Correction for Brain PET Images. *Advances in Medical Engineering. Springer Proceedings in Physics Volume 114*, 2007, pp 93-97
8. Neelavalli J, Cheng Y-CN, Jiang J, Haacke EM. Removing background phase variations in susceptibility-weighted imaging using a fast, forward-field calculation. *J Magn Reson Imaging*. 2009 Apr;29(4):937–48.

9. Li M, Hu J, Miao Y, Shen H, Tao D, Yang Z, et al. In Vivo Measurement of Oxygenation Changes after Stroke Using Susceptibility Weighted Imaging Filtered Phase Data. *PLoS ONE*. 2013 May 13;8(5):e63013.
10. Mathew RJ. Caffeine induced changes in cerebral circulation. *Stroke J Cereb Circ*. 1986 Dec;17(6):1337.
11. Xia S, Utriainen D, Tang J, Kou Z, Zheng G, Wang X, et al. Decreased oxygen saturation in asymmetrically prominent cortical veins in patients with cerebral ischemic stroke. *Magn Reson Imaging*. 2014 Dec;32(10):1272–6.
12. Sutherland GR, Peeling J, Lesiuk HJ, Brownstone RM, Rydzy M, Saunders JK, et al. The effects of caffeine on ischemic neuronal injury as determined by magnetic resonance imaging and histopathology. *Neuroscience*. 1991;42(1):171–82.
13. Dash PK, Moore AN, Moody MR, Treadwell R, Felix JL, Clifton GL. Post-trauma administration of caffeine plus ethanol reduces contusion volume and improves working memory in rats. *J Neurotrauma*. 2004 Nov;21(11):1573–83.
14. Sachse KT, Jackson EK, Wisniewski SR, Gillespie DG, Puccio AM, Clark RSB, et al. Increases in cerebrospinal fluid caffeine concentration are associated with favorable outcome after severe traumatic brain injury in humans. *J Cereb Blood Flow Metab*. 2008 Feb;28(2):395–401.
15. Popa G, Amaireh M, Dinu M, Jipescu I, Alaicescu M, Stănescu A, et al. Acetazolamide therapy evaluation in haemorrhagic stroke. *Romanian J Neurol Psychiatry Rev Roum Neurol Psychiatr*. 1995 Jun;33(2):145–55.
16. Yoshida K, Nakamura S, Watanabe H, Kinoshita K. Early cerebral blood flow and vascular reactivity to acetazolamide in predicting the outcome after ruptured cerebral aneurysm. *Acta Neurol Scand Suppl*. 1996;166:131–4.

17. Kashiwagi S, Kitahara T, Shirao S, Moroi J, Kato S, Nakayama H, et al. The value of acetazolamide challenge test in the evaluation of acute stroke. *Keio J Med.* 2000 Feb;49 Suppl 1:A120–1.
18. Maxwell WL, Irvine A, Adams JH, Graham DI, Gennarelli TA. Response of cerebral microvasculature to brain injury. *J Pathol.* 1988 Aug 1;155(4):327–35.
19. Xu F, Ge Y, Lu H. Noninvasive quantification of whole-brain cerebral metabolic rate of oxygen (CMRO<sub>2</sub>) by MRI. *Magn Reson Med.* 2009 Jul;62(1):141–8.
20. Wise RG, Harris AD, Stone AJ, Murphy K. Measurement of OEF and absolute CMRO<sub>2</sub>: MRI-based methods using interleaved and combined hypercapnia and hyperoxia. *NeuroImage.* 2013 Dec;83:135–47.
21. Detre JA, Leigh JS, Williams DS, Koretsky AP. Perfusion imaging. *Magn Reson Med.* 1992 Jan;23(1):37–45.
22. Grubb RL, Raichle ME, Eichling JO, Ter-Pogossian MM. The effects of changes in PaCO<sub>2</sub> on cerebral blood volume, blood flow, and vascular mean transit time. *Stroke J Cereb Circ.* 1974 Oct;5(5):630–9.